ENHANCED METHODS OF OCEAN WAVE SPECTRA AND SEA STATE PARAMETER ESTIMATION FROM X-BAND MARINE RADAR DATA

A thesis submitted to the
School of Graduate Studies
in partial fulfillment of the
requirements for the degree of
Doctor of Philosophy

by
© Al-Abbass Al-Habashneh

Faculty of Engineering and Applied Science
Memorial University of Newfoundland
St. John's, NL.

May 2018

This thesis is dedicated to the soul of my maternal grandmother ‘Safieh’, parental grandfather ‘Abdallah’and uncle ‘Mahmoud’ who passed away while I was far from home pursuing my PhD degree. I also dedicate this thesis to my beloved parents, Yousef and Aisha, my brothers, Almeqdad, Kotayba, and Obada, and my sisters, Asma, Tamador, and Ateka for their endless love and support throughout my entire life.

Acknowledgment

I would like express my special appreciation and thanks to my advisers Prof. Cecilia Moloney and Prof. Eric W. Gill. Without you it would have been impossible to achieve this work. Your guidance and support have always been the torch that lighten up my way throughout my entire PhD journey. I could not have imagined having better advisers and mentors for my PhD studies. Your warm encouragement and thoughtful guidance have indeed shaped the researcher I am today.

My sincere thanks also goes to Dr. Weimin Huang. Your open door has been inviting whenever I feel in need of help and guidance.

Finally, I thank the Natural Sciences and Engineering Research Council of Canada (NSERC) for their financial support.

Abstract

Due to the ocean's importance in human lives, researchers have been studying the ocean and developing systems to estimate its state since the 19th century. During the last three decades, remote sensing of the ocean surface using X-band marine radars has emerged as a reliable tool to estimate ocean wave spectra and sea state parameters such as mean wave period and direction and significant wave height.

The purpose of this thesis is to develop methods that produce accurate and reliable estimates of ocean wave spectra using X-band marine radar data. The approach taken in this thesis is to determine the sources of ocean wave spectra estimation error in existing methods and then to develop new methods that minimize those errors. In this thesis, four sources of error are addressed: the dependency of spectra estimation on the orientation of the analysis windows; the effect of the radar sampling process; the effect of the scan conversion process; and the accuracy of surface current estimation.

The azimuthal location of the X-band radar data analysis window affects the estimation of ocean wave spectra. It has been reported in the literature, and supported by our results, that using the up-wave directions for analysis windows produces higher signal to noise ratios and hence more accurate ocean wave spectra estimates. In order to minimize error due to dependency on the orientation of the analysis windows, a new method referred to as the Adaptive Recursive Positioning Method (ARPM) is proposed. The ARPM is a recursive approach that dynamically determines the optimal number of analysis windows and their corresponding orientation toward the up-wave directions.

Second, in this thesis, it has been demonstrated that the sampling process of the ocean surface by X-band marine radar during data collection significantly affects the estimation of ocean wave spectra from X-band marine radar data. Therefore, a method referred to as the Inverse Sampling Averaging Filter (ISAF) is proposed to mitigate the effect of the radar sampling process of the ocean surface on the ocean

wave spectra estimation using X-band marine radars. ISAF was designed based on a novel understanding of the radar sampling process to involve an averaging process or low pass filtering of the ocean wave spectra.

Third, in this thesis, a method referred to as the Polar Fourier Transform (PFT) is proposed to eliminate the distortion presented by the scan conversion process to the estimated wave spectra. Unlike the existing methods which use the Cartesian Fourier Transform (CFT) to acquire the ocean wave spectra, the PFT method is designed to apply a Fourier-type transformation on the radar data in its native format, which is sampled in the polar coordinates, without the need for the intermediate stage of scan conversion used to map the data into Cartesian coordinates.

The performance of the proposed methods, the ARPM, ISAF and PFT, are individually validated by comparing their ocean wave spectra estimates to those acquired using the existing methods with respect to ground truth wave spectra acquired using a wave rider buoy. Furthermore, the proposed methods were also combined together to seek further enhancement. The wave spectra estimation results from different combinations of the proposed methods were validated in comparison to the ground truth data.

Finally, a new method to estimate surface current using X-band marine radar is proposed. This method is referred to as the Hybrid Least Squares (HLS) method. The HLS combines two existing approaches: the Iterative Least Squares (ILS) method and the Normalized Scalar Product (NSP). The HLS is designed to inherit the short computational time of ILS and the high reliability of NSP. To validate its accuracy and reliability, the proposed HLS method was applied on a number of simulated X-band marine radar image sets and the results were compared to the estimates acquired using the ILS and the NSP.

Contents

List of Tables

List of Figures

List of Symbols

x, y	Spatial Cartesian coordinates	9
t	Time coordinate	9
ζ	Ocean surface elevation	9
k_x, k_y	Ocean wave vector components in Cartesian coordinates	9
ω	Ocean wave angular frequency	9
A	Ocean wave amplitude	9
ψ	A random phase	9
σ_n	Normal distribution standard deviation	10
E_t	The average energy per unit area of the ocean surface	10
f	Ocean wave frequency	10
λ_w	Ocean wave wavelength	22
λ_e	Radar electromagnetic radiation wavelength	22
ϕ	Electromagnetic radiation indecent angle	22
$\mathbf{r}$	Space-time vector (x, y, t)	21
N	The number of elements in the space time domain	21
r_i, φ_i	B-scan image sample with indices	22
R_i, Φ_i	Size of B-scan images	22
X_i, Y_i	Size of radar Cartesian images	22
Δ_x, Δ_y	Radar Cartesian image resolution	22

Δ_r, Δ_θ	Radar B-scan image resolution	22
Φ_{in}	The initial B-scan azimuth direction clockwise from true north	22
ν	Non-wave components in image spectrum	27
$\mathbf{\Omega}$	3D wave number-frequency vector (k_x, k_y, ω)	26
k, θ	Ocean wave number magnitude and phase	27
$\mathbf{k}$	Ocean wave number vector	27
g	The acceleration of gravity	27
$\mathbf{U}$	Ocean surface velocity of encounter vector	27
d	Water depth	27
$\Delta\omega$	The angular frequency resolution	27
T_s	The radar sampling/rotating time	27
N_t	The analysis window size in the time domain	27
β	Modulation Transfer Function (MTF) decaying exponent	30
m_n	The n^{th} spectral moment	32
f_p	Ocean peak wave frequency	32
T_p	Ocean peak wave period	32
T_{01}	Ocean mean wave period	32
T_z	Ocean zero-crossing wave period	32
θ_m	Ocean wave mean direction	32
H_s	Significant wave height	33
ρ	Correlation coefficient	53
E_R	Radar-estimated normalized frequency spectrum	53
E_B	Buoy-estimated normalized frequency spectrum	53
N_f	The number of frequency points in E_R and E_B	53
$\overline{\lvert\varepsilon_{T_p}\rvert}$	The mean absolute error in T_p estimation	56
$\overline{\lvert\varepsilon_{T_{01}}\rvert}$	The mean absolute error in T_{01} estimation	56

$\overline{\lvert\varepsilon_{T_z}\rvert}$	The mean absolute error in T_z estimation	56
θ_p	Peak wave direction	56
$\sigma_{\varepsilon_{T_p}}$	Error standard deviation of T_p estimates	56
$\sigma_{\varepsilon_{T_{01}}}$	Error standard deviation of T_{01} estimates	56
$\sigma_{\varepsilon_{T_z}}$	Error standard deviation of T_z estimates	56
$\sigma_{\varepsilon_{\theta_p}}$	Error standard deviation of θ_p estimates	56
T_{pBuoy}	Ground truth ocean peak wave period	56
N_e	The total number of radar estimates	56
c	The speed of light	62
τ	The radar sampling period	62
BW	Radar half power beam width	62
L_x, L_y	The size of the fine grid simulated Cartesian images	66
dx, dy	The resolution of the fine grid simulated Cartesian images	66
$\tilde{k}_x, \tilde{k}_y$	Normalized wave number vector components	67
r_z	The magnitude of filter zeros	67
σ	Analog filter attenuation constant	71
r, φ	Spatial polar coordinates	89

Chapter 1

Introduction

1.1 The importance of the ocean

An interconnected volume of saltwater covers roughly 71% of the planet surface and represents one of the most valuable natural resources on Earth [2]. Throughout history, the ocean has directly or indirectly influenced human lives in many ways. The ocean provides convenient travel and shipping routes, by which most goods traded between countries are carried. The ocean is also a major source of food. According to the Food and Agricultural Organization (FAO) of the United Nations, 16.7% of the total human consumption of animal protein in 2010 was contributed by seafood [3]. In Canada, which has a wide access to the Atlantic and Pacific Oceans as well as Arctic water with extended coastlines, fisheries significantly contribute to the economy of the country. For the year 2015, Canada's statistics show that the total number of persons employed in the fisheries was 76 044, while the total values of seafood imports and exports were \$3 438 791 and \$5 958 905, respectively [4]. Crude oil and natural gas, which are among the most important energy sources in the world, may be found under the seabed. In Newfoundland and Labrador alone, three major offshore oil drilling projects exist: Hibernia, operated by Hibernia Management and Development

Company Ltd, Terra Nova, operated by Suncor Energy, and White Rose, operated by Husky Energy [5]. The Government of Newfoundland and Labrador estimates the potential Newfoundland and Labrador offshore reserve of crude oil and natural gas to be more than 6 billion barrels and 60 trillion cubic feet, respectively [5]. The ocean is also a significant source of other minerals such as salt, copper, nickel, iron and cobalt. Furthermore, the ocean plays a key role in regulating the climate and removing carbon dioxide from the air.

1.2 Motivation

The ocean has been studied intensively by oceanographers and engineers in order to better exploit its resources. A knowledge of the ocean surface wave system is essential for a wide range of applications. For instance, in coastal engineering, ocean waves are the main force pressuring breakwaters and can severely damage them. Therefore, a knowledge of the ocean wave system is crucial to the design of breakwaters. Similarly, in offshore engineering, ocean waves generate forces on the piles on offshore structures. In the application of ship response to waves, a knowledge of the wave system is used to provide more stability to the ship motion [6]. Representing the ocean wave system using a descriptive analytical model has received a great deal of attention from researchers due to the benefits in understanding the ocean wave system and predicting its behavior and correlation with climate conditions. The frequency wave spectrum and the directional wave spectrum are perhaps the most common models of describing ocean surface waves. In fact, the aforementioned applications of breakwaters and offshore structures and the response of ships use parameters that are directly calculated from the directional wave spectrum. The concept of using ocean wave spectra to describe complex ocean surface elevation started about 60 years ago [7, 8]. Several ocean wave spectral estimation methods working on different principles have been developed based on the technologies of directional wave rider buoys, High Frequency (HF) radars, marine radars, and Synthetic Aperture Radars (SARs) [9]. Because of its mobility, reliability and cost efficiency, the X-band marine radar-based method of wave spectra estimation has gained great attention from oceanographers. Nowadays, almost every water craft of a significant size is equipped with X-band marine radar technology which was initially implemented for target detection and navigation purposes. The popularity of X-band marine radars makes them more accessible to be used for wave spectra estimation.

In order to better understand the ocean and exploit its resources, researchers and oceanographers have been continuously exploring the technology of using X-band marine radar in ocean wave spectral estimation method by increasing its accuracy and reliability. In the X-band marine radar-based method, an image spectrum is acquired by applying the Cartesian Fourier Transform (CFT) on the ocean surface images generated by radars. Subsequently, a directional ocean wave spectrum is estimated from the image spectrum by excluding the non-wave spectral components and applying a Modulation Transfer Function (MTF) to mitigate the effect of the radar imaging process [10, 11].

The effect of X-band marine radar imaging of the ocean surface on the estimated ocean wave spectra is one of the active research areas for the technology. This is due to the complexity of the radar imaging process in which several phenomena contribute to the radar images of the ocean surface. These phenomena include shadowing, tilt modulation, and the dependency of returned radar scatter on the range, wind speed and wave propagation direction [9]. The non-linear contribution of these phenomena makes their effect on the estimated ocean wave spectra one of the ill-defined problems among X-band radar-based methods for ocean wave spectral estimation. In this thesis, several aspects of the X-band marine radar imaging process and radar-based spectral estimation methods are studied in order to improve the performance of the CFT method.

1.3 Problem Definition

The purpose of this thesis is to develop accurate and reliable wave spectra estimation methods using X-band marine radar. Our approach is to identify the sources of error in the common Cartesian Fourier Transform (CFT) method and design new methods to mitigate those various sources of error. Several sources of error that have been addressed in this thesis include the following:

1. **The dependency on the analysis windows orientation**

   One of the sources of error in estimating the ocean wave spectra using X-band radar data via the CFT method is the dependency of the returned radar signal strength on the azimuth direction. In the past, this problem has been addressed by averaging the wave spectra over several analysis windows that are spatially uniformly distributed. Except for one study by Lund *et al.* [12], this problem has not been sufficiently discussed in the literature. In [12], the effect of the analysis window location (range and orientation) is studied in the context of Signal to Noise Ratio (SNR). It is further proposed in [12] to choose the orientation of the analysis window in the up-wave direction for maximum SNR which provides, by extension, better wave spectrum estimation.

2. **Radar sampling of the ocean surface**

   In the literature, the generation of B-scan samples by X-band marine radars has been viewed as a standard sampling of the ocean surface in which the returned scatter is recorded at the centre of a sample's patch area. Looking carefully at the sampling process, it can be seen that this understanding of the ocean surface sampling is not completely accurate since the returned scatter is collected over the entire sample area, as determined by the radar setting parameters including pulse length and beam width, and not only the centre of the area. This problem has not been previously addressed. Understanding the effect of the ocean surface sampling process on the estimated ocean wave spectra might help in developing an algorithm to mitigate that effect.

3. **The scan conversion process**

   Polar coordinates are naturally imposed on the X-band marine radar output data in correspondence with the manner of sample collection. B-scan samples are arranged on a polar grid with range and azimuth resolutions that are set by the radar parameters. In order to estimate ocean wave spectra using the CFT method, the data must be re-sampled on a Cartesian grid [13] through a process that is referred to as 'scan conversion'. This process can be visualized as a recovery of the original continuous image of ocean surface elevation followed by a sampling on a new Cartesian grid. Two difficulties are encountered with this process. First, the original sampling on a polar grid is non-uniform in terms of the number of samples per unit area. Second, in order to completely recover the original continuous image from the radar image, an ideal low pass filter is required. Since ideal low pass filters can only be realized by an approximation, a distortion in the recovered ocean wave spectra will result [13–15].

4. **Accuracy and reliability of the surface current estimation**

   The surface current information is one of the important sea state parameters that can be estimated using the CFT method. Various applications including ship navigation and oil spill control require surface current information. Furthermore, the CFT method itself depends on estimating the velocity of encounter, which includes the ocean surface current and the observer's velocity, in excluding the non-wave components from the ocean wave spectra. Two approaches that are most commonly used to estimate surface current vectors presently appear in the literature: the Iterative Least Squares (ILS) method and the Normalized Scalar Product (NSP) method. The latter provides accurate and reliable estimates at both low and high values of velocity of encounter. However, the NSP is computationally expensive which may limit its implementation for real-time analysis. On the other hand, the ILS method provides accurate and reliable estimates at low values of velocity of encounter but it becomes less robust at higher values of velocity of encounter. This is due to the high aliasing effect at high values of velocity of encounter which makes it hard for the algorithm to estimate a good initial value to start the recursive process.

1.4 Approach to the Solution and Outline of Thesis

In Chapter 2, the relevant background, physics, and literature are reviewed. Chapter 2 presents an overview of the ocean wave spectral descriptive model, methods of ocean wave spectral estimation, and a review of the CFT method of ocean wave spectral estimation using X-band marine radar. Also, the field data used to validate the subsequently proposed methods are described in Chapter 2. In order to achieve more accurate and reliable estimates of the ocean wave spectra, the following estimation algorithms are proposed to mitigate the sources of error in the CFT method that are addressed in Section 1.3:

1. **The Adaptive Recursive Positioning Method (ARPM)**

   Since the signal-to-noise ratio is highest in the up-wave direction [12], less error can be expected in the estimation of wave spectra when the analysis window is chosen in the up-wave direction. Two difficulties exist with this approach. First, the wave system may contain multiple peaks from wind waves and swell. Second, the directional wave spectrum is generally not known *a priori*. Therefore, the ARPM is proposed to select the number and direction of analysis windows recursively.

In Chapter 3, the dependancy of wave spectra estimation in the presence of both types of waves as manifested by wave spectra components (wind waves and swell) is invistigated further. Also, the ARPM and performance analysis are presented. The estimates of ocean wave spectra using the ARPM were validated against the standard method using radar field data. The results from both methods were validated against ground truth data acquired using a TRIAXYS wave rider buoy are used. This work was also presented in [16].

2. **The Inverse Sampling Averaging Filter (ISAF)**

   An analytical model that describes the ocean surface sampling process is presented in Chapter 4. Furthermore, a Modulation Transfer Function referred to as the Inverse Sampling Averaging Filter (ISAF) is proposed to mitigate the effects of the radar sampling process based on the presented analytical model. The performance of the ISAF was also validated in comparison with the standard method and ground truth data acquired using a TRIAXYS wave rider buoy.

3. **The Polar Fourier Transform (PFT)**

   In order to eliminate the error that results from scan conversion, we propose to implement the Polar Fourier Transform (PFT) [17] on B-scan images directly. This makes the scan-conversion process unnecessary. In Chapter 5, a full description of the PFT in three dimensions is presented. The performance of the PFT was also validated in comparison with the CFT method and ground truth data acquired using a TRIAXYS wave rider buoy. Introductory work on this method was presented in [14, 15].

A performance comparison of the CFT, PFT, ARPM, and ISAF methods is presented in Chapter 6. An investigation of the applicability of combining these methods and an evaluation of the resulting enhancement/deterioration in the performance of estimating ocean wave spectra and sea state parameters is also undertaken.

4. **The Hybrid Least Squares (HLS) method**

   In Chapter 7 of this thesis, a review the ILS and NSP is presented. Also, a Hybrid method of the two, referred to as the Hybrid Least Squares (HLS) method, is proposed to estimate surface current with high accuracy and reliability at high values of surface current speed and with a low computational price. This work was also presented in [18].

Chapter 8 concludes the thesis and summarizes its findings. Suggestions for future work are also provided in Chapter 8.

Chapter 2

Background

2.1 The ocean descriptive model and wave spectra

In the simplest description of ocean waves, which are widely accepted to be sinusoidal [6], water particles move in a vertical circular motion. The vertical displacement in a water particle location due to a certain ocean wave (i) at the ocean surface from the particle's rest position is given by

$$\zeta_i(x,y,t) = A_i \cos(k_{xi}x + k_{yi}y - \omega_i t + \psi_i) \tag{2.1}$$

where A_i is the wave amplitude, k_{xi} and k_{yi} are the wave vector components in the x and y directions, respectively, ω_i is the angular frequency and ψ_i is a random phase. Equation 2.1 is one of a set of equations referred to as the Airy wave equations [6], derived by Sir G.B. Airy in 1845. It is widely understood by oceanographers that the ocean contains a wide range of waves that differ in wavelength, hence in period, and direction. Also, the ocean wave system is considered to be linear such that the ocean surface elevation ζ due to all ocean waves is given by

$$\zeta(x,y,t) = \sum_i \zeta_i(x,y,t) = \sum_i A_i \cos(k_{xi}x + k_{yi}y - \omega_i t + \psi_i). \tag{2.2}$$

Figure 2.1 is an illustration of the principle of linear superposition of ocean waves. Considering $\zeta_0, \zeta_1 \ldots \zeta_\infty$ to be statistically independent random variables with the same distribution, regardless of the distribution type, the central limit theorem states that ζ has a Gaussian distribution [19]. The probability that a random water particle at the ocean surface has an elevation of ζ is given thus by

$$p(\zeta) = \frac{1}{\sigma_n \sqrt{2\pi}} e^{-\zeta^2/2\sigma_n^2}, \tag{2.3}$$

where σ_n is the standard deviation and the mean is assumed to be 0. By taking the origin $x = y = 0$ in Equation 2.1, without loss of generality, the average energy per unit area of the ocean surface, E_t, is given by

$$E_t = \sum_i \zeta_i^2 = \sum_i 0.5A_i^2 = \sum_i E_i, \tag{2.4}$$

where E_i is the energy content of the ocean wave (i). Equation 2.4 shows that the total wave energy is the linear superposition of the energy content of individual waves. The frequency wave spectrum $E(f)$, where $f = \omega/2\pi$ is the ocean wave frequency in Hertz (Hz), is a useful representation of the contribution of individual ocean waves to the total wave energy. $E(f)$ is also referred to in the literature as 'the omnidirectional spectral density function' or 'non-directional wave spectrum'. It must be noted that f is a continuous variable. This follows since, in practice, ocean waves might occur at any frequency. The relationship between E_t and $E(f)$ is given by

$$E_t = \int E(f)df. \tag{2.5}$$

Sea state parameters, such as peak and mean wave period, may be estimated using $E(f)$, which describes the ocean system energy distribution in terms of ocean wave frequency, i.e. wave periods.

The wave spectrum $E(f)$ does not include any directional information about the ocean waves although different ocean waves with the same frequency might have different directions. Therefore, ocean waves cannot be distinguished using ocean wave frequency alone. In order to include the directional information about ocean waves in the ocean wave system representation, a more detailed wave spectral representation referred to as the directional wave spectrum $E(f,\theta)$ is used. $E(f,\theta)$ describes the ocean wave system energy in terms of wave frequency as well as the direction θ of ocean waves.

Figure 2.2 shows examples of both spectra; $E(f)$ and $E(f,\theta)$. The frequency wave spectrum shown in Figure 2.2a has a peak at $f = 0.085$ Hz. This means that the ocean waves with a period of $1/0.085 = 11.7$ s had the biggest share of the energy content of the ocean system at the time when the data was recorded. The sea state, which is an index measure of the calmness/roughness of the ocean system, is proportional to the total energy stored in the ocean system or, equivalently, the area under the frequency wave spectrum curve. Again here, no directional information can be retrieved from Figure 2.2a about any of the ocean waves in the system. Now, looking at the directional wave spectrum shown in Figure 2.2b, it can be seen that the peak wave is actually located at azimuth direction of 75° clockwise from true north.

Generally, the ocean wave system is a combination of different types of waves including wind waves, swell, tide waves, and possibly tsunami waves. However, the frequency and directional wave spectra are best used to represent wind waves and swell [9]. Wind waves and swell of interest are within the range of 50-150 metres. The wind waves are generated when local winds blow on the ocean surface for a sufficient period of time, while a swell is basically wind waves that were generated somewhere else and have traveled to the observation area. The main factors that proportionally contribute to the energy stored in a wind wave are the wind speed, the wind duration and the fetch. The fetch is the ocean surface area being affected by the wind. While traveling away from the fetch area where the waves are no longer affected by the wind, swells with higher energy, which are typically longer waves, move faster and eventually over take those with less energy. Due to this fact, swell peaks tend to appear narrower than wind wave peaks in wave spectra most of the time. However this is not always true and it really depends on the ocean system at the moment. Therefore, it can be a challenge to discriminate between wind waves and swell in wave spectra. The commercial system WAMOS II uses an adjustable variable period limit, with a default value of 9 s, to decide whether a wave system is wind sea or swell. A wave system with mean period larger than the pre-set period limit variable is identified as swell system. Otherwise, the wave system is identified as wind sea. For example, the wave system that appears in the frequency wave spectrum shown in Figure 2.2a may be regarded as swell since the calculated mean wave period of the system is 10.5 s.

2.2 Methods of ocean wave spectra estimation using X-band marine radar

The directional wave rider buoy method is the most common and reliable method of ocean wave spectral estimation [20]. In fact, ocean wave spectra estimates generated using the wave rider buoy method are often used as ground truth to validate estimates that are generated using other methods. X-band marine radars may also be used to estimate ocean wave spectra. The X-band marine radar method may provide better mobility and flexibility in collecting data compared to wave rider buoys. This is mainly because X-band radars can collect data from a wide range area of the ocean surface, usually up to range of 5 km, compared to only one point using wave rider

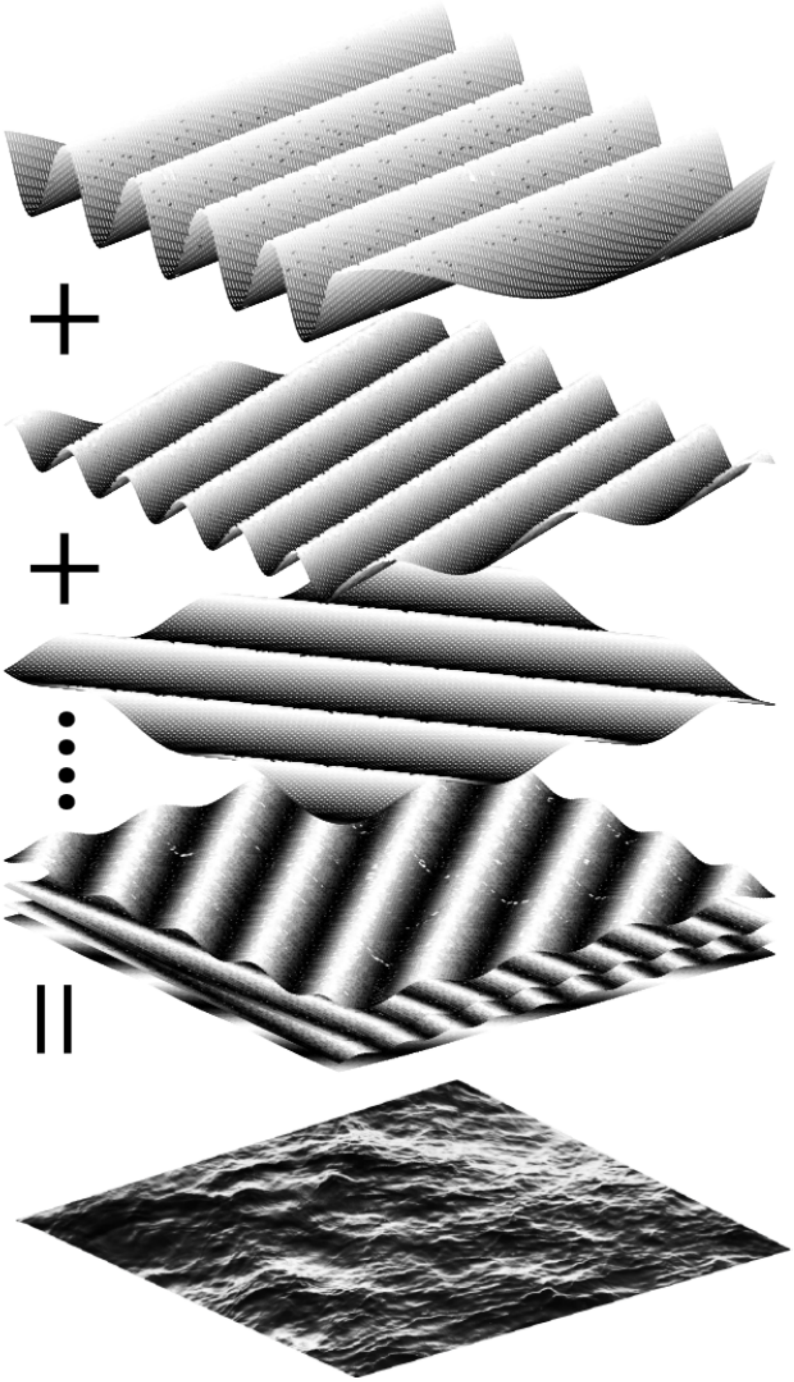

Figure 2.1: Structure of a random ocean surface.

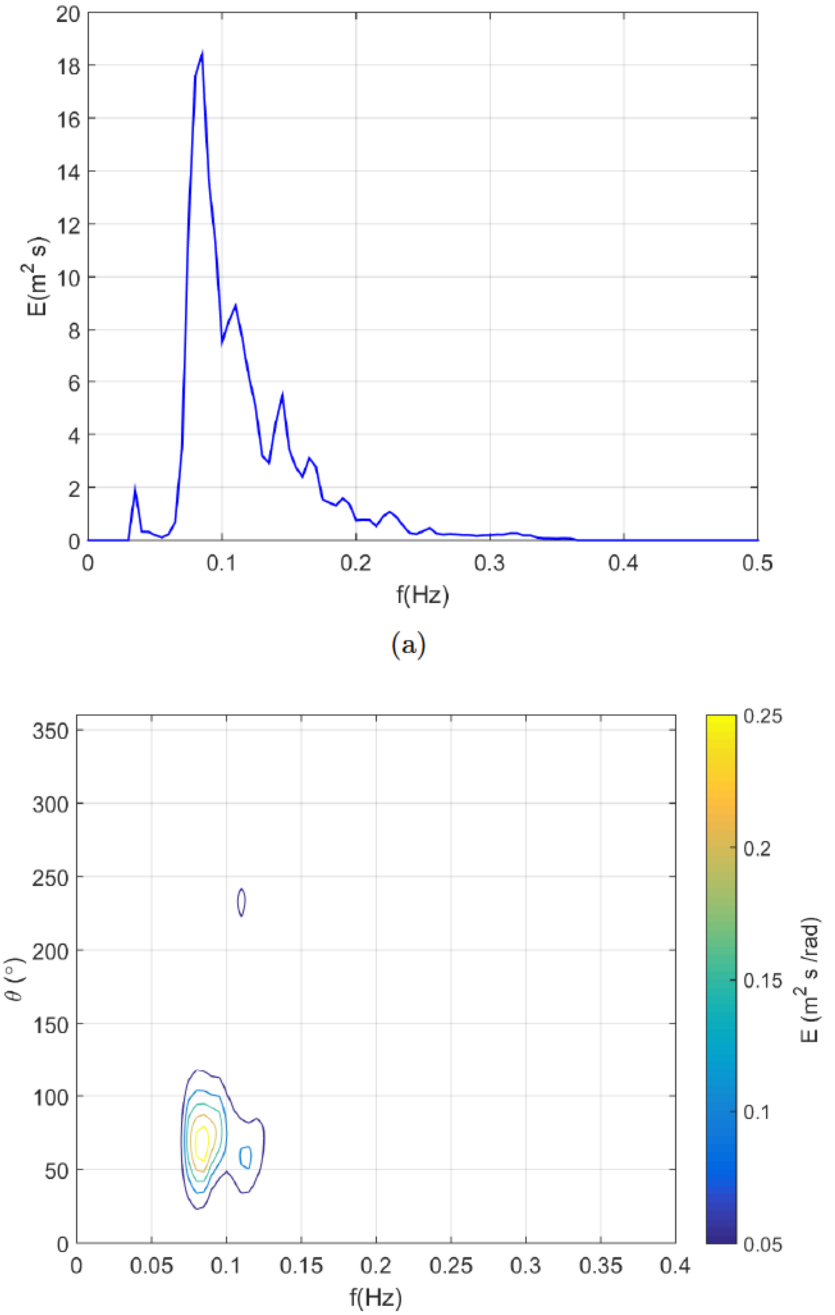

(a)

(b)

Figure 2.2: An example of ocean wave spectra (a) Frequency wave spectrum. (b) Directional wave spectrum. Spectra were estimated using a TRIAXYS wave rider buoy. Data was recorded by Defence Research and Development Canada (DRDC) on Nov 27, 2008 between 12:30 PM and 1:00 PM near Halifax, Canada.

buoys. Therefore, it is far easier to change the analysis location when using X-band marine radar compared to wave rider buoys. A buoy needs to be physically relocated in order to change the analysis location, while only changing the analysis window location within the radar range may be sufficient in the case of the X-band marine radar method. Also, in the case where the X-band marine radar needs to be relocated, it is often easier to move X-band marine radars from one point to another compared to buoys. Moreover, due to the higher spatial resolution of X-band marine radar images, spectral estimates generated using X-band marine radars are expected to be less dependent on the examination location. However, it should be noted that the method of ocean wave spectral estimation using X-band marine radar may not be able to operate independently to estimate significant wave heights [21, 22]. This can be related to the fact the radar images do not represent the actual ocean surface elevation values but relative values of it on a gray scale. Subsequently, the estimates of ocean wave spectra generated using the X-band marine radar represent relative (not actual) energy level of ocean waves. Therefore, ocean wave spectral estimates are usually calibrated using wave rider buoy data in order to produce correct significant wave height estimates.

When electromagnetic radiation from an X-band marine radar is incident on the ocean surface with angles less than 70°, it scatters back in a fashion that is best described by Bragg scattering [23]. In this type of scattering, the returned electromagnetic power is proportional to the energy of the ocean wave that satisfies the Bragg condition [23]

$$\lambda_w = \frac{\lambda_e}{2\cos(\phi)},$$

where λ_w and λ_e are the wavelengths of the ocean wave and electromagnetic radiation, respectively, and ϕ is the angle between the incident electromagnetic radiation and the mean ocean surface as shown in Figure 2.3. Since X-band marine radars operate in

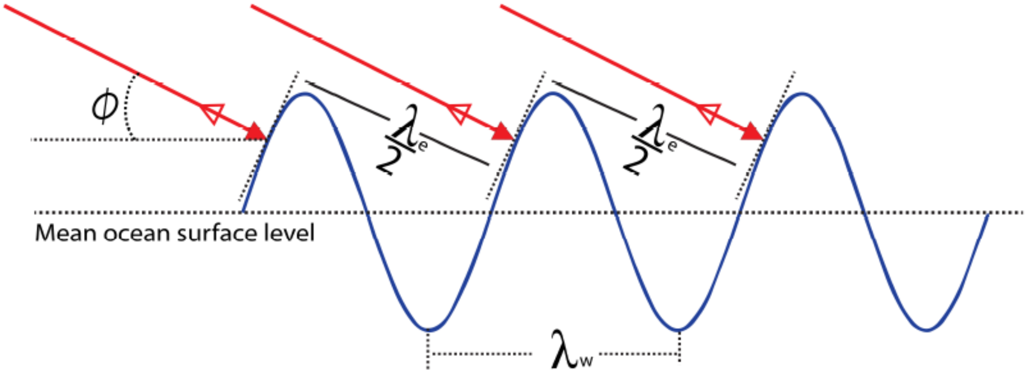

Figure 2.3: An illustration of Bragg scattering.

the frequency range of 8-12 GHz ($\lambda_e = 2.5-3.75$ cm) [24], the ocean waves that satisfy the Bragg condition have wavelengths of $\lambda_w = 1.25 - 3$ cm. Such centimetre-scale ocean waves/ripples are mainly generated by the frictional forces between the ocean surface and local winds with a minimum speed of 3 m/s [25]. Figure 2.4, which is taken from [1], shows the dependency of the normalized radar cross section area, which is a representation of the returned scatter intensity, on the wind speed. It should be noted that the data used in Figure 2.4 was acquired using a 15 GHz radar. However, the results are still valid for X-band radars since Bragg scattering is the dominant scattering in both cases. Since these ripples, which are the main reason for the returned scatter, are modulated by longer wavelength gravity ocean waves [23, 26], the returned scatter from the ocean surface is indirectly affected by these gravity ocean waves. This phenomenon is what makes it possible to estimate ocean wave spectra by studying the returned scatter from the surface.

The intensity (i.e. energy content) of ocean waves is not the only factor that contributes to the returned scatter signal. Radar imaging mechanisms, including shadowing and tilt modulation, also influence the returned scatter [10, 12, 18, 23, 27–29]. Geometric and partial shadowing are expected to occur during the radar imaging process [27]. Geometric shadowing occurs when waves with higher heights hide the shorter ones following the principle of geometrical optics. On the other hand, partial shadowing occurs when those hidden waves still produce returned scatter which is dependent on factors such as diffraction and polarization. In the case of X-band marine radar, partial shadowing effect is usually neglected due to the shorter radar electromagnetic wavelength (i.e. few centimetres) compared to those of the measured ocean wind waves (i.e. typically tens of metres). However, the shadowing behavior in the imaging process is still not fully understood. Tilt modulation can be also described by analogy to geometrical optics, whereby radar signals with small incident angle are expected to have stronger returns [11]. Polarization also influences the intensity of the returned scatter from the ocean surface. It was reported in [30] that the normalized radar cross-section area is 5 dB less when using the horizontal (HH) polarization compared to the vertical (VV) polarization at a grazing angle of 40° as depicted in Figure 2.4, which is taken from [11]. Furthermore, it was demonstrated in the Four Frequency Radar (4FR) study, which was conducted by the US Naval Research Lab (NRL) [1, 31] that the intensity of the return scatter and its dependence on the polarization are affected by the incident angle. Figure 2.5, which is taken from [1], shows the dependency of the returned scatter intensity on polarization and grazing angle.

Usually, the returned scatter is referred to as sea clutter and commonly consists of alternating illuminated and shadowed areas which form a strip-like pattern (see Figure 2.6). This sea clutter can be analyzed using methods such as the Cartesian Fourier Transformation (CFT) to estimate ocean wave spectra. This method was first introduced by Young *et al.* [10] in 1985. CFT-estimated ocean wave spectra can be used to estimate valuable sea state parameters such as surface current, wave period, direction and significant wave height. Other ocean-related information such as wind vectors [32–38] and bathymetry [39–41] can also be derived from CFT-estimated

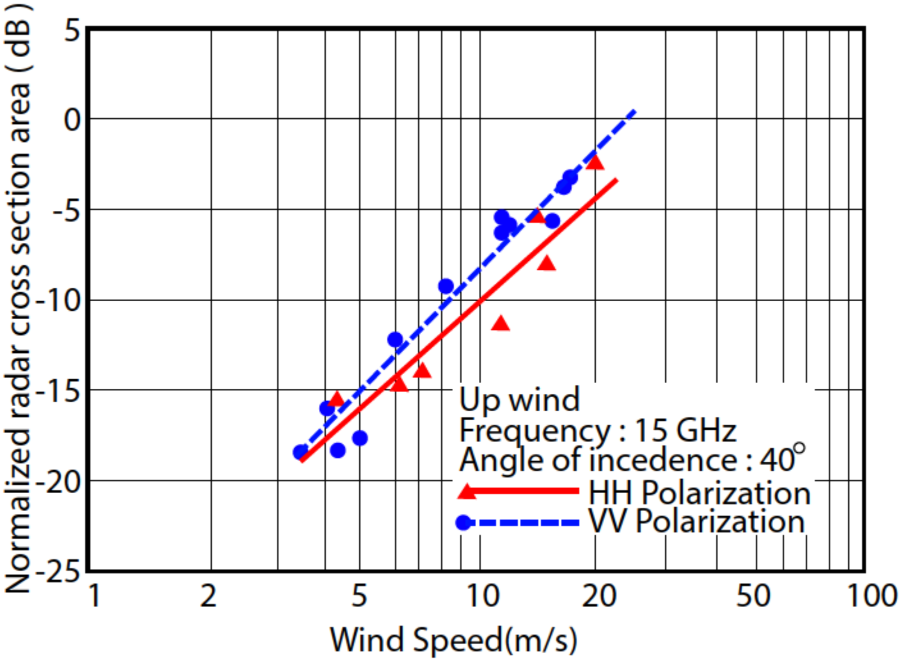

Figure 2.4: General trend in returned scatter intensity with wind speed for vertical (VV) and Horizontal (HH) polarization. Plot is taken from [1].

ocean wave spectra.

Since its first introduction, the CFT spectral estimation method has been significantly improved and many studies have been carried out to make the method more robust and accurate [11, 29, 42–44]. Surface current estimation using the CFT method has received a good deal of attention in the literature due to its key role in excluding the non-wave components from the estimated wave spectra [18, 45, 46]. Another problem that has been addressed in the literature is the effect of shadowing and tilt modulation on the CFT-estimated wave spectra. Using a Modulation Transfer Function (MTF) to compensate for distortion in the wave spectra due to shadowing and tilt modulation is perhaps the most popular approach [29, 44, 47, 48]. Other studies have addressed the dependency of the returned radar signal strength on the relative azimuth direction between the peak ocean wave direction and the radar beam direction [12, 18].

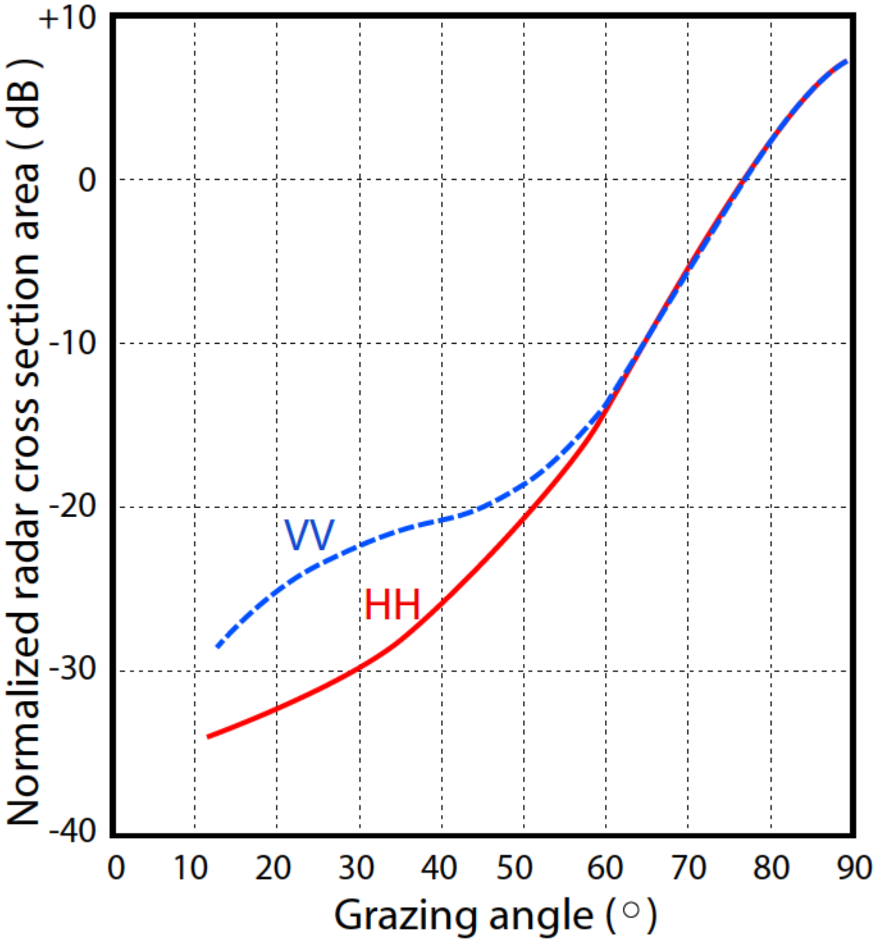

Figure 2.5: General trend in returned scatter intensity with the grazing angle for vertical (VV) and Horizontal (HH) polarization based on the US Naval Research Lab (NRL) Four Frequency Radar (4FR) data. Plot is taken from [1].

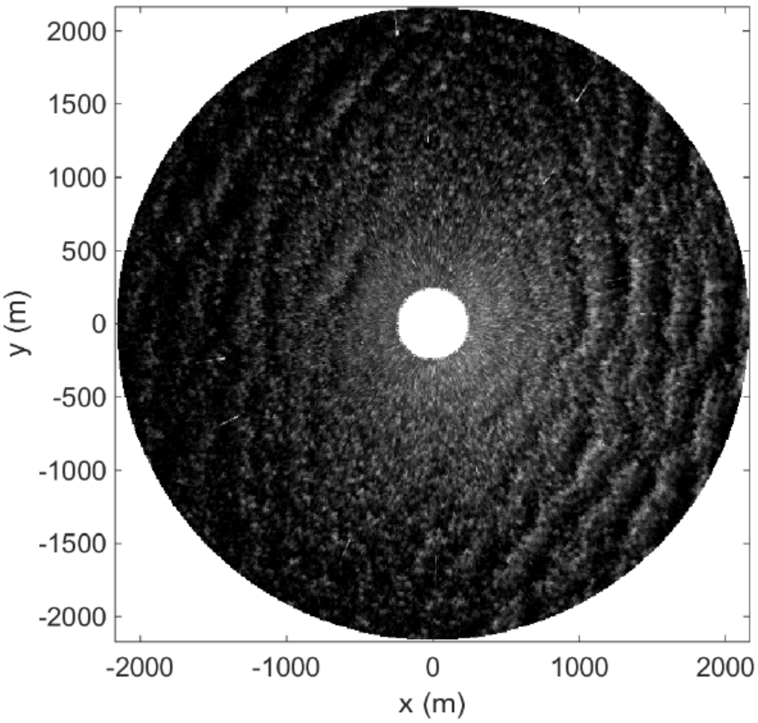

Figure 2.6: An example of sea clutter. Image was generated using an X-band radar by Defence Research and Development Canada (DRDC)[Dec. 01, 2008, Atlantic ocean near Halifax].

In spite of being the most popular method, it should be noted that the CFT is not the only method of sea state parameters estimation from X-band marine radar. Wavelet transforms may be used for that purpose [49]. Another recent study by Chen *et al.* [50] proposed a new algorithm to estimate sea state parameters from X-band marine radar images using empirical orthogonal functions.

In the next section, a detailed overview of ocean wave spectral estimation using the CFT method is presented.

2.3 A review of wave spectral estimation using X-band marine radar

X-band marine radars illuminate the ocean surface with electromagnetic pulses at different directions to cover a specific azimuth range. Output samples are generated by collecting the returned scatter during consecutive time intervals. A sample's range (i.e. distance from the radar) is determined by the round-trip travel time between sending and receiving a radar pulse, while the azimuth location of the sample is considered to be the antenna direction at the moment of pulse transmission [1, 51]. Typically, X-band marine radars make a full azimuthal rotation every 1-2 s with range and azimuth resolutions of 1-10 m and $\sim 0.35°$, respectively. This configuration of data output, in which samples are naturally digitized on a polar grid, is referred to as B-scan format. The first step in the process of ocean wave spectra estimation using X-band marine radar and before applying the Cartesian Fourier Transformation (CFT) is to convert consecutive radar B-scan images to Cartesian images $I(\mathbf{r}_n)$ using a processes referred to as 'scan conversion', where $\mathbf{r}_n = (x_n, y_n, t_n)$ is the discrete space-time vector, $n = 0 \ldots N-1$, and N is the number of elements in the space-time domain. Section 2.3.1 of this chapter includes a review of the scan conversion process while a review of the CFT method is found in Section 2.3.2.

2.3.1 Scan conversion

Scan conversion is used to convert B-scan images to Cartesian images in order to apply the CFT. The use of a look-up Table (LUT) is a popular method for scan conversion [52]. In the initial stage of the method, a reference mapping table is created and then used to convert all B-scan images that are generated using the same set of radar parameters. Each element of the table corresponds to an individual sample of the B-scan image and can hold indices of multiple Cartesian image samples. In programming, this is often implemented using a table of linked lists [1]. In Figure 2.7, which illustrates the structure of a LUT, each block belongs to an individual B-scan image sample with indices (r_i, φ_i), where $r_i = 0 \dots R_i - 1$ and $\varphi_i = 0 \dots \Phi_i - 1$, and represents a list of its related Cartesian image indices (x_i, y_i), where $x_i = 0 \dots X_i - 1$ and $y_i = 0 \dots Y_i - 1$. X_i and Y_i represent pre-specified numbers of samples in the x and y directions, respectively, of the scan-converted images. For example, it can be seen in Figure 2.8, which is a not to scale illustration of the scan conversion process, that the B-scan sample $(r_i, \varphi_i) = (128{,}0)$ covers the Cartesian samples $(x_i, y_i) = (256{,}384)$, $(257{,}384)$, and $(258{,}384)$. Therefore, these Cartesian samples are added to the list of $(r_i, \varphi_i) = (128{,}0)$ as shown in Figure 2.7.

The LUT is created using a two-stage algorithm involving inverse and forward mapping. The algorithm starts with the inverse mapping in which the Cartesian image indices (x_i, y_i) are assigned to the B-scan image indices (r_i, φ_i) via the relation

$$r_i = \left\lfloor \frac{\sqrt{((x_i - X_i/2)\Delta_x)^2 + ((y_i - Y_i/2)\Delta_y)^2}}{\Delta_r} + 0.5 \right\rfloor$$

$$\varphi_i = \left\lfloor \frac{1}{\Delta_\varphi} \left(5\pi/2 - \operatorname{atan2}\left(\frac{(y_i - Y_i/2)\Delta_y}{(x_i - X_i/2)\Delta_x} \right) - \Phi_{in} \right) + 0.5 \right\rfloor \mod \Phi_i,$$

where $\Delta_x, \Delta_y, \Delta_r$ and Δ_φ are the sampling resolutions in the x, y, range and azimuth directions, respectively, and Φ_{in} is the initial B-scan azimuth direction clockwise from true north. It should be noted that the mapping process here is not necessarily one-to-one. After the inverse mapping is performed, some B-scan samples might have been left 'un-hit' (not assigned to any Cartesian samples). Therefore, the forward

---

[1] A linked list is a linear collection of objects referred to as nodes. Each node consists of a variable to hold data, Cartesian indices in our case, and a link to the next node in the list [53].

mapping is implemented such that an un-hit B-scan sample (r_o, φ_o) is assigned to a Cartesian sample that is given by

$$x_i = \left\lfloor \frac{r_o \Delta_r \cos(\pi/2 - (\Phi_{in} + \varphi_o \Delta_\varphi))}{\Delta_x} + X_i/2 + 0.5 \right\rfloor$$

$$y_i = \left\lfloor \frac{r_o \Delta_r \sin(\pi/2 - (\Phi_{in} + \varphi_o \Delta_\varphi))}{\Delta_y} + Y_i/2 + 0.5 \right\rfloor .$$

Once the forward mapping is completed, the reference table is ready to be used to map B-scan samples to their corresponding Cartesian sample(s). It should be noted that it is possible for a Cartesian sample to be assigned to multiple B-scan samples. For example, in Figure 2.7, the Cartesian sample (x_i, y_i) = (256,257) is assigned to the B-scan samples (r_i, φ_i) = (1,0) and (1,1). This situation is more common near the centre of the B-scan image. In this case, the Cartesian sample is filled by the average of the corresponding B-scan samples. Figure 2.9 shows a single B-scan radar image and the Cartesian image after scan conversion. It should be noted that the start collection range of the data shown in Figure 2.9 was 225 m. This appears as a white circle at the centre of the scan-converted image in Figure 2.9.

2.3.2 The Cartesian Fourier Transform (CFT) analysis

Once the radar Cartesian images are produced using the scan conversion process, an analysis window, $f(\mathbf{r}_n)$, is selected. In this thesis, analysis windows with the size of 256×128×32 samples are used. An analysis window with this size covers 1920 m ×960 m×44.8 s with a sample resolution of 7.5 m×7.5 m×1.4 s. Traditionally, multiple analysis windows are used to minimize the dependency of wave spectra estimation on analysis window orientation. The final estimated wave spectra are acquired by averaging the wave spectra estimates from those analysis windows which are uniformly [54] or adaptively [16] distributed over the azimuth dimension. Figure 2.10 shows

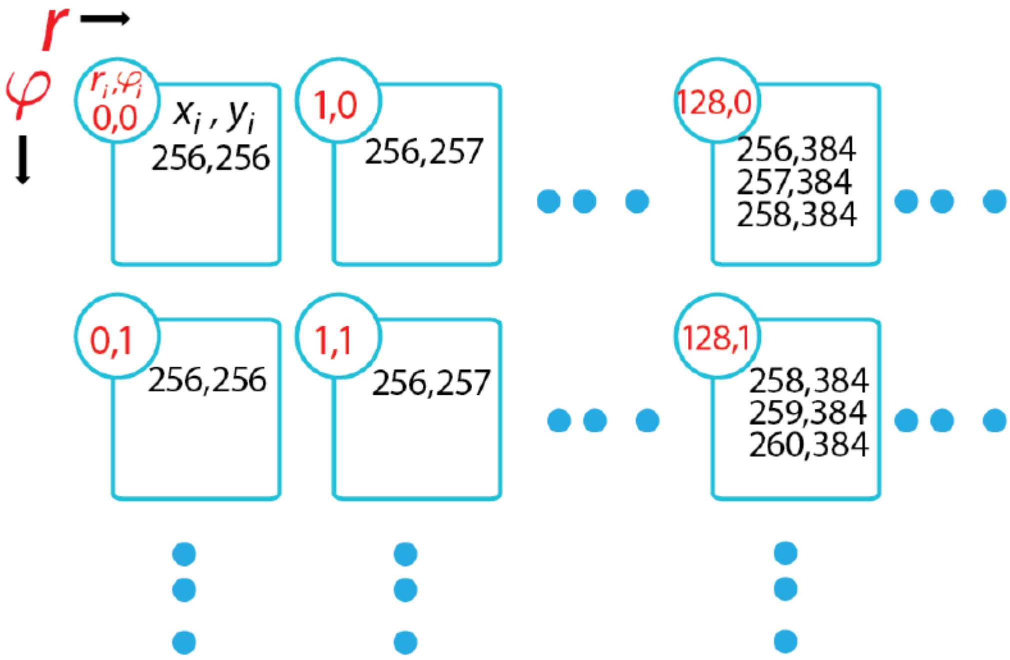

Figure 2.7: Demonstration of the structure of a LUT.

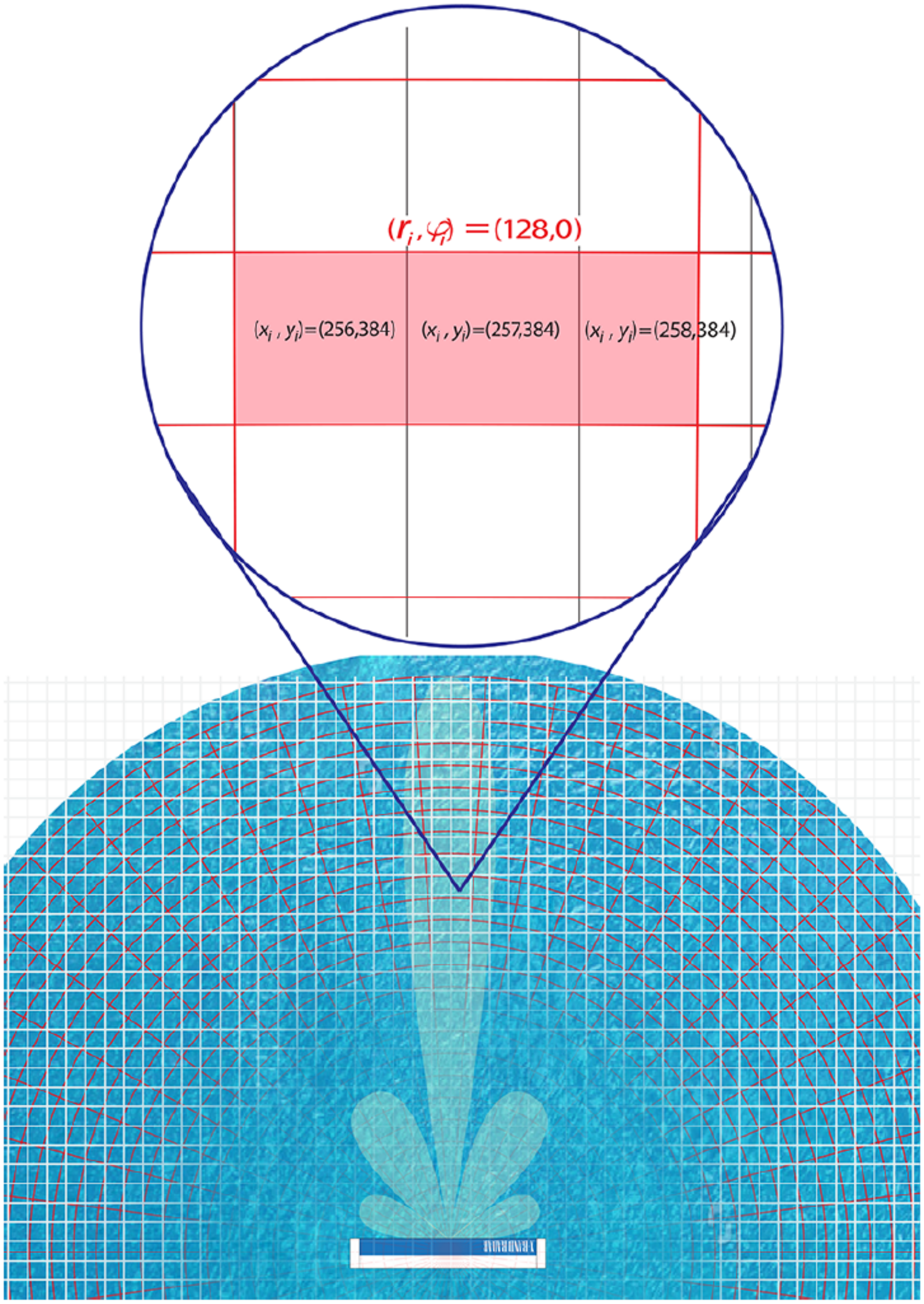

Figure 2.8: Illustration of the B-scan and Cartesian sampling grids showing the radar at the centre and the beam power pattern for one pulse. Figure dimensions are not to scale.

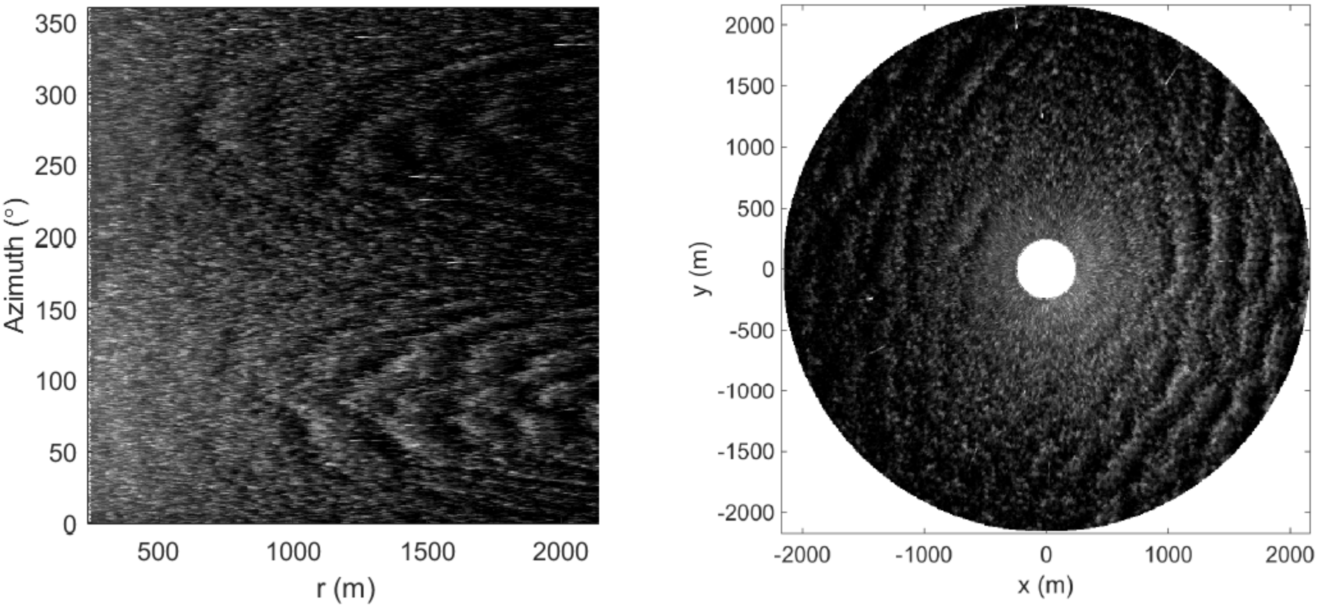

Figure 2.9: Single B-scan radar image (left). Cartesian image after scan conversion (right). Collected on Dec. 01, 2008, Atlantic ocean near Halifax.

three analysis windows of the size noted above and uniformly distributed over the full 360° azimuth range.

Once an analysis window $f(\mathbf{r}_n)$ is selected, the 3D Cartesian Fourier Transform (CFT) is applied on $f(\mathbf{r}_n)$ to evaluate the 3D image spectrum $\mathrm{F}(\mathbf{\Omega})$, where $\mathbf{\Omega}$ is the 3D wave number-frequency vector (k_x, k_y, ω) with k_x and k_y being the spatial wave vector components and $\omega = 2\pi f$ the wave angular frequency. The 3D image spectrum $\mathrm{F}(\mathbf{\Omega})$ is computed by the 3-D discrete time Fourier transform (DTFT) given by

$$F(\mathbf{\Omega}) = \sum_{n=0}^{N-1} f(\mathbf{r}_n) e^{(-j\mathbf{\Omega}\cdot\mathbf{r}_n)},$$

where N is the number of points in the discrete space-time vector $\mathbf{r}_n$. The power spectrum $\mathcal{E}$ is given in terms of F as [10]

$$\mathcal{E}(\mathbf{\Omega}) = \frac{1}{N}|F(\mathbf{\Omega})|^2.$$

The power spectrum $\mathcal{E}$ consists of components E_Ω, representing contents due to ocean

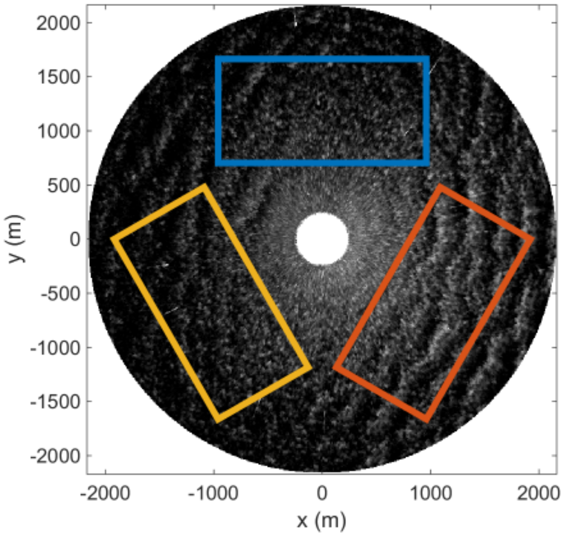

Figure 2.10: Single scan-converted radar image with 3 uniformly distributed analysis windows. Data: Dec. 01, 2008, Atlantic Ocean near Halifax, Canada.

waves and non-wave components ν, that account for the influence of noise or aliasing effects [10]. Thus, $\mathcal{E}$ may be written as

$$\mathcal{E}(\mathbf{\Omega}) = E_{\Omega}(\mathbf{\Omega}) + \nu(\mathbf{\Omega}).$$

In the case of wave spectra estimation where E_{Ω} includes the components of interest, one wishes to separate E_{Ω} from ν. Since E_{Ω} is governed by the dispersion relationship while ν is not, a component in $\mathcal{E}$ may be classified as a wave or non-wave component based on whether it obeys the dispersion relationship, given by [29]

$$\omega(\mathbf{k}, \mathbf{U}) = \sqrt{gk\tanh(kd)} + \mathbf{k}\cdot\mathbf{U}, \tag{2.6}$$

where $\mathbf{k} = (k_x, k_y)$ is the wave vector of magnitude $k = 2\pi/\lambda_w$, λ_w being the wavelength, in the direction of wave propagation $\theta = \tan^{-1}(k_y/k_x)$, d the water depth, g the acceleration due to gravity, and $\mathbf{U}$ the velocity of encounter which is the sum of the surface current velocity and the radar platform velocity. Figure 2.11 plots Equation 2.6 for four values of $\mathbf{U}$ (0, $1\angle 0$ m/s, $\sqrt{2}\angle 45$ m/s, and $2\angle 90$ m/s). It can be seen from Figure 2.11 that different values of $\mathbf{U}$ produce different shapes of the dispersion shell, around which ocean wave components are concentrated. For example, an arbitrary component $\mathcal{E}(\mathbf{k_o}, \omega_o)$ is classified as a wave component that belongs to E_Ω if $\omega(\mathbf{k_o}, \mathbf{U}) \in [\omega_o - \Delta\omega, \omega_o + \Delta\omega]$, where $\Delta\omega = 2\pi(T_s N_t)^{-1}$ is the angular frequency resolution, T_s is the radar sampling/rotating time, and N_t is the analysis window size in the time domain (i.e. the number of radar images in one set). Otherwise, it is classified as a non-wave component that belongs to ν. The velocity of encounter ($\mathbf{U}$) can be estimated using algorithms that implement the least squares method [10, 46], the normalized scalar product technique [45, 55, 56] or both [18].

Once E_Ω is extracted from $\mathcal{E}$ by excluding the non-wave components (ν), which are identified by the aid of Equation 2.6, from $\mathcal{E}$, the 2D wave spectrum $E_k(k_x, k_y)$ may be found as

$$E_k(\mathbf{k}) = 2\int_{\omega>0} E_\Omega(\mathbf{\Omega})\mathrm{d}\omega.$$

E_Ω is integrated over only positive angular frequencies (i.e. $\omega > 0$) to remove the 180° ambiguity in wave direction, which results when the entire range of angular frequencies ($-\infty < \omega < \infty$) is considered. E_k does not reflect the actual wave spectrum represented by the ground truth spectrum E_{gt} due to changes caused by the radar imaging process. Figure 2.12 is an illustration of the radar imaging process. The radar return (B-scan), shown in the upper right corner of Figure 2.12 can be seen to be proportional to the product of the sampled ocean surface elevation (lower left of Figure 2.12) and other modulation mechanisms that include shadowing (lower middle of Figure 2.12) and tilt modulation (lower right of Figure 2.12). Mathematically, the Modulation Transfer Function (MTF), which represents the change in the ocean wave spectrum due to the imaging process, can be given by

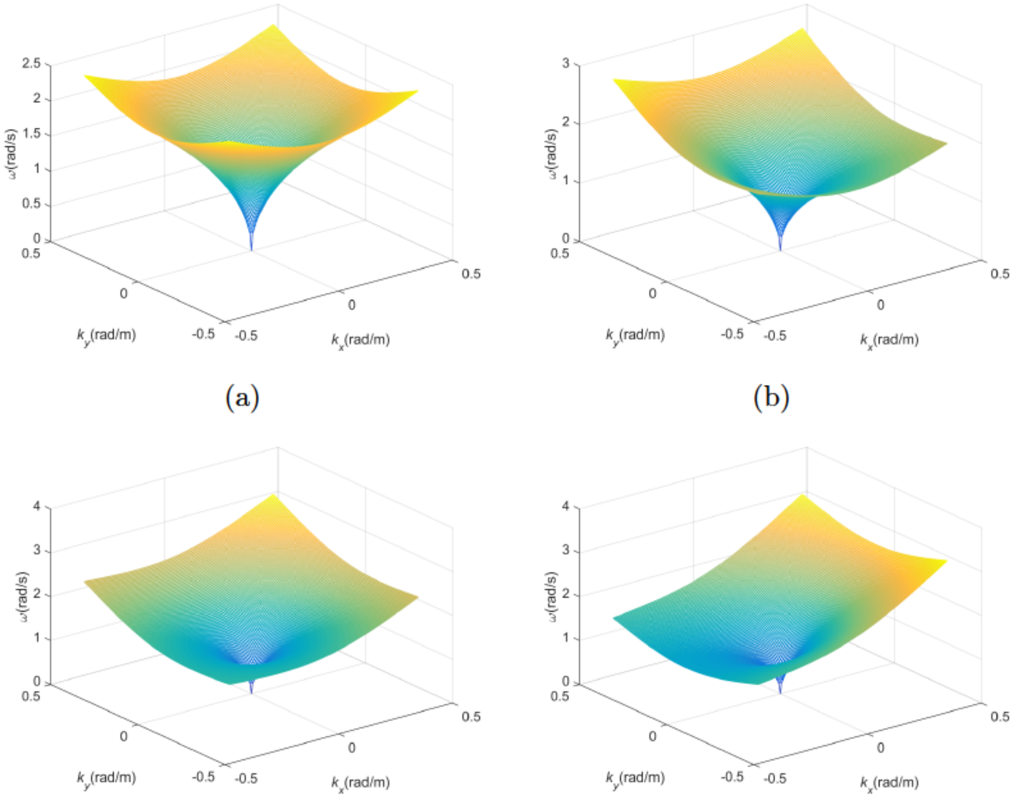

(a)

(b)

(c)

(d)

Figure 2.11: Dispersion relationship (a) $\mathbf{U} = 0$. (b) $\mathbf{U} = 1\angle 0$ m/s. (c) $\mathbf{U} = \sqrt{2}\angle 45$ m/s. (d) $\mathbf{U} = 2\angle 90$ m/s.

$$M(\mathbf{k}) = E_k(\mathbf{k})/E_{gt}(\mathbf{k})$$

where E_{gt} is the ground truth directional wave spectrum. It should be noted that the MTF is meant to improve the shape of wave spectra. However, it does not calibrate wave spectra to reflect actual energy values. Unfortunately, it is quite difficult to characterize $M(\mathbf{k})$ due to the nonlinear nature of the imaging mechanisms and their dependency on the ocean state which is, at this stage, yet to be estimated. Nevertheless, empirical attempts have been made to find a mathematical form of $M(\mathbf{k})$ [11, 48]. Perhaps the Borge *et al.* model [11] is the most popular one and is given by

$$M(\mathbf{k}) = k^{\beta}$$

where β is a constant and that has been found to be in the range of 1.2. This value was found empirically using field and simulated data [11]. The simulations implemented both shadowing and tilt modulation as these are considered to be the main contributors to the MTF. The corrected directional wave spectrum E_c, which is a better estimate of E_{gt}, can then be given by

$$E_c(\mathbf{k}) = k^{-\beta} E_k(\mathbf{k}). \tag{2.7}$$

Even though using a value of $\beta = 1.2$ produced reasonable results for many cases of the field data used in this thesis, in a significant number of cases it did not. For example, in some cases $\beta = 0.8$ worked best, while $\beta = 2$ gave better results for other cases by comparison with the ground truth spectra. Chen *et al.* [48] have also reported that $\beta = 1.2$ might not work best for complex sea states and proposed a new MTF for near shore applications.

Subsequently, the directional wave spectrum $E_c(\mathbf{k})$, which is presented in the Cartesian coordinates, can be equivalently represented in polar coordinates by $E(f, \theta)$

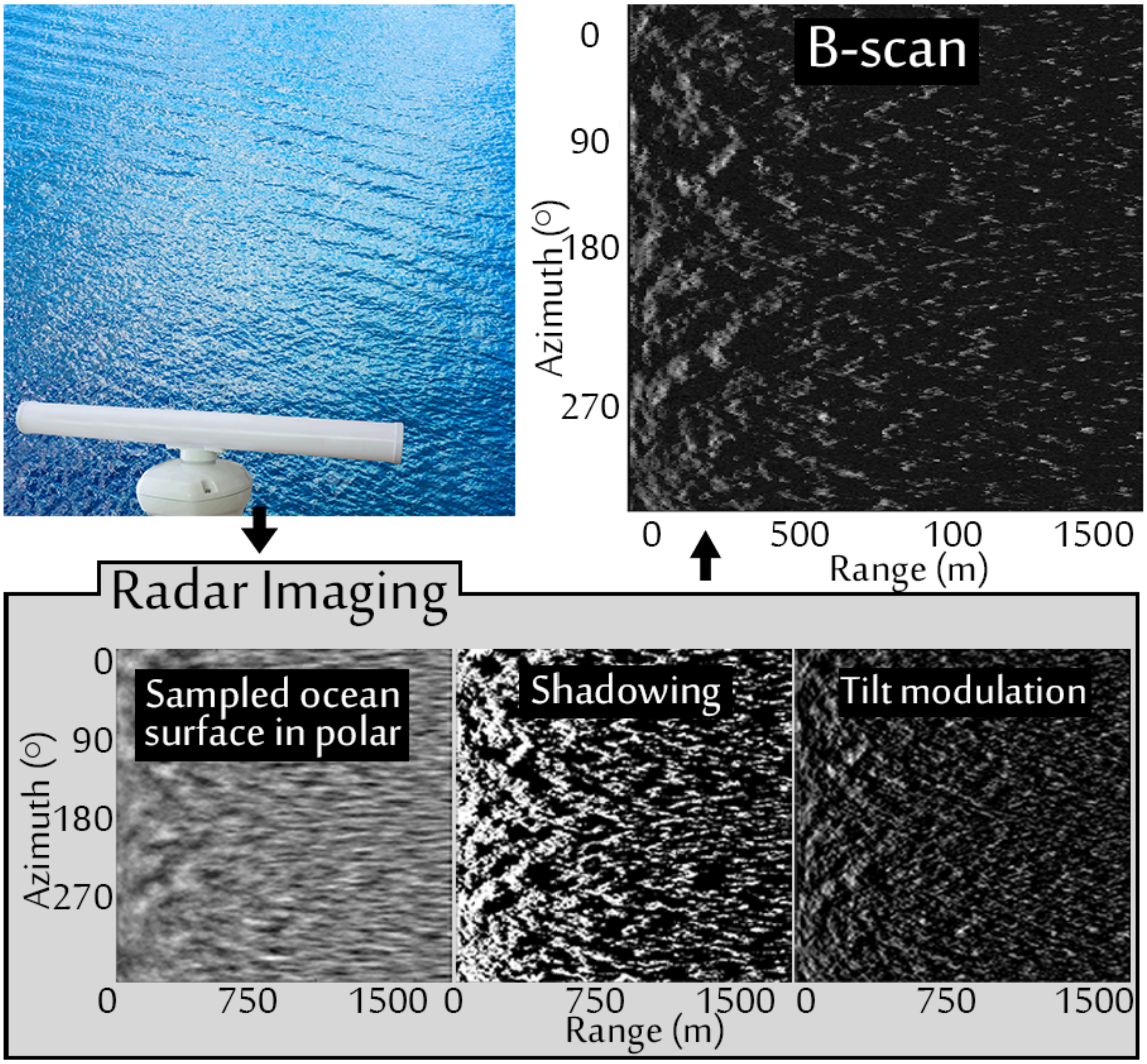

Figure 2.12: Illustration of the radar imaging process. Simulation was used to generate B-scan (upper right), ocean surface elevation (lower left), shadowing signal (lower middle), and tilt modulation signal (lower right).

via the transformation [10]

$$E(f,\theta) = E_c(\mathbf{k})k\frac{\mathrm{d}k}{\mathrm{d}f},$$

where $f = \omega/2\pi$ is the ocean wave frequency in Hz, and $k\mathrm{d}k/\mathrm{d}f$ is the Jacobian of the transformation between the coordinates $\mathbf{k} = (k_x, k_y)$ and (f, θ). The frequency spectrum $E(f)$ is given by

$$E(f) = \int_{-\pi}^{\pi} E(f,\theta)\mathrm{d}\theta.$$

Once the directional and non-directional wave spectra are acquired, sea state parameters, such as ocean wave period and direction, can be estimated by means of a stochastic approach [57–59]. The n^{th} spectral moment m_n is defined as

$$m_n = \int_0^{\infty} f^n E(f)\mathrm{d}f. \tag{2.8}$$

The zero-crossing period is given by $T_z = (m_0/m_2)^{1/2}$, the mean period $T_{01} = m_0/m_1$, and the peak wave period $T_p = 1/f_p$ where f_p is the peak frequency [6]. The n^{th} directional moments A_n and B_n are given by

$$A_n(f) + jB_n(f) = \frac{1}{\pi}\int_0^{2\pi} e^{jn\theta}E(f,\theta)d\theta,$$

and the mean direction is given by

$$\theta_m = \tan^{-1}\frac{B_1(f)}{A_1(f)}.$$

Using Equation 2.8, the first moment m_0 is given by

$$m_0 = \int_0^{\infty} E(f)\mathrm{d}f.$$

Clearly, m_0 represents the total energy or variance in the wave system (see Equation 2.4) and indicates the severity of the ocean conditions.

In practice, the significant wave height, $H_s = 4.01\sqrt{m_0}$ [6, 57], is commonly used to represent the severity of the ocean conditions. H_s is defined as the average of the highest one-third estimated wave heights [6]. Since B-scan radar images do not reflect the actual elevation of the ocean surface but rather a relative value on the grayscale, E_Ω, which is calculated from the B-scan images, do not reflect the actual ocean wave energy but a scaled version of it. For the estimation of most sea state parameters such as ocean wave period and direction, E_Ω is adequate. However, for the significant wave height analysis, a properly scaled wave spectrum that reflects the actual ocean wave energy is needed. Traditionally, supportive buoy data is used to calibrate E_Ω. This is considered an application shortcoming of the marine radar-based methods in wave spectra estimation [21]. A recent study by Gangeskar [60] proposed a new method that uses shadowing in radar images to estimate the significant wave height without the need for calibration. Subsequently, several studies used this approach to enhance significant wave estimation [61–64]. Significant wave height analysis is beyond the scope of this thesis. The evaluation of the proposed methods in this thesis mainly involves the analysis of other sea state parameters including wave periods and direction.

2.4 Data Overview

The field data used in this thesis were collected near Halifax, Nova Scotia, on the East Coast of Canada by Defence Research and Development Canada (DRDC) (see Figure 2.13 and Table 2.1) by shipborne Decca and Furuno X-band nautical radars over a 10 day period (Nov 25 - Dec 4, 2008). A TRIAXYS wave rider buoy, which generated a reading every 30 minutes, was also used to validate the marine radar-derived results from the proposed methods in this thesis. During the experiment, there was a drift of 41 km in the wave buoy location. However, the radars were always within a 10 km distance of the buoy during the experiment. Hence, no significant statistical differences are expected between measurements at the locations of the buoy and radars in the experiments.

Figure 2.14 displays the wind speed and direction during the experiment. It should be noted from Figure 2.14 that at some instances, the wind speed dropped below 3 m/s. At such low wind speed, ocean wave signatures in X-band radar images might not be sufficient to produce ocean wave spectra estimates [54]. Furthermore, high precipitation was observed at some other instances during the experiment as shown in Figure 2.15. Rain might contaminate X-band radar images and corrupt wave spectra estimates from X-band radar data [54]. In order to eliminate the potential discrepancies due to low wind speed or high precipitation in our analysis, the performance validation of the proposed methods in this thesis was based only on the wave spectra estimates that achieve a minimum agreement of 40% with the ground truth (see Section 3.4.2 for agreement calculation). Figure 2.16 shows the significant wave height information recorded by the TRIAXYS wave rider buoy during the experiment. Except for a few hours on Nov 28, it can be seen from Figure 2.16 that the sea state mostly varied between moderate and rough (1 m/s $< H_s <$ 5 m/s). It should be noted that no X-band radar data were recorded during those few hours on Nov 28 when the significant wave height exceeded 7 m/s.

The radars, which were connected to a Wave Monitoring System II (WaMoS II) [54], were operating at 9.4 GHz with HH polarization and at grazing incidence. The radar system recorded the returned scatter signal on a value scale of 0 to 255 and saved the data samples in 8-bit unsigned integers format. Between the two radars, since the shortest radars' antenna rotational time was 1.44 s (Furuno), the frequency spectrum analysis and comparison are limited in this thesis to the range of 0.05 to 0.35 Hz. For the chosen analysis window size of 256×128×32, a single estimate of

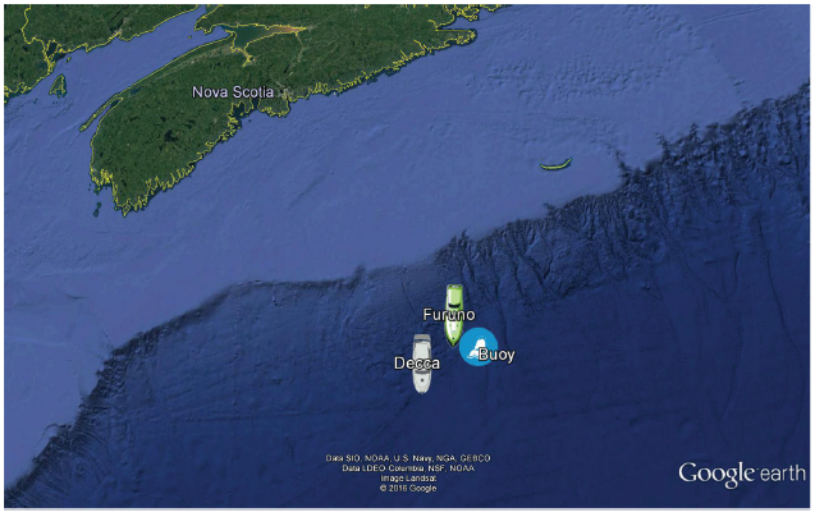

Figure 2.13: Locations of wave buoy and radar during the experiment on Dec. 01, 2008.

ocean wave spectra using radar methods requires 32 images, which needs 80 s and 44.8 s to be generated by Decca and Furuno radars, respectively. This size of analysis window was chosen over other popular sizes, e.g. 128×128×32, to cover a larger azimuth range in order to mitigate the dependency of wave spectral estimation on the azimuthal dimension. It should be noted that the generation rate of ocean wave spectral estimates of the radar methods (the CFT and the proposed methods in this thesis) is different from the buoy method. Thus, for compatible comparisons between the radar and buoy estimates, radar estimates generated during the 30 minute window of a buoy estimate generation are averaged for comparison with that buoy estimate. The ground truth buoy directional wave spectrum has a resolution of 0.005 Hz ×3° and covers a range of 0.030 to 0.465 Hz and a full range of 360°. Further details about the experiment are listed in Table 2.1.

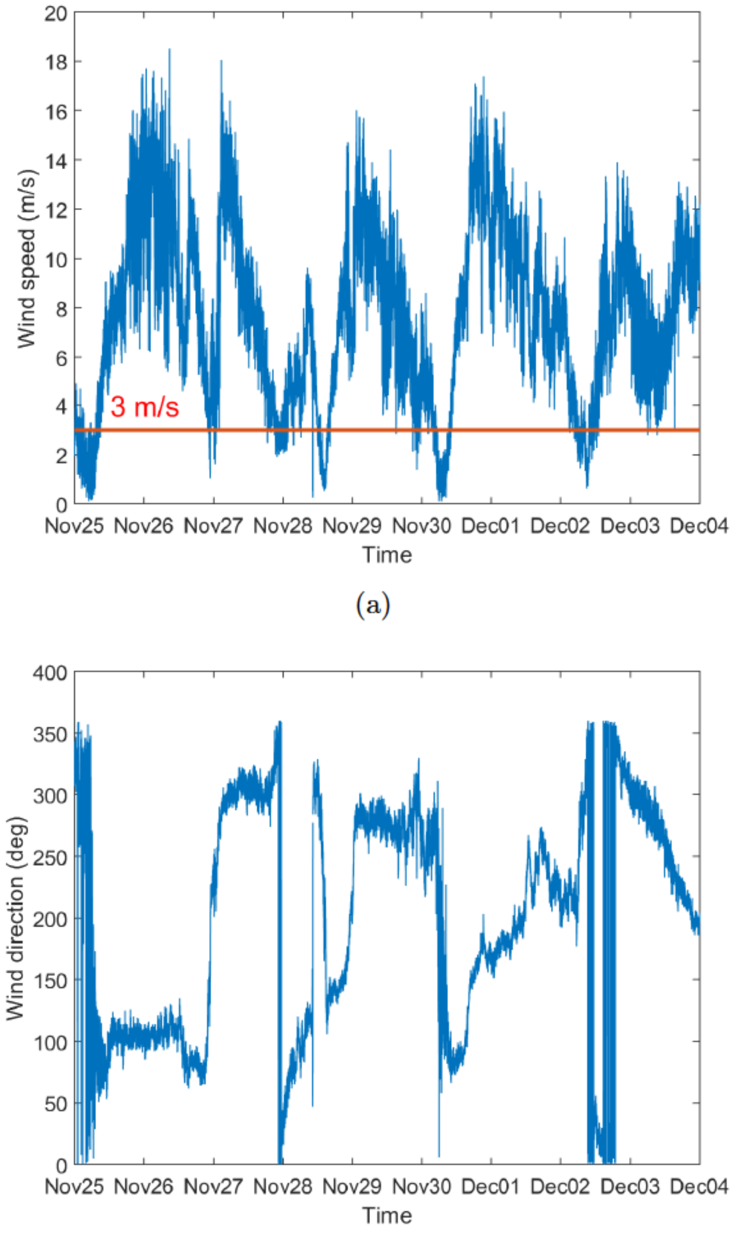

(a)

(b)

Figure 2.14: Wind speed (a) and direction (b) during the field experiment.

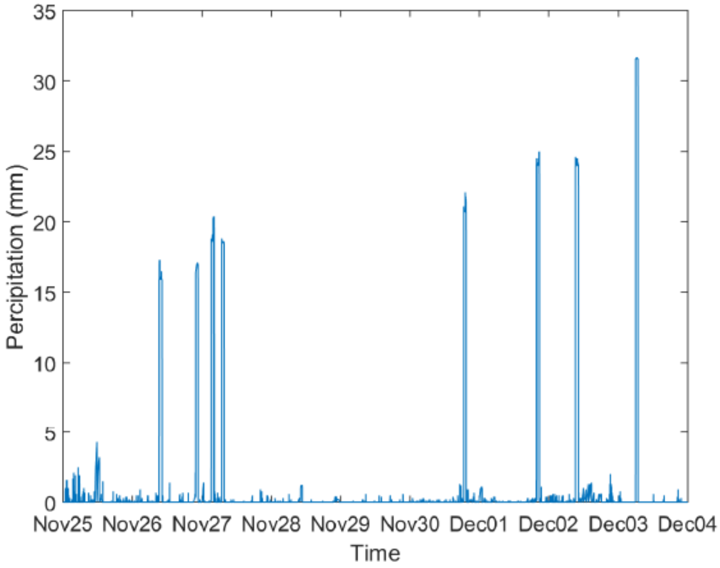

Figure 2.15: Precipitation recorded during the field experiment.

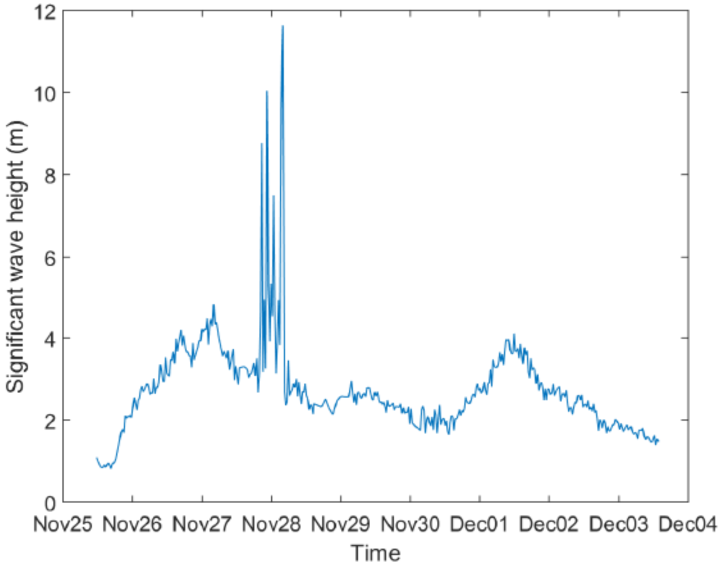

Figure 2.16: Significant wave height recorded during the field experiment.

Table 2.1: Experiment setup: radar and buoy parameters.

Experiment location	42° 22.4391 N 61° 55.5654 W
Antenna rotational time	Decca: 2.5 s, Furuno 1.44 s
Antenna height	Decca: 21.9 m, Furuno 16.5 m
Sampling frequency	20 MHz
Range resolution	7.5 m
Radar pulse length	50 ns
Range coverage	240 - 2160 m
Azimuth coverage	360°
Pulses per sweep	1000
Water depth	200 m
Polarization	Horizontal
TRIAXYS wave period range	1.6 to 33.3 s
TRIAXYS wave period accuracy	better than 1%
TRIAXYS wave direction range	0 to 360°
TRIAXYS wave direction accuracy	1°
TRIAXYS Heave range	±20 m
TRIAXYS Heave resolution	0.01 m
TRIAXYS Heave accuracy	better than 2%
TRIAXYS Compass accuracy	±0.5°
TRIAXYS GPS	12 channel

Chapter 3

An Adaptive Method of Wave Spectra Estimation Using X-Band Marine Radar

3.1 Introduction

The purpose of this thesis is to develop wave spectra estimation methods that provide more accurate and reliable estimates compared to the standard CFT method. In one of the early steps of the CFT method, one or multiple analysis windows of the full azimuth range of radar data are chosen to perform the CFT analysis. Choosing a different number or orientation of the analysis windows may change the accuracy of the estimate. Traditionally, this problem has been addressed by using multiple windows that are uniformly distributed over the full azimuth range. The final directional wave spectrum is calculated by averaging the directional wave spectra from different analysis windows. In this chapter, the dependency of wave spectra estimation on the orientation of the analysis windows is studied with the intention of developing an algorithm that determines the number and orientation of the analysis windows such that the output is most accurate and reliable.

3.2 The Wave Spectrum Estimation Dependency on the Orientation of the Analysis Window

In wave spectrum estimation using marine radar images, the dependency on the azimuth direction of the analysis window is not due to a hydrodynamical property of the ocean waves. Rather it is due to the imaging process [16, 65]. Several imaging mechanisms including the intensity variation in the up/down wave direction due to Bragg scattering, shadowing, and tilt modulation contribute to this dependency. The Bragg scattering contribution can be explained by the concentration of the centimetre-scale roughness on the up-wave surface of the wind waves. Since this roughness is responsible for Bragg scattering, it is expected that there will be a stronger returned radar signal from the up-wave direction than from other directions. Even though some studies [27] presented analysis on the shadowing formation in X-band radar images, the shadowing contribution to the estimated wave spectrum using X-band radar data is not fully understood. However, evidence was presented in [12] that shadowing induces higher harmonics in radar images of the ocean surface.

In order to investigate how shadowing and tilt modulation contribute to the wave spectra estimation dependency on the orientation of analysis windows, a simulated ocean surface elevation using the parameters listed in Table 3.1 and the input directional spectrum shown in Figure 3.1a were implemented. The simulation was generated using a Pierson-Moskowitz-based power distribution model recommended by the 15th International Towing Tank Conference (ITTC) [66] and a squared cosine distribution (accounting for angular spreading) [29], with random phases that were generated using a uniform distribution. Figure 3.1b shows a sample of the simulated surface elevation. The shadowing and tilt modulation masks were calculated for the simulated image sets using the model proposed by Nieto *et al.* [29]. Figures 3.1c and 3.1d show the shadowing and tilt masks, respectively. The shadowing percentage is calculated at near, mid and far range as a function of θ. At a given angle θ_0, the shadowing percentage is quantified as the number of shadowed samples within a one-dimensional rectangular window applied in the range dimension divided by the window size. Using a one-dimensional window size of 128 samples is more meaningful in this context since the two-dimensional analysis windows (128×128 or 256×128) have the same range size. Figure 3.1e shows the averaged shadowing percentage for 150 simulated radar image sets. Clearly, the shadowing increases with range. This should not be surprising since the probability that a smaller wave is hidden by a bigger one increases as the grazing angle decreases (i.e. increasing range). Another interesting observation is that the shadowing is minimum at cross-wave ($\theta = 0°$ and $180°$), up-wave ($\theta = 90°$) and down-wave ($\theta = -90°$) directions. The reason behind the behavior of the shadowing at the up-wave and down-wave directions is not clear to us and will be investigated in future work. The minimum shadowing at the cross-wave (*i.e.* parallel to the wave front) direction can be explained by the fact that, at this angle, radar signals travel in parallel with the ocean wave front rather than facing it, giving a smaller opportunity for the shadowing to occur.

Table 3.1: Numerical tests: simulation parameters.

Image set size	$512 \times 512 \times 32$ samples
Antenna rotational period	1.44 s
Antenna height	10 m
Sampling frequency	20 MHz
Water depth	200 m
Wind wave direction	90° from the true north
Surface current	0.5 m/s 90° from the true north
The mean period T_{01}	10 s
The significant wave height	3.5 m

In order to investigate the effect of tilt modulation, it is calculated at near, mid and far ranges as a function of θ in a manner similar to that for the shadowing case. However, tilt modulation is quantified by integrating the tilt modulation signal over the range within a 128 sample one-dimensional rectangular window. Figure 3.1f shows the normalized averaged tilt modulation for the simulated image sets. The figure shows peaks at up-wave ($\theta = 90^\circ$) and down-wave ($\theta = -90^\circ$) directions and minima at cross-wave ($\theta = 0^\circ$ and 180°) for all ranges. This analysis strongly indicates that the azimuthal direction biases the radar imaging mechanisms and by extension wave spectral estimation. Also, it can be concluded that for best results in wave spectrum estimation, the analysis window should be chosen in the up-wave direction where the shadowing is minimum since higher shadowing induces higher order dispersion modes [12]. Also, the radar return is strongest in the up-wave direction due to the high tilt modulation factor and Bragg scattering.

To amplify this point, here we present a field data example. Figure 3.2 shows the ground truth directional wave spectrum for the field data example given in Figure 3.3.

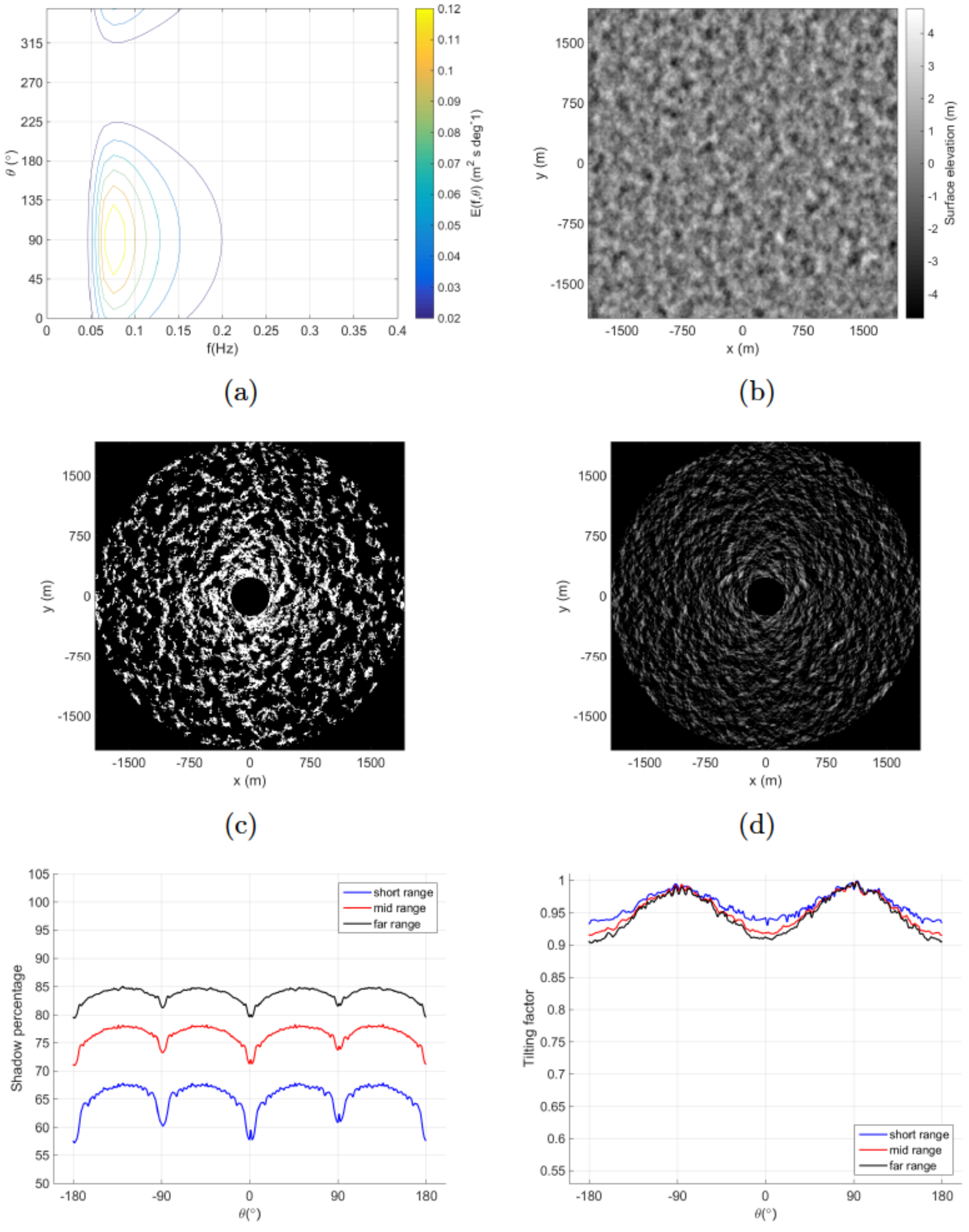

(a) (b) (c) (d) (e) (f)

Figure 3.1: Simulation analysis for shadowing and tilt modulation: **(a)** Directional wave spectrum used to generate simulated radar images; **(b)** Simulated surface elevation; **(c)** Shadowing mask; **(d)** Tilt modulation mask; **(e)** Shadowing percentage dependency on the azimuthal direction; **(f)** Tilt modulation factor dependency on the azimuthal direction.

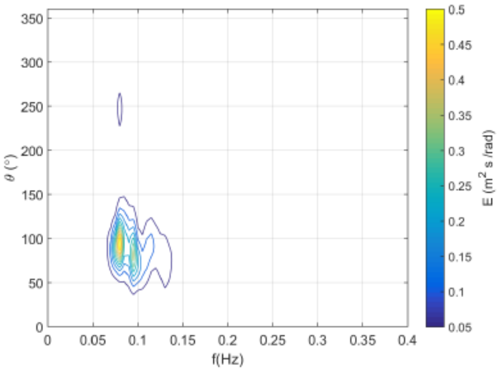

Figure 3.2: Directional wave spectrum for example given in Figure 3.3. Directional wave spectrum is estimated using a directional TRIAXYS wave rider buoy.

In this example, the directional and frequency wave spectra were estimated using the CFT from an analysis window that was positioned first in the up-wave direction (see Figures 3.3a and 3.3b) and second in the down-wave direction (see Figures 3.3c and 3.3d). It can be seen, when compared to the ground truth frequency wave spectra in Figures 3.3b and 3.3d, that the estimate of the frequency wave spectrum is more accurate when the analysis window is positioned in the up-wave direction (Figure 3.3b) compared to the down-wave direction (Figure 3.3d).

Wave spectra usually have one or two peaks that are related to wind waves or/and swell. The dominant wind wave and swell do not necessarily travel in the same direction. Therefore, choosing the analysis window in the wind wave direction might occur at the price of compromising the swell peak or vice versa. Traditionally, this problem is addressed by averaging the output of three uniformly distributed analysis windows. For a field data example, Figure 3.4 shows a directional wave spectrum which is calculated using wave rider buoy data and has two peaks at $\theta = 110°$ and 185°. The directional wave spectrum estimated using marine radar data with three analysis windows (see Figure 3.5a) is presented in Figure 3.5b. The directional wave spectrum from each window is acquired using the CFT-based method outlined in Section 2.3.2 and detailed in [10, 29, 47]. In the radar data used in this example,

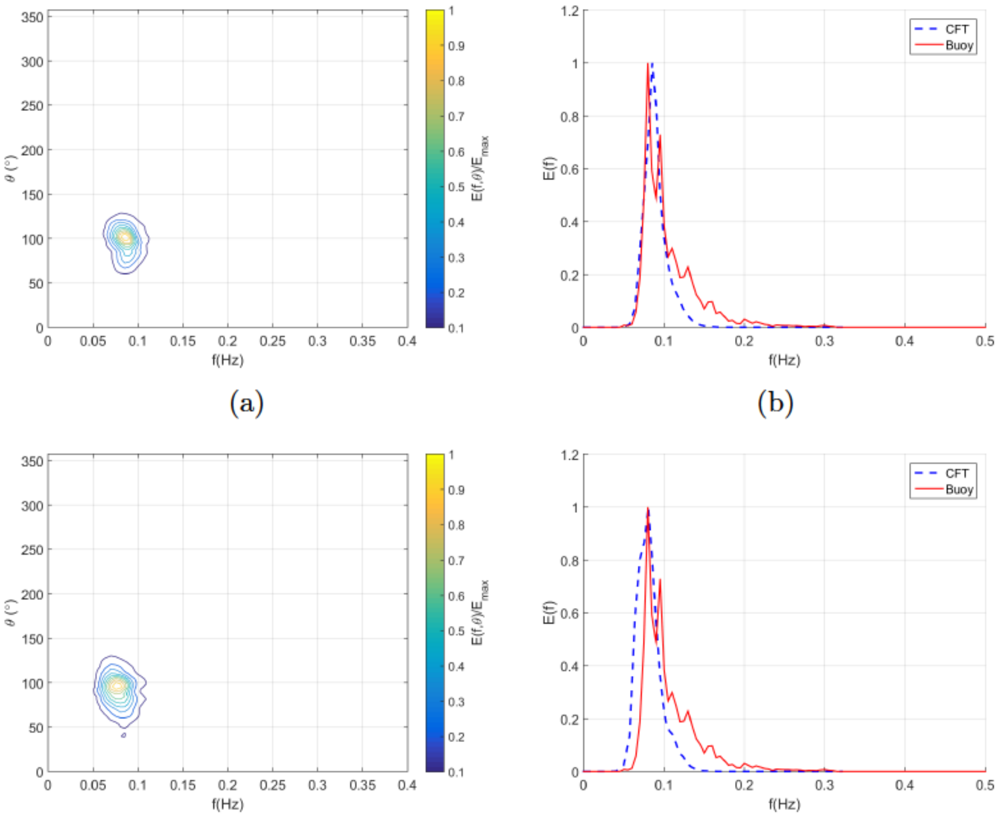

(a) (b)

(c) (d)

Figure 3.3: A field data example for wave spectrum estimation dependency on azimuth direction. Data was recorded on 27 Nov 2008 between 4:58 AM and 5:28 AM : (**a**,**c**) The directional wave spectrum estimated using the CFT on an analysis window positioned in the up-wave and down-wave directions, respectively; (**b**,**d**) The directional wave spectrum estimated using the CFT on an analysis window positioned in the up-wave and down-wave directions, respectively, overlaid on the ground truth frequency wave spectrum.

the buoy is located within the radar coverage. Clearly, both peaks in the directional wave spectrum of the buoy are detected in the radar's wave spectrum. However, comparing the normalized non-directional wave spectrum in Figure 3.5c, which is calculated using Equation 2.3.2 and divided by its maximum value, it may be seen that the second peak is almost non-distinguishable. However, when taking the analysis window orientation to be in the first peak direction, $\theta = 110°$ (see Figure 3.5d), the first peak is even more highly emphasized compared to the second one which is completely non-distinguishable as shown in Figures 3.5e and 3.5f. When taking the analysis window in the direction of the second peak ($\theta = 185°$), Figures 3.5g–3.5i show more weight for the second peak over the first which now has an energy level of 25% compared to 100% of the first peak for the ground truth. Finally, an intuitive solution is to average the results from the two analysis windows which are in the direction of spectral peaks at $\theta = 110°$ and 185° (see Figure 3.5j). Figures 3.5k and 3.5l show better agreement with the buoy estimated spectrum.

However, this approach is challenging since the wave directions are not known beforehand. In this chapter, a new method is proposed that is referred to as the Adaptive Recursive Positioning Method (ARPM); this method estimates the direction of travel of the waves and chooses the analysis windows orientation accordingly.

3.3 The Adaptive Recursive Positioning Method (ARPM)

The ARPM determines the number and orientation of the analysis windows according to the number and orientation of peaks in the wave spectrum. In the case where the wave spectrum has only one peak, one analysis window is chosen in the direction of that peak. In the case where the wave spectrum consists of two peaks resulting

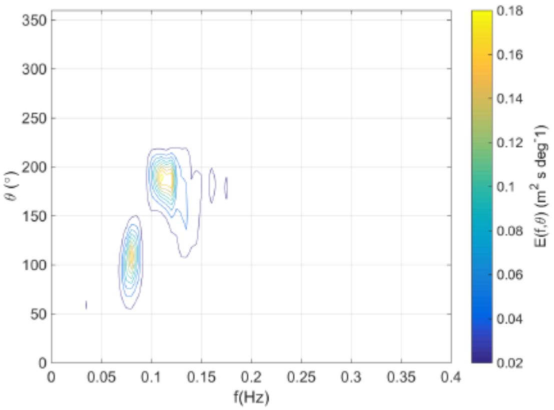

Figure 3.4: Directional wave spectrum for example given in Figure 3.5. Directional wave spectrum is estimated using a directional TRIAXYS wave rider buoy.

from wind waves and swell, two analysis windows are chosen in the directions of these peaks. For instances where the wave spectrum may consist of $n > 2$ peaks, n (possibly overlapped) analysis windows are used and positioned in the peak directions. Since the wave spectrum is not known beforehand, the ARPM determines the analysis window locations recursively. Figure 3.6 shows the flowchart of the ARPM. The method starts by estimating the wave spectrum using three uniformly distributed analysis windows in a manner that is similar to the standard method outlined in Section 3.2. The estimated directional wave spectrum is used as an initial estimate to determine the number and direction of the peaks. Subsequently, new analysis window(s) are chosen in the direction(s) of the peaks, and a new estimate of the wave spectrum is obtained. This process is repeated until a termination criterion is satisfied. For the results of this chapter, a simple termination criterion is used which limits the number of iterations to a maximum number. Based on the field data used, three iterations were found to generate satisfactory results after which little change in the number and orientation of the analysis windows was noticed. While Figure 3.7, which is acquired using the field data described in Section 2.4, shows a continuous decrease in the average change in the orientation of the analysis windows to iteration

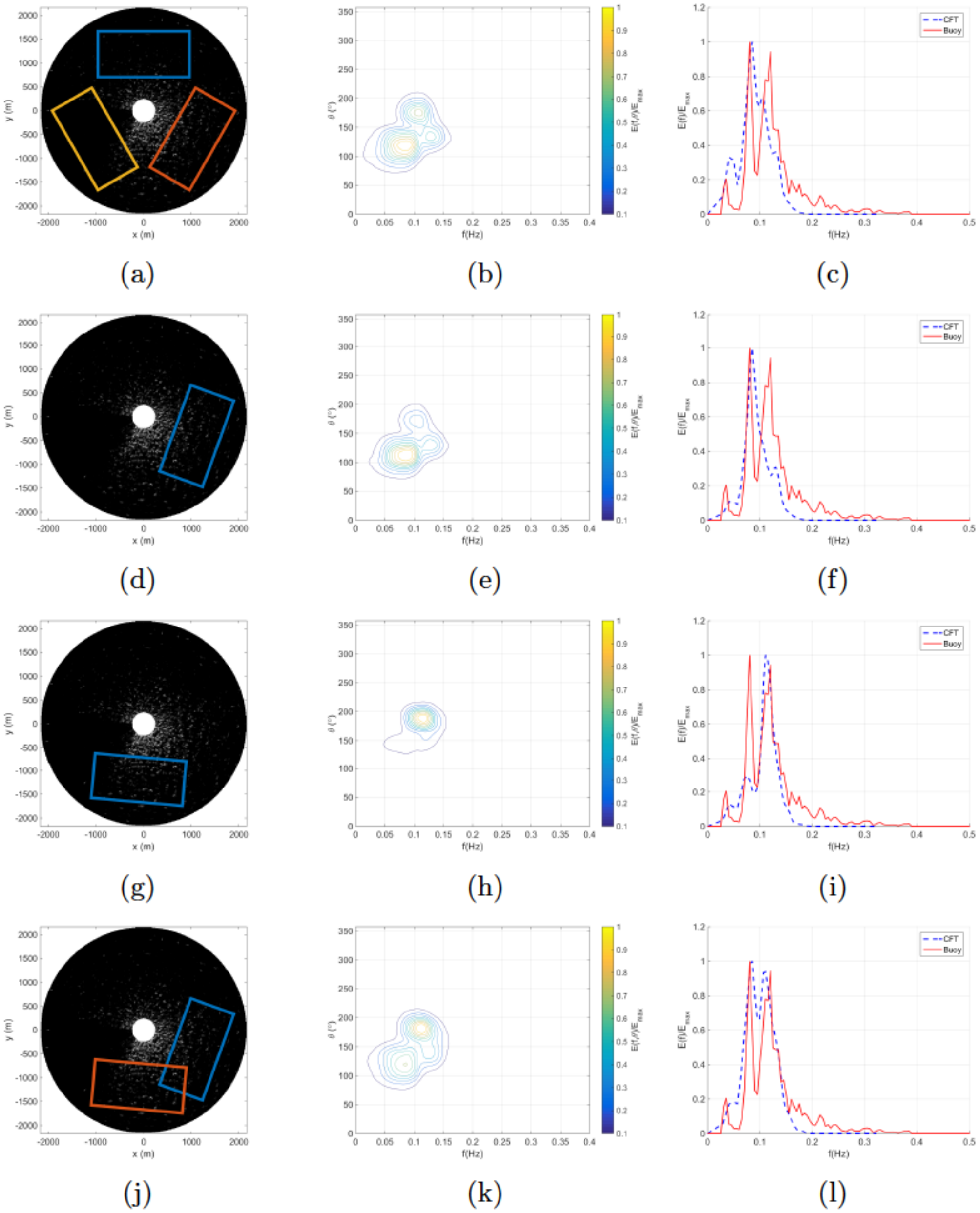

(a) (b) (c)

(d) (e) (f)

(g) (h) (i)

(j) (k) (l)

Figure 3.5: A field data example for wave spectrum estimation dependency on azimuth direction. Data was recorded on 1 December 2008 between 4:03 PM and 4:38 PM : (**a,d,g,j**) A single Furuno radar image shown with various analysis window orientations; (**b,e,h,k**) The directional wave spectrum estimated using the CFT on the analysis windows in Figures b, e, h and k, respectively; (**c,f,i,l**) The frequency wave spectrum estimated using the CFT on the analysis windows in Figures a, d, g and j, respectively overlaid on the ground truth frequency wave spectrum.

5 or 6, trading off analysis cost and estimate accuracy, 3 iterations were found to be sufficient.

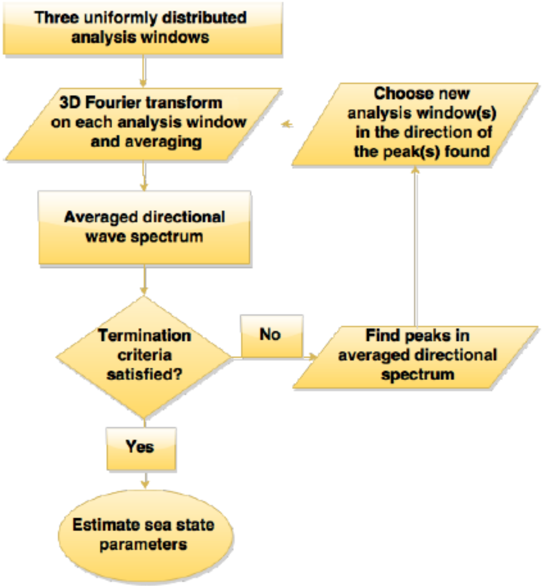

Figure 3.6: Adaptive Recursive Positioning Method (ARPM) flowchart.

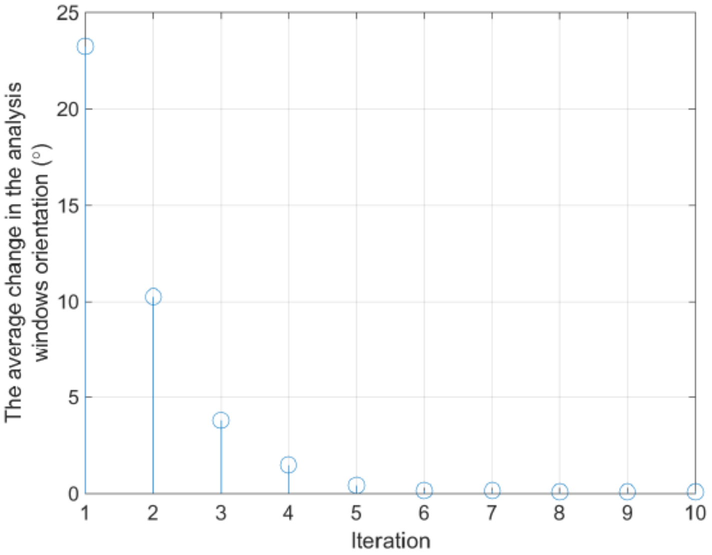

Figure 3.7: The average change in the analysis windows' orientation from one iteration to the next for different number of iterations in the ARPM.

Obviously this method needs a full field of view, or in practice, close to it. This is needed to facilitate the freedom in choosing the orientation of the analysis window(s). Usually, data from offshore platforms and shipboard marine radars provide such a field of view. On the other hand, coastal station marine radars might not provide such a wide ocean field of view. However, the ARPM method may still be applied, although in a more limited and less effective way since the up-wave direction detected in the initial guess of directional wave spectrum may not be part of the field of view.

3.4 Results and Analysis

3.4.1 Field Data Examples

In order to demonstrate the accuracy of the ARPM, we start by an example. Figure 3.8 shows a ground truth wave spectrum which is estimated from TRIAXYS wave buoy data. The spectrum has a main peak at 0.075 Hz and 90° and a secondary peak at 0.15 Hz and 150°. Figure 3.9 shows the ARPM output for each iteration. The estimated directional and frequency wave spectrum in the first iteration (standard method) is shown in Figures 3.9a and 3.9b, respectively. The secondary peak is underestimated with a lower relative energy level of 25%, relative to that of the main peak of the first iteration, compared to 40% for the ground truth secondary peak. In the second iteration, only two analysis windows are used, and they are repositioned to be in the peak directions. The estimated directional and frequency wave spectra of the second iteration are shown in Figures 3.9c and 3.9d, respectively. Clearly, the secondary peak is better estimated in this iteration with a higher relative energy level of 60%, relative to that of the main peak of the second iteration, compared to its estimate in the first iteration of 25%. However, further refinement is needed since it now has more relative energy than the ground truth and thus can be deemed to be

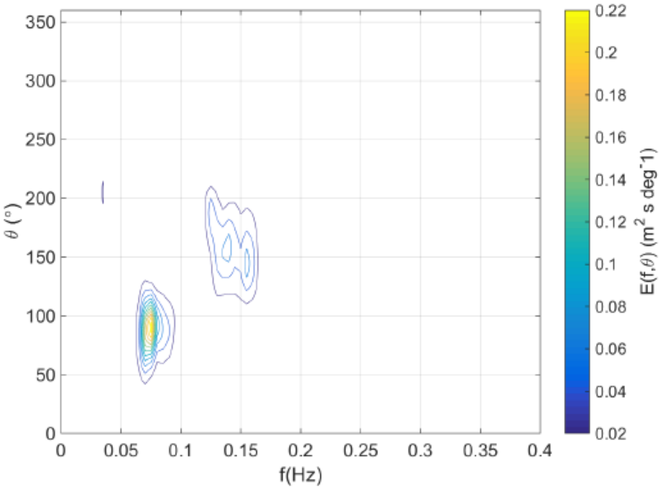

Figure 3.8: Directional wave spectrum for example given in Figure 3.9. Directional wave spectrum is estimated using a directional TRIAXYS wave rider buoy.

over-estimated. Finally, the last iteration produces a satisfactory improvement in the estimated wave spectra as shown in Figures 3.9e and 3.9f. The secondary peak is now almost at the same relative energy level (40%) as in the ground truth spectrum.

Another example is shown in Figures 3.10 and 3.11. Figure 3.10 shows a ground truth wave spectrum which is estimated using a TRIAXYS wave buoy data. The spectrum has two peaks, a main peak at 0.09 Hz and 225° and a secondary peak at 0.09 Hz and 75°. Obviously, these peaks are not distinguished through the frequency spectrum because both peaks are at 0.09 Hz. Looking at the directional wave spectrum in Figure 3.11a produced in the first iteration, the secondary peak is not detected. Comparing this estimate to the final estimate produced in the final iteration (Figure 3.11e), the secondary peak is now visible.

3.4.2 Performance Validation

The last two examples show that the ARPM significantly improves the wave spectrum estimation over the standard method. In order to validate the performance of the ARPM, the agreement between its estimated wave spectrum and the buoy wave

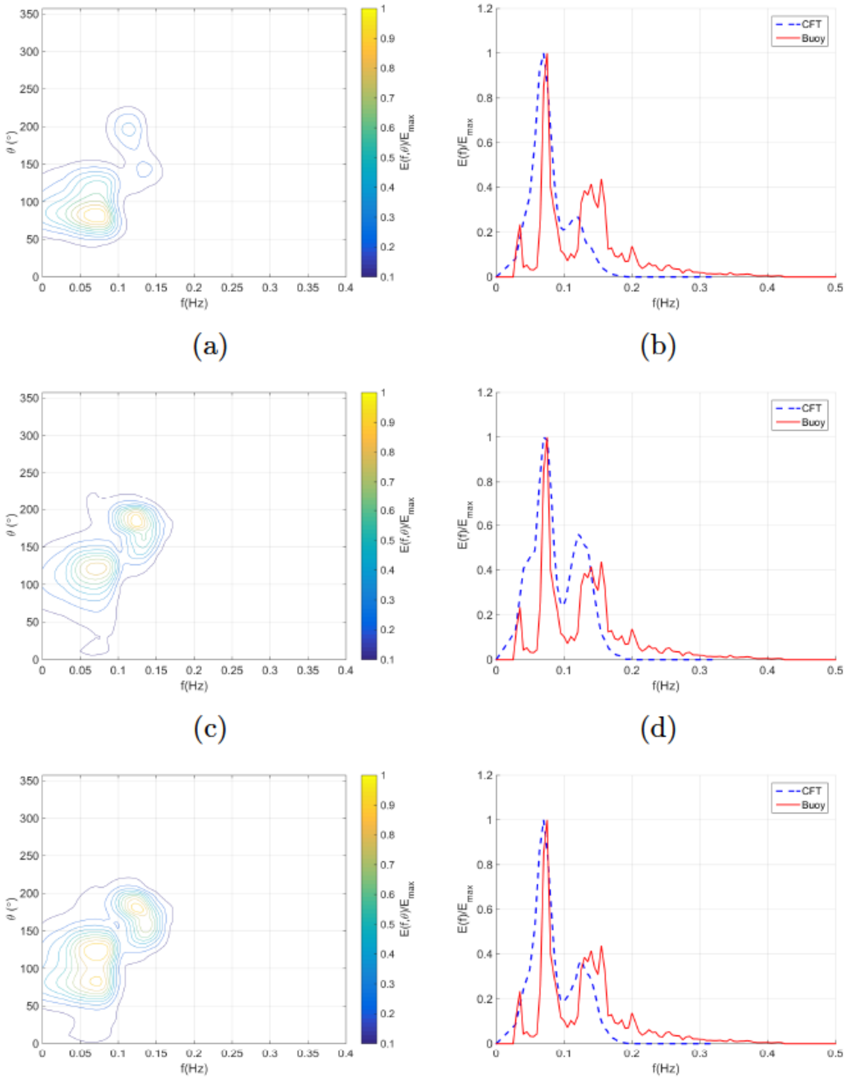

(a) (b) (c) (d) (e) (f)

Figure 3.9: A field data example for wave spectrum estimation using the CFT with the ARPM. Data was recorded on 1 December 2008 between 11:48 AM and 12:08 PM: (**a**,**c**,**e**) The directional wave spectrum estimated in the first, second and third iteration, respectively; (**b**,**d**,**f**) The frequency wave spectrum estimated from the radar data in the first, second and third iteration respectively and overlaid on the ground truth frequency wave spectrum.

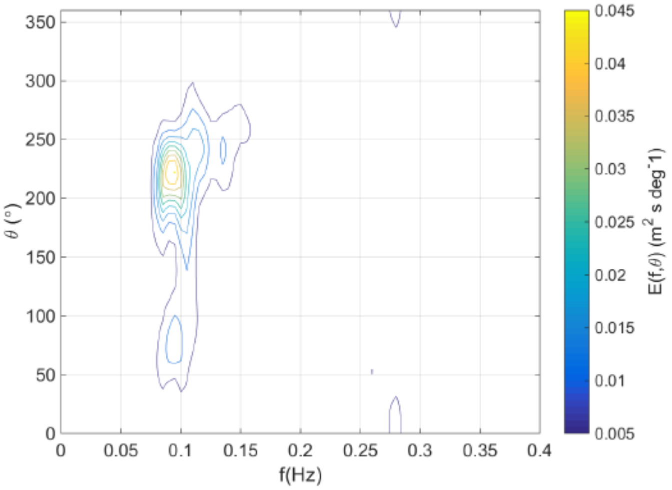

Figure 3.10: Directional wave spectrum for example given in Figure 3.11. Directional wave spectrum is estimated using a directional TRIAXYS wave rider buoy.

spectrum (the ground truth) is quantified using the correlation coefficient between the two frequency spectra on a discrete frequency grid. The value of the correlation coefficient ranges from 0 (no similarity) to 1 (identical) and is estimated by

$$\rho = \frac{N_f \sum E_R E_B - (\sum E_R)(\sum E_B)}{\sqrt{[N_f \sum E_R^2 - (\sum E_R)^2][N_f \sum E_B^2 - (\sum E_B)^2]}}, \tag{3.1}$$

where E_R and E_B are the radar and buoy-estimated normalized frequency spectrum, respectively, N_f is the number of frequency points in E_R and E_B, and $\sum$ is the summation over all frequency points in E_R and E_B. As described in Section 2.4, one radar set (32 images) is used to calculate a wave spectrum estimate. Furthermore, the buoy records data for 30 minutes in order to generate an estimate of wave spectrum. For a proper comparison with the wave buoy output, a buoy wave spectrum estimate was compared to the average of all radar-based wave spectral estimates that were produced within the 30-minute interval of that buoy estimate. The standard method and the ARPM are used to estimate the wave spectrum. The estimated correlation coefficient with the buoy ground truth is calculated for each method. Figure 3.12

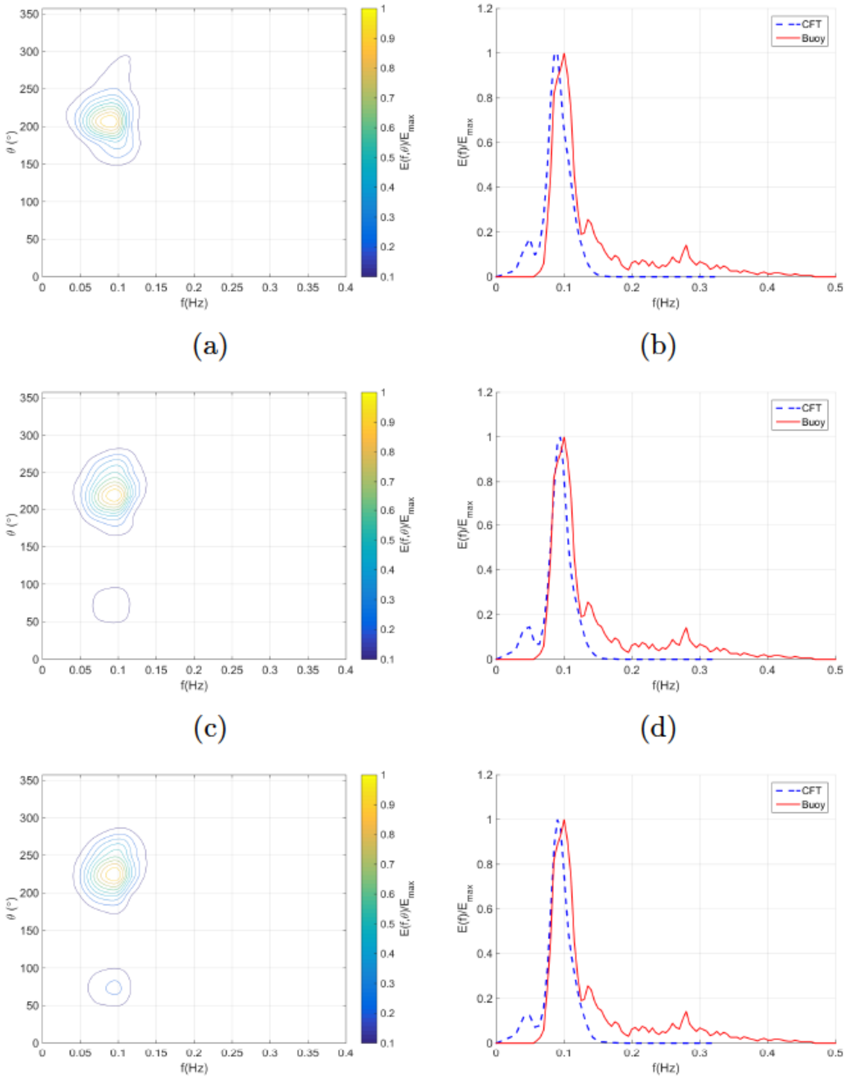

(a) (b)

(c) (d)

(e) (f)

Figure 3.11: A field data example for wave spectrum estimation using the CFT with the ARPM. Data was recorded on 3 December 2008 between 5:01 AM and 5:31 AM: (**a**,**c**,**e**) The directional wave spectrum estimated in the first, second and third iteration, respectively; (**b**,**d**,**f**) The frequency wave spectrum estimated from the radar data in the first, second and third iteration respectively and overlaid on the ground truth frequency wave spectrum.

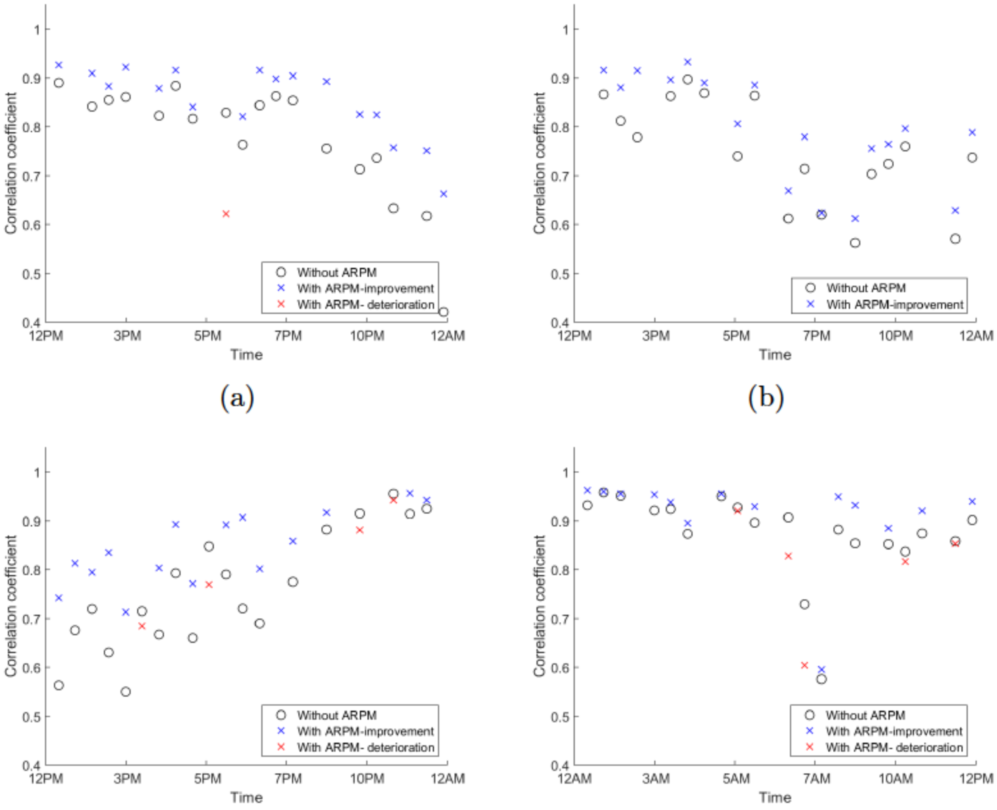

(a) (b)

(c) (d)

Figure 3.12: A comparison between the ARPM and the standard method in terms of the frequency wave spectrum similarity with respect to the buoy ground truth spectra. Each point represents the correlation coefficient between ground truth and the radar-estimated frequency wave spectra.(a) Dec 1 afternoon and evening, (b) Dec 2 afternoon and evening, (c) Dec 3 afternoon and evening, (d) Dec 4 morning.

shows the correlation coefficient in pairs: the standard method coefficient is marked using an “o” while the ARPM is marked using an “ × ”; the results are shown for four 12-hour periods during Dec 1 - Dec 4, 2008. To enhance the readability of the results, the ARPM output is plotted in blue (red) to indicate improvement (deterioration) in performance compared to the standard method. Clearly, the ARPM outperforms the standard method with higher correlation coefficients except for a few cases. The average improvement is found to be 9.8%.

For further validation, the peak wave period T_p, mean period T_{01}, the zero-crossing period T_z and the peak wave direction θ_p are estimated for wind waves and swell using the standard method and the ARPM. Figures 3.13 and 3.14 show the peak wave period and direction, respectively, over time. Both figures show an advantage of the ARPM over the standard CFT method for most of the time. The mean absolute error ($\overline{|\varepsilon_{T_p}|}$,$\overline{|\varepsilon_{T_{01}}|}$, $\overline{|\varepsilon_{T_z}|}$ and $\overline{|\varepsilon_{\theta_p}|}$) and error standard deviation ($\sigma_{\varepsilon_{T_p}}$, $\sigma_{\varepsilon_{T_{01}}}$, $\sigma_{\varepsilon_{T_z}}$ and $\sigma_{\varepsilon_{\theta_p}}$) of these estimates are calculated with respect to the ground truth and listed in Table 3.2. Figure 3.15 shows the normalized (with respect to the CFT) average absolute error in estimating T_p, T_{01}, T_z, and θ_p using the ARPM. The mean absolute error and the error standard deviation of T_p are calculated by

$$\overline{|\varepsilon_{T_p}|} = \frac{1}{N_e} \sum_{n=1}^{N_e} |T_{p_n} - T_{pBuoy_n}| \tag{3.2}$$

and

$$\sigma_{\varepsilon_{T_p}} = \sqrt{\frac{1}{N_e} \sum_{n=1}^{N_e} \left(T_{p_n} - \frac{1}{N_e} \sum_{m=1}^{N_e}, T_{p_m} \right)^2}, \tag{3.3}$$

respectively, where N_e is the total number of radar estimates and T_{pBuoy} is the buoy ground truth of T_p. The other metrics in Table 3.2 are calculated in a similar manner.

Finally, it is not surprising that this improvement comes at the price of extra computational time. As an illustration, in our analysis and implementation, the standard method needed 2.7 s to process one radar set (32 radar images) while the ARPM required 5 s, with both implementations running on the same processor and with similar software and data structure efficiency. However, this price is very reasonable since the time needed by the radar to generate one data set is 48 s. Therefore, the ARPM can be also used for real-time analysis.

In the next chapter, the effect of the ocean surface sampling process on the estimated ocean wave spectra is investigated. It will be demonstrated that the conventional assumption of the radar sampling process of the ocean surface being a standard sampling is not quite accurate. In fact, an averaging process is involved and can be

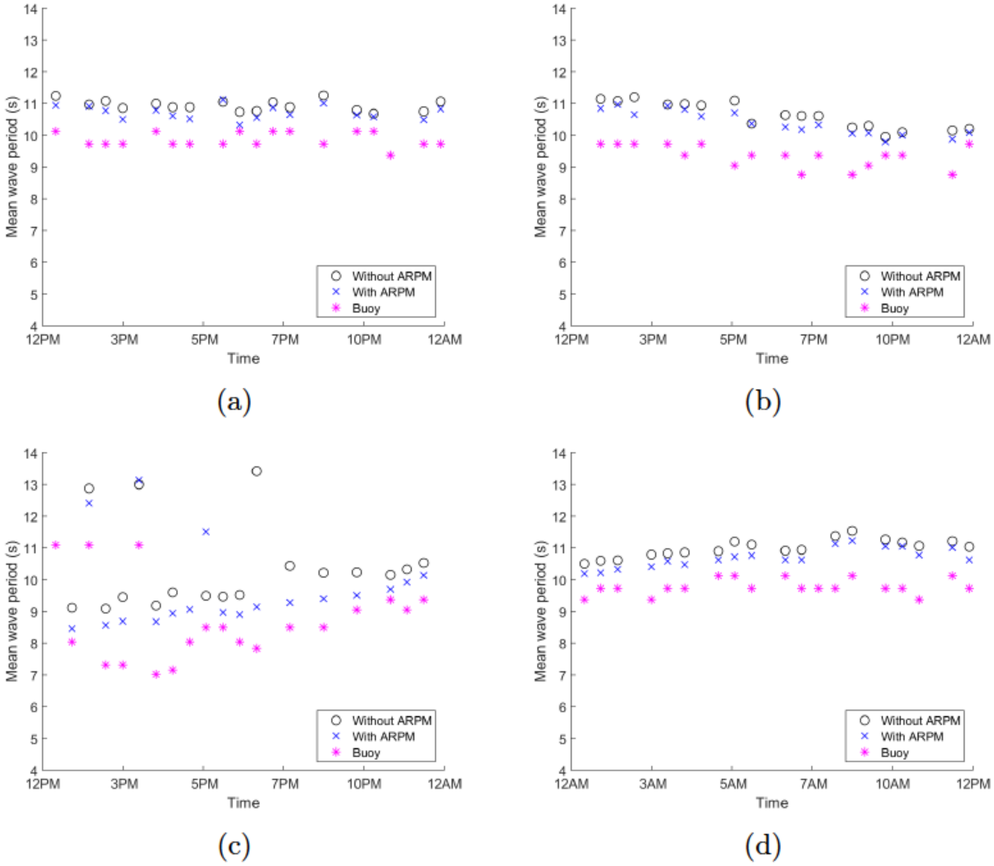

(a) (b) (c) (d)

Figure 3.13: A comparison between the ARPM and the standard method in terms of the peak wave period. (a) Dec 1 afternoon and evening, (b) Dec 2 afternoon and evening, (c) Dec 3 afternoon and evening, (d) Dec 4 morning.

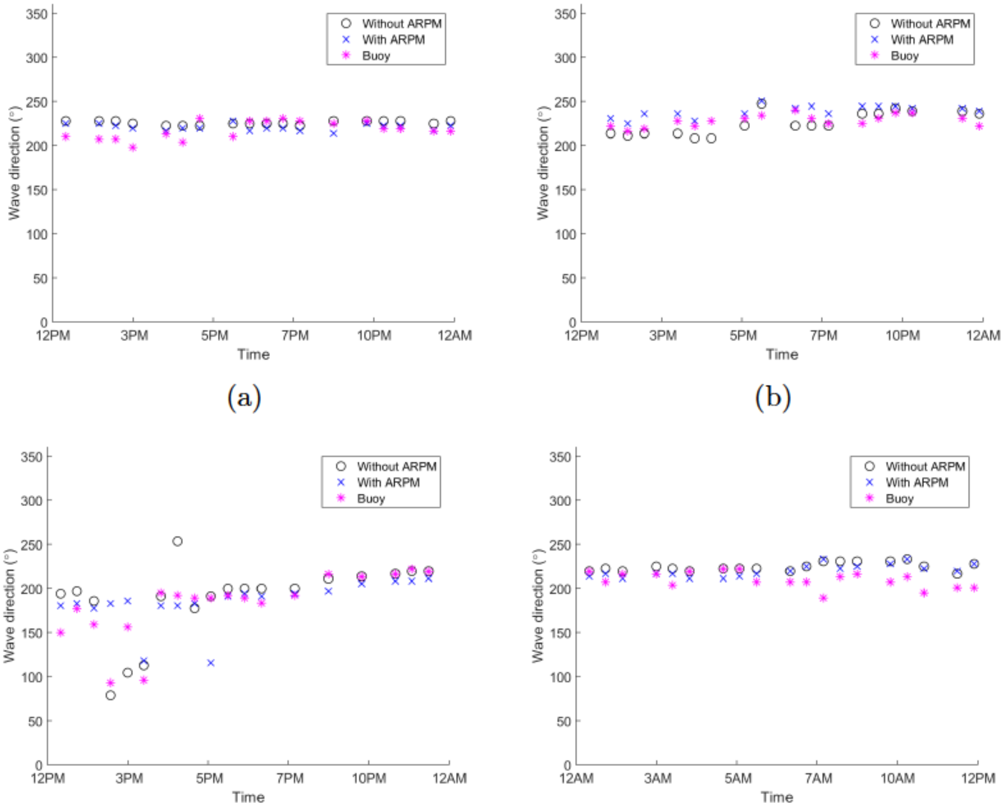

(a) (b)

(c) (d)

Figure 3.14: A comparison between the ARPM and the standard method in terms of the peak wave direction. (a) Dec 1 afternoon and evening, (b) Dec 3 morning, (c) Dec 2 afternoon and evening, (d) Dec 3 morning.

represented by an analytical model. Understanding the sampling process will help us to understand its effect on ocean wave spectra estimation and, ultimately, in the design of an algorithm to mitigate that effect.

Table 3.2: Comparison of the ARPM and the standard method in wave period and peak direction estimation.

	$\overline{\lvert\varepsilon_{T_p}\rvert}$(s)	$\boldsymbol{\sigma}_{\varepsilon_{T_p}}$ (s)	$\overline{\lvert\varepsilon_{T_{01}}\rvert}$(s)	$\boldsymbol{\sigma}_{\varepsilon_{T_{01}}}$ (s)	$\overline{\lvert\varepsilon_{T_z}\rvert}$(s)	$\boldsymbol{\sigma}_{\varepsilon_{T_z}}$(s)	$\overline{\lvert\varepsilon_{\theta_p}\rvert}$(°)	$\boldsymbol{\sigma}_{\varepsilon_{\theta_p}}$(°)
CFT	2.5	0.9	2.4	0.8	2.3	0.8	15.1	16.1
ARPM	2	0.9	1.9	1.5	1.9	1.5	11.7	13

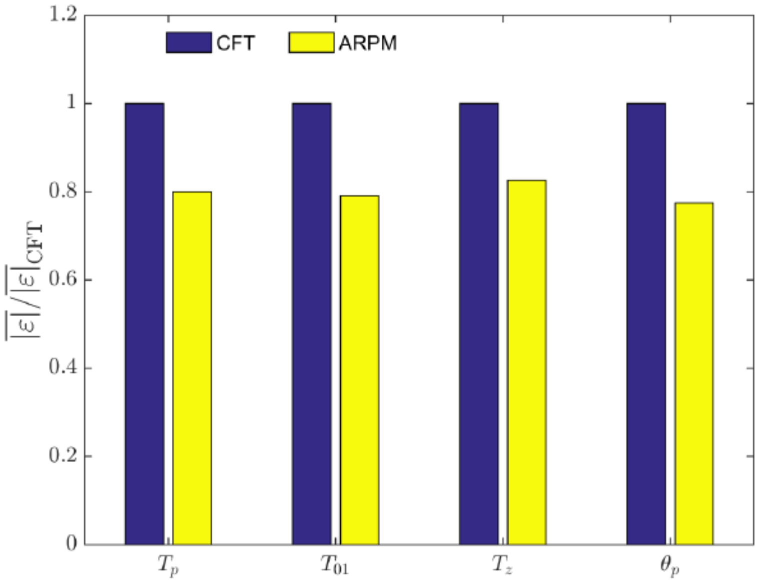

Figure 3.15: The average absolute error of the ARPM normalized with respect to the CFT method.

3.5 Conclusions

In this chapter, the dependency of ocean wave spectra estimation on the orientation of the analysis windows is investigated. Our results show that the best orientation of the analysis window is in the up-wave direction where the effects of shadowing and tilt modulation are minimum and the returned scatter intensity is maximum due to stronger Bragg scattering. However, in the presence of wind waves and swell, the situation is more challenging since choosing the orientation of the analysis window in the direction of one of the sets of waves (wind waves or swell) is at the price of underestimating the other one. For this reason, we propose to use multiple analysis windows oriented in the directions of wind waves and swell. This approach presents another challenge which is that the wind wave and/or the swell directions are not known *a priori*. Therefore, this chapter proposes the Adaptive Recursive Position Method (ARPM) to solve this problem by finding the number and orientation of analysis windows recursively. The ARPM presented significant improvement in wave spectra estimation that has been demonstrated by producing frequency spectra that better agree with ground truth data. It has also been shown that the ARPM can produce more accurate and reliable wave period and direction estimates compared to the standard method. The ARPM successfully serves the purpose of reducing the estimation error of the ocean wave spectra using the CFT method. Future work on the ARPM will include possible enhancements of the iterative process by seeking optimal initial guesses and termination criteria.

Chapter 4

The effect of radar ocean surface sampling on wave spectrum estimation using X-band marine radar

4.1 Introduction

The dependency of estimated ocean wave spectra on the azimuth direction of analysis window was the first source of error in wave spectra estimation addressed in this thesis. The second source of error in ocean wave spectral estimation addressed in this thesis is from the sampling process of the ocean surface by X-band marine radars. This problem has not been previously addressed. Our approach is to model the effect of the ocean sampling process via an invertible analog filter. Subsequently, the effect of the sampling process may be mitigated by using the inverse of the proposed analog filter.

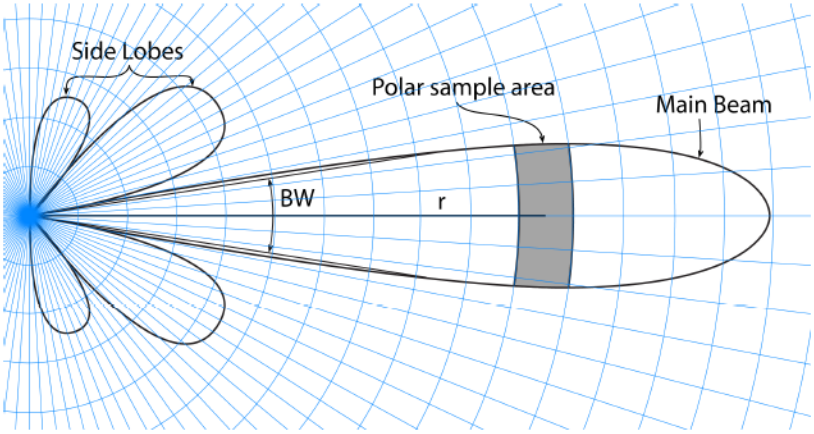

Figure 4.1: An illustration of radar radiation pattern.

4.2 The Radar Sampling Process and the Inverse Sampling Averaging Filter (ISAF)

4.2.1 Radar sampling process

To sample the ocean surface over the range dimension at a given direction using an X-band marine radar, the radar sends its electromagnetic pulse with the main beam being pointed in that direction as shown in Figure 4.1. Subsequently, the radar starts to receive the returned scatter, repeatedly, for short periods of time $\tau = 1/f_s$, where f_s is the radar sampling frequency. The radar range resolution Δ_r is determined by τ via [1, 51]

$$\Delta_r = c\tau/2, \tag{4.1}$$

where c is the speed of light. The azimuth radar resolution is given by

$$\Delta_\theta = BWr,$$

where BW is the half-power beam width and r is the distance of the sample from the radar. The returned scatter from the sample is collected from the entire area of the sample. This implies that an averaging filter is involved in the sampling process. The manner in which different locations in the sample patch contribute to the returned signal is difficult to model or estimate due to the following reasons. First, various locations in the sample patch depend on the ocean state at the time of scatter. Second, the signal power across the sample patch varies due to the radar beam pattern. However, to simplify the problem we assume that different parts in the sample area contribute equally to the returned scatter.

Our preliminary approach to investigate the effect of the ocean surface sampling process on the estimates of the ocean wave spectra is as follows. First, Cartesian images of ocean surface elevation are simulated on a fine grid. For best results, a high Cartesian spatial resolution of $dx \times dy = 1 \times 1$ m is used. Next, B-scan images are generated from the simulated ocean surface elevation Cartesian images using values of Δ_r and BW that are used in an actual X-band marine radar as listed in Table 4.1. A B-scan sample is calculated by averaging those high-resolution Cartesian samples which fall in the area of that B-scan sample. Finally, the CFT method is used to estimate the ocean wave spectra from the B-scan images. In order to understand the behavior of the ocean surface sampling process, the CFT-estimates are compared to the simulation input spectra (the spectra used to generate the simulated Cartesian images of ocean surface elevation). It should be noted here that neither shadowing nor tilt modulation were implemented in our simulation in order to examine the effect of the ocean surface sampling alone. A modified Pierson-Moskowitz-based power distribution model presented in [66] was adopted to generate the input non-directional wave spectrum of the simulation. A squared cosine distribution[11] was used to add the directional component of the input directional wave spectrum for producing the simulated images. Furthermore, for more realistic simulation output, uniform random phases were added to different wave numbers of the input wave spectrum.

Figure 4.2a shows an example of the generated simulation input directional wave spectrum based on the parameters listed in Table 4.1. Figure 4.2b depicts a sample of the simulated high resolution ocean surface elevation images. Figure 4.2c shows the B-scan image generated from the high resolution ocean surface image displayed in Figure 4.2b. Figure 4.2d shows an analysis window of size 1600×800 m generated from the B-scan image displayed in Figure 4.2c using the scan conversion process outlined in Section 2.3.1. Figure 4.2e contains the CFT-estimate of the directional wave spectrum from the analysis window with a sample shown in Figure 4.2d. Also, Figure 4.2f displays the normalized CFT-estimate of the non-directional wave spectrum compared to the simulated normalized input non-directional wave spectrum. Clearly, the normalized CFT-estimate of the non-directional wave spectrum decays faster than the normalized input spectrum. This supports our assumption that the sampling process may be presented by an averaging (low pass) filter that attenuates high frequencies relative to low frequencies.

Table 4.1: Numerical tests: simulation parameters.

Antenna rotational period	1.44 s
Ocean surface grid resolution	1×1 m
Wind wave direction	90° from true north
Mean period T_{01}	10 s
Significant wave height	3.5 m
Antenna beam width BW	1°
Pulses per 360°	1000
Radar sampling frequency f_s	20 MHz
Radar range resolution Δ_r	7.5 m

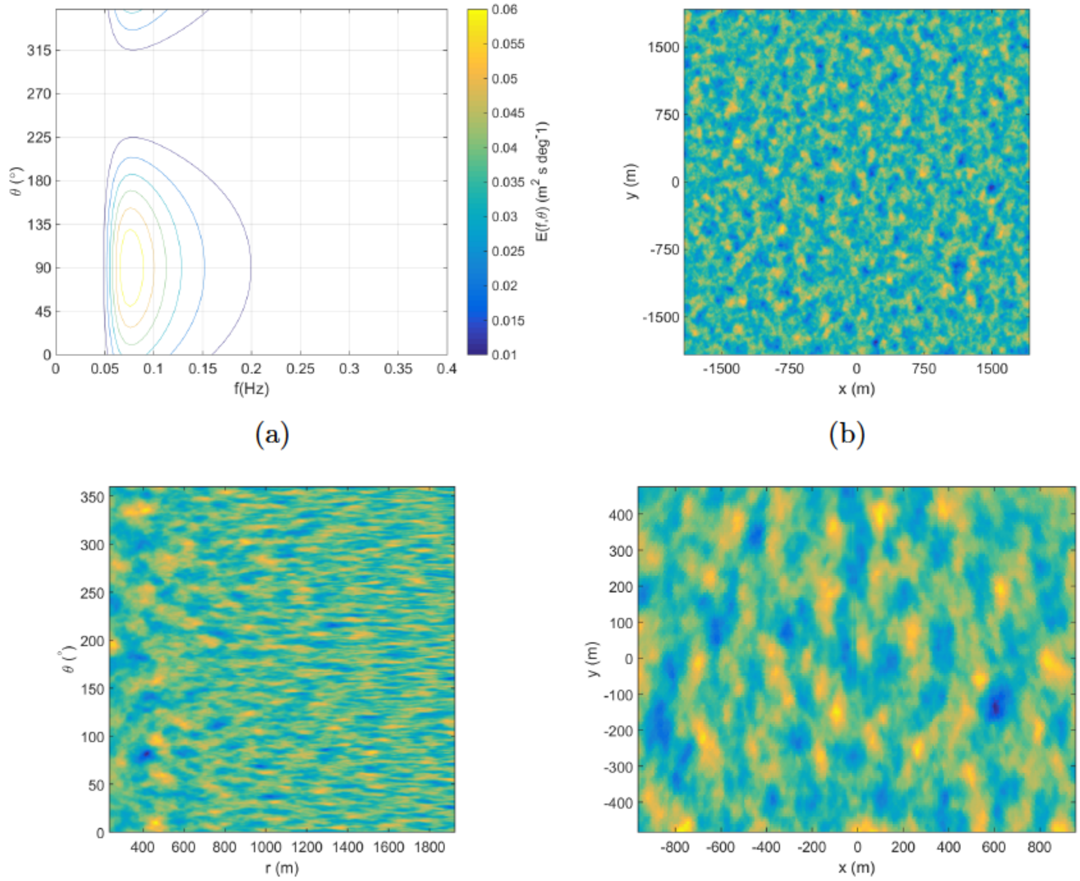

(a) (b)

(c) (d)

Figure 4.2: A synthetic data example that illustrates the effect of the radar sampling process of the ocean surface on estimates of ocean wave spectra. (a) Simulation input directional wave spectrum. (b) A sample of the simulated high resolution Cartesian images of ocean surface elevation using $dx \times dy = 1 \times 1$ m. (c) A sample of the B-scan images that are produced from the simulated high resolution images using $\Delta_r = 7.5$ m and $\Delta_\theta = 1^\circ$. (d) A selected rectangular analysis window from the scan converted B-scan images of size 1600×800 m using $\Delta_x \times \Delta_y = 7.5 \times 7.5$ m.

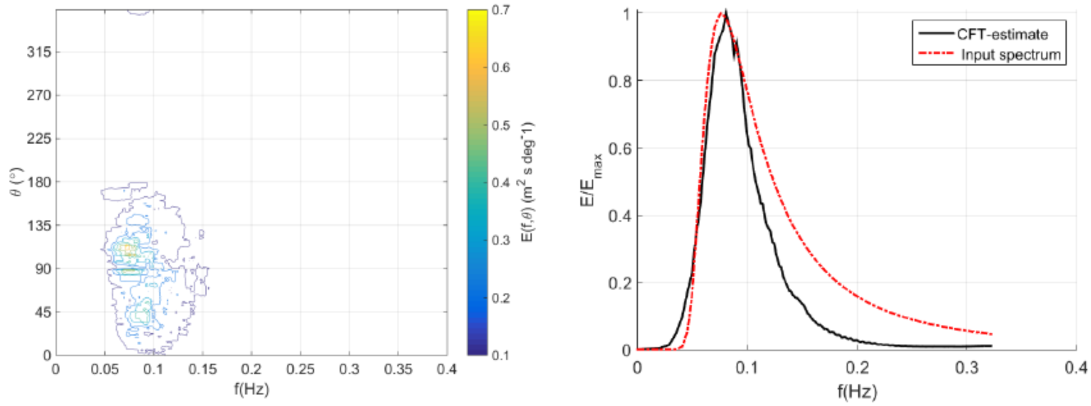

(e) (f)

Figure 4.2: (e) The normalized estimated directional wave spectrum using the CFT method from B-scan simulated radar returns of the ocean surface elevation. (f) The normalized input and CFT-estimate of the non-directional wave spectra.

In order to understand the effect of ocean surface sampling on the estimated ocean wave spectra from the simulated data, Figure 4.3 shows an area of a B-scan sample which is a function of the range resolution Δ_r, the beamwidth BW and the range r. The figure also shows the underlying high-resolution Cartesian grid for the simulated ocean surface elevation with a spatial resolution of $dx \times dy = 1 \times 1$ m. Clearly, the number of high-resolution samples that are averaged to form the B-scan sample is not fixed, but increases with range r and, by extension, with the area of the B-scan sample. To simplify the problem, the B-scan sample area is considered to be rectangular with the dimensions of $L_x \times L_y$, where $L_x = r\ BW$ and $L_y = \Delta_r$, instead of the ring sector, as shown in Figure 4.3. This assumption is valid for high ranges r and low Beam width BW values, which is the case in our field data experiment with $r > 240$ and $BW = 1°$. The numbers of high-resolution samples N_x and N_y that are averaged to produce one B-scan sample are given by

$$N_x = \left\lceil \frac{L_x}{dx} \right\rceil \text{ and } N_y = \left\lceil \frac{L_y}{dy} \right\rceil, \tag{4.2}$$

respectively, where $\lceil \cdot \rceil$ is the ceiling function. The wave number response of this averaging process can be given by the 2-D low pass filter $H_{\tilde{k}} = H_{\tilde{k}_x} H_{\tilde{k}_y}$ where

$$H_{\tilde{k}_x}(\tilde{k}_x) = \frac{1}{N_x} \sum_{n_x=-N_x/2}^{N_x/2-1} (r_z e^{j\tilde{k}_x})^{-n_x} \tag{4.3}$$

$$H_{\tilde{k}_y}(\tilde{k}_y) = \frac{1}{N_y} \sum_{n_y=-N_y/2}^{N_y/2-1} (r_z e^{j\tilde{k}_y})^{-n_y} \tag{4.4}$$

where $\tilde{k}_x = k_x dx$ and $\tilde{k}_y = k_y dy$ are the normalized wave number vector components in the x and y direction, respectively, and r_z is the magnitude of the filter zeros. In order to achieve an invertible filter, r_z was chosen to be 0.9 (see Section 4.2.3 for an explanation of this choice). Using the radar configurations given in Table 4.1 and Equations 4.1 and 4.2 and considering $r = 1000$ m, N_x and N_y are found to be 18 and 8, respectively. Figures 4.4a and 4.4b show the zero-pole diagrams of $H_{\tilde{k}_x}$ and $H_{\tilde{k}_y}$, respectively, while Figure 4.5a and Figure 4.5b shows the normalized directional magnitude response of $H_{\tilde{k}}$ in the $(\tilde{k}_x, \tilde{k}_y)$ and $(\tilde{k}, \theta)$ domain, respectively. To verify our rectangular area assumption, $H_{\tilde{k}}(\tilde{k}_x, \tilde{k}_y)$ is multiplied by the input directional wave spectrum shown in Figure 4.5 to produce a modified input non-directional wave spectrum. This modified spectrum is compared to the CFT-estimate of the non-directional wave wave spectrum as shown in Figure 4.6. Clearly, introducing $H_{\tilde{k}}$ improves the agreement between the two non-directional wave spectra. Since $H_{\tilde{k}}$ is designed to be invertible (see Section 4.2.3), the effect of the radar sampling process may be mitigated by multiplying the CFT-estimate of the directional wave spectrum by $H_{\tilde{k}}^{-1}$. Figure 4.7 shows the improvement that shaping by $H_{\tilde{k}}^{-1}$ can bring to the CFT-estimate of the non-directional wave spectrum. When multiplied by $H_{\tilde{k}}^{-1}$, the observed increase in the non-directional wave spectrum shown in Figure 4.7 for frequencies higher than 0.25 Hz is due to the small values of $H_{\tilde{k}}$ shown in Figure 4.5. This behavior at higher frequencies is not expected to be experienced in our field data

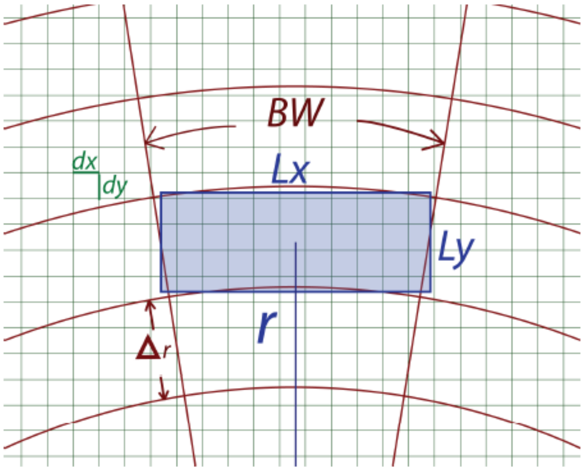

Figure 4.3: An illustration of the the polar samples area.

analysis as shown is Section 4.2.2.

The previous example and the design of $H_{\tilde{k}}$ have helped in understanding the effect of the ocean surface sampling process on the estimated ocean wave spectra. $H_{\tilde{k}}^{-1}$ was designed to mitigate the effect of the averaging process of the simulated ocean surface elevation with $dx \times dy = 1$ m on the estimated ocean wave spectra. Considering a higher resolution of the simulated ocean surface elevation lead to higher values of N_x and N_y given in Equation 4.2 and, hence, a more accurate design of $H_{\tilde{k}}$ in modeling the effect of ocean surface sampling process. Ultimately, the most accurate design of $H_{\tilde{k}}$ is achieved when $dx \times dy \to 0$, which requires consideration of the filter design in the analog domain.

4.2.2 The averaging process in the analog domain

In order to extend $H_{\tilde{k}}^{-1}$ to be applicable to radar field data, the filter design has to be considered in the analog domain. The radar actually collects the returned scatter from the continuous rectangular area $L_x \times L_y$ shown in Figure 4.3. Therefore, the analog average filter is given by $H_k = H_{k_x} H_{k_y}$ where H_{k_x} and H_{k_y} are adaptive moving average filters in the x and y directions, respectively, and are calculated as follows.

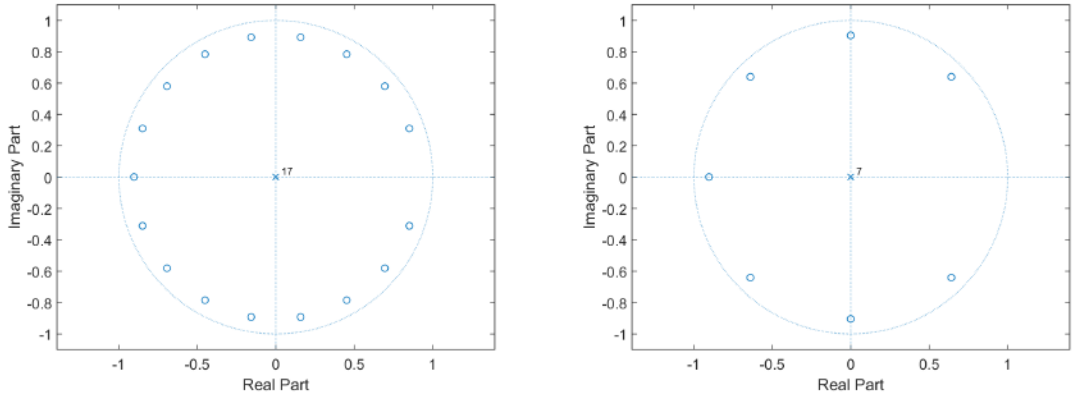

(a) (b)

Figure 4.4: Zero-pole diagram of (a) $H_{\tilde{k}_x}$ and (b) $H_{\tilde{k}_y}$.

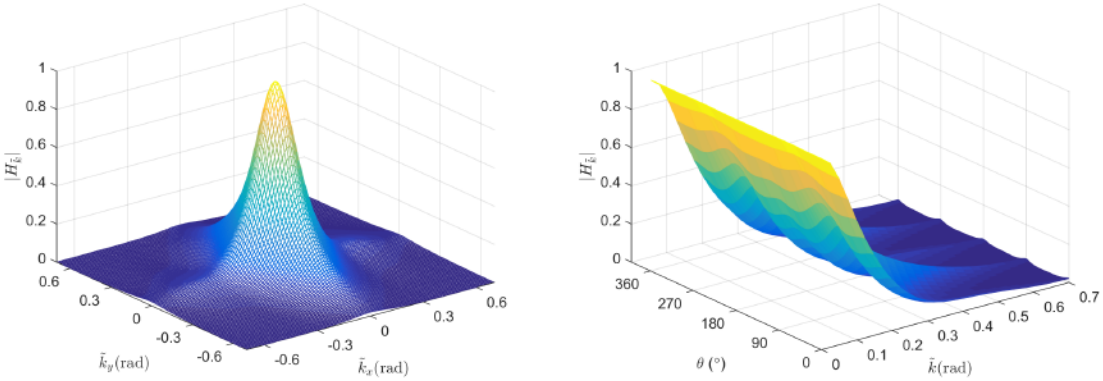

(a) (b)

Figure 4.5: The directional wave number response of $H_{\tilde{k}}$ in (a) $\tilde{k}_x, \tilde{k}_y$ and (b) $\tilde{k}, \theta$ domain.

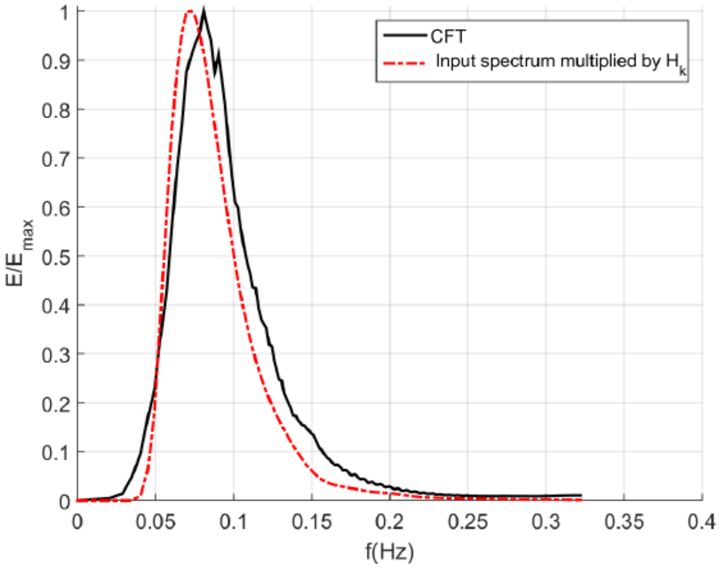

Figure 4.6: The modified input non-directional wave spectrum overlaid by the CFT-estimate of the non-directional wave spectrum.

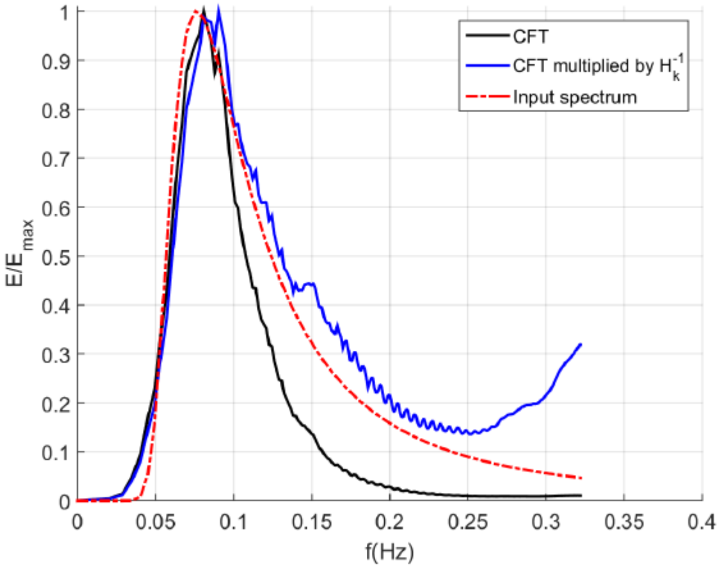

Figure 4.7: A demonstration of the improvement in CFT-estimate of the non-directional ocean wave spectrum shaped by $H_{\tilde{k}}^{-}1$ using simulated data.

In the x direction, the moving average filter in the spatial domain can be stipulated by the rectangular window

$$h_x(x) = \frac{1}{L_x} u(x + L_x/2) u(-x + L_x/2).$$

where $u(\cdot)$ is the unit step function. Using the Laplace transform,

$$H_{k_x}(k_x) = \int_{-\infty}^{\infty} h_x(x) \mathrm{e}^{-sx} dx = \frac{\mathrm{e}^{s_x L_x/2} - \mathrm{e}^{-s_x L_x/2}}{s_x L_x} \tag{4.5}$$

where $s_x = \sigma + jk_x$, with σ being the attenuation constant. Similarly,

$$H_{k_y}(k_y) = \frac{\mathrm{e}^{s_y L_y/2} - \mathrm{e}^{-s_y L_y/2}}{s_y L_y} \tag{4.6}$$

where $s_y = \sigma + jk_y$. Using the parameters given in Table 4.1 and considering $\sigma = -0.1$ for a invertible analog filter (see Section 4.2.3), Figure 4.8a and Figure 4.8b show the directional wave number response of H_k in the (k_x, k_y) and (k, θ) domain, respectively. Since H_k is invertible, $H_k^{-1} = 1/H_k$ can be used to mitigate the effect of the radar sampling process on radar field data. H_k^{-1} is referred to as the Inverse Sampling Averaging Filter (ISAF). For radar field data, the ISAF is used with the modulation transfer function $MTF = k^{-1.2}$ proposed in [11]. The ISAF filter is integrated in the CFT method outlined in Section 2.3.2 by updating Equation 2.7 as follows.

$$E_c(\mathbf{k}) = k^{-1.2} E_k(\mathbf{k}) H_k^{-1}(\mathbf{k}).$$

4.2.3 Filter inversion and the attenuation constant σ

Using the attenuation constant $\sigma = 0$ in Equations 4.5 and 4.6 produces a non-invertible wave number response due to the zeros shown in Figures 4.9a and 4.9b, respectively, being on the unit circle of the z-plane. This is the case because once the radar averages the returned scatter from all positions in the sample area, information

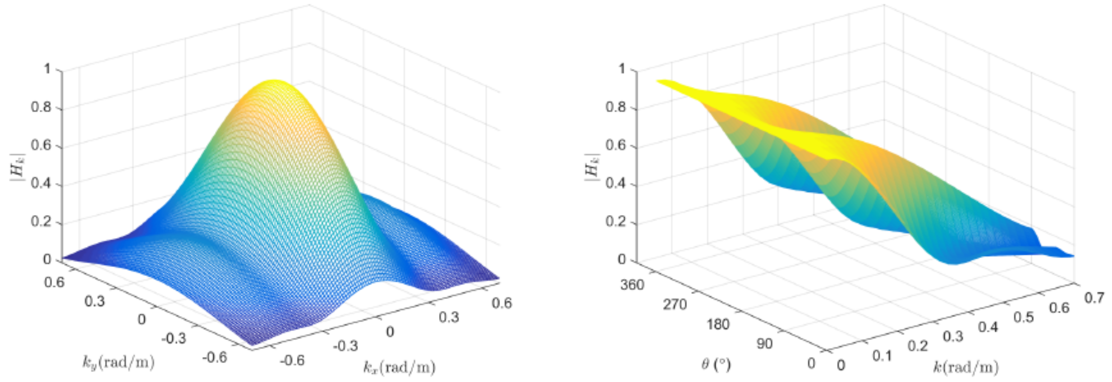

(a) (b)

Figure 4.8: The directional wave number response of H_k in (a) k_x, k_y and (b) k, θ domain.

about individual positions cannot be retrieved from the radar output. Still, we can use an interpolation of the filter by setting $\sigma = -0.1$ in Equations 4.5 and 4.6. This value was chosen so that the interpolation follows the envelope of the original filter with $\sigma = 0$ as shown in Figures 4.9a and 4.9b. Choosing a lower value of σ, such as -0.2, might lead to an underestimation of wave spectra components at low wave numbers due to the high amplitude response of $|H_{k_x}|$ at those wave numbers as depicted in Figure 4.5. On the other hand, using a higher value of σ such as -0.05 might lead to an unstable behavior of the inverse filter due to the small values of $|H_{k_x}|$ and $|H_{k_y}|$ at their zeros. For the same reason, $r = 0.9$ was used in Equations 4.3 and 4.4. This value was found using the Z-Laplace transform relationship theory, where [67]

$$z = r_z \mathrm{e}^{j\tilde{k_x}} = \mathrm{e}^{s_x dx} = \mathrm{e}^{(\sigma + jk_x)dx} = \mathrm{e}^{\sigma dx}\mathrm{e}^{jk_x dx}.$$

Therefore, $r_z = \mathrm{e}^{\sigma dx}$. Using $\sigma = -0.1$ and $dx = 1$ m as shown in Table 4.1 leads to $r = 0.9$.

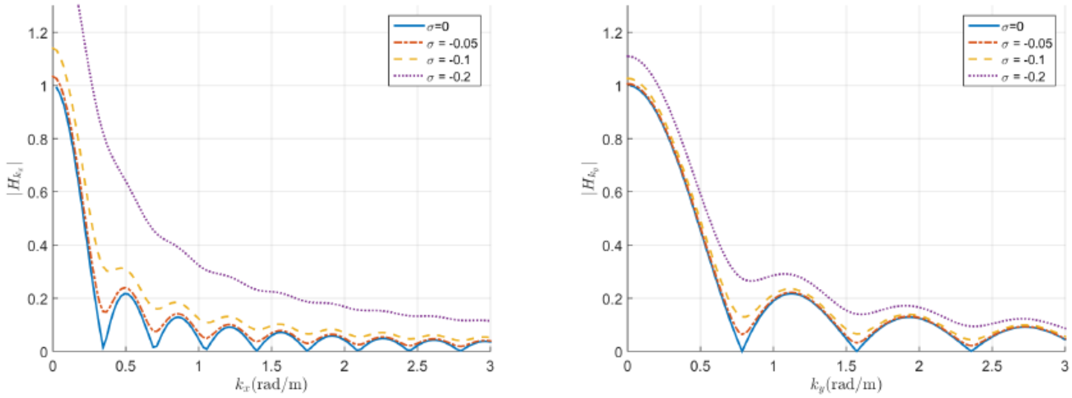

(a) (b)

Figure 4.9: (a and b) The magnitude of the x and y components, respectively, of the analog averaging filter (H) for σ = 0, -0.05, -0.1 and -0.2.

4.3 Results and Analysis

4.3.1 Field data examples

In this section, three field data examples of ocean wave spectral estimation using the CFT-with-ISAF method and the CFT-without-ISAF method are presented to demonstrate the performance of the ISAF. Figure 4.10 shows: (a) a ground truth directional wave spectrum estimated from TRIAXYS Wave Rider buoy data, (b) the estimated directional wave spectrum using the CFT-without-ISAF, (c) the estimated directional wave spectrum using the CFT-with-ISAF method, and (d) the non-directional wave spectra deduced from the three directional wave spectra. In the case of a directional wave spectrum with multiple peaks, the terminology used in this discussion is that the peak with the highest peak energy is referred to as the main peak, while the other peaks are referred to as the secondary peaks. Also, since we are dealing with normalized wave spectra, the energy level of secondary peaks is measured with respect to the energy level of the main peak of the same spectrum. Figures 4.10a and 4.10d show that the ground truth wave spectra have a main peak at 0.135 Hz and

243° and a secondary peak at 0.08 Hz and 114° with relative energy level of 70%. Looking at the estimates of the directional and non-directional wave spectra that are generated using the CFT-without-ISAF method shown in Figures 4.10b and 4.10d, respectively, both peaks were detected. However, the main peak was barely detected and was detected as the secondary peak at 0.128 Hz and 245° with a relative energy level of 43%, while the secondary peak was detected as the main peak at 0.075 Hz and 100°. On the other hand, when the ISAF was implemented in the CFT method, as shown in Figures 4.10c and 4.10d, both peaks were properly detected. The main peak was detected as the main peak at 0.134 Hz and 245° and the secondary peak was detected as a secondary peak at 0.075 Hz and 100° with a relative energy level of 78%. Clearly, the ISAF has significantly improved the wave spectrum estimation in this example. Figure 4.10d also shows better agreement between the ground truth non-directional spectrum and the spectrum obtained by the CFT-with-ISAF method compared to the CFT-without-ISAF.

The same conclusion may be drawn from the example given in Figures 4.11. The ground truth directional wave spectrum shown in Figure 4.11a contains four peaks located at 0.03 Hz and 140°, 0.03 Hz and 290°, 0.14 Hz and 75°, and 0.16 Hz and 250°. For convenience, these peaks are referred to as P1, P2, P3, and P4. It can be seen from Figures 4.10b and 4.10c that P1 and P2 were not detected by CFT-with-ISAF and detected by the CFT-without-ISAF. However, P3 and P4 were detected more accurately in terms of peak location and relative energy as shown in Figure 4.11d. Since most of the spectrum energy is actually contained in P3 and P4, it can be concluded that the CFT-with-ISAF outperforms the CFT-without ISAF in this example too.

Finally, Figure 4.12 shows another example for comparison between the CFT-with-ISAF and CFT-without-ISAF. In this example, non-directional wave spectrum estimates generated using both methods show a good agreement with the non-directional ground truth wave spectrum as shown in Figure 4.12d. However, the CFT-with-ISAF estimate shows a slight advantage for the CFT-with-ISAF estimate in terms of agreement with the ground truth non-directional wave spectrum.

4.3.2 Performance validation

In order to validate the performance of the ISAF, the CFT was used to estimate the wave spectra with and without implementing the ISAF. The results were compared to the ground truth wave spectra that were estimated using the TRIAXYS wave rider buoy, which produces one reading every 30 minutes. For a proper comparison, all CFT estimates from image sets (32 images) that the radar produced within a 30-minute window are averaged to be compared with the buoy reading produced in the same window. The correlation coefficient estimate, given by Equation 3.1, between the ground truth and the CFT-estimated non dimensional wave spectrum was used as an agreement measure between the two spectra. The value of the coefficient ranges from 0 (no agreement) to 1 (identical). Figure 4.13 shows the correlation coefficient in pairs: the CFT-without-ISAF coefficient is marked using a “o” while the CFT-with-ISAF is marked using a “ × ”; the results are shown for four 12-hour periods during Dec 1 - Dec 4, 2008. To enhance the readability of the results, the CFT-with-ISAF output is plotted in blue and red to indicate improvement and deterioration in performance, respectively, compared to the CFT-without-ISAF method. Clearly, the performance of CFT has significantly improved with the implementation of the ISAF with higher correlation coefficients except for a few cases. On average, an improvement on the agreement with the ground truth of 11% has been achieved. Ultimately, this improvement is expected to reflect positively in the estimation of sea state parameters.

For further validation, the CFT with ISAF method and the standard CFT method are used to estimate the peak wave period T_p, mean period T_{01}, the zero-crossing period T_z and the peak wave direction θ_p. The estimates are then compared with the ground truth buoy-estimates. Figures 4.14 and 4.15 show the peak wave period and direction, respectively. The mean absolute errors ($\overline{|\varepsilon_{T_p}|}$,$\overline{|\varepsilon_{T_{01}}|}$, $\overline{|\varepsilon_{T_z}|}$ and $\overline{|\varepsilon_{\theta_p}|}$) and error standard deviations ($\sigma_{\varepsilon_{T_p}}$, $\sigma_{\varepsilon_{T_{01}}}$, $\sigma_{\varepsilon_{T_z}}$ and $\sigma_{\varepsilon_{\theta_p}}$) of these estimates are calculated with respect to the ground truth and listed in Table 4.2. Figure 4.16 shows the normalized (with respect to the CFT) average absolute error in estimating T_p, T_{01}, T_z, and θ_p using the ISAF method. The mean absolute error and the error standard deviation of T_p are given by Equations 3.2 and 3.3, respectively. The other metrics are calculated in a similar manner. Improvements are observed in estimating sea state parameters. For $\overline{|\varepsilon_{T_p}|}$, $\overline{|\varepsilon_{T_{01}}|}$, $\overline{|\varepsilon_{T_z}|}$, and $\overline{|\varepsilon_{\theta_p}|}$, improvements of 12%, 20%, 20%, and 33% were achieved.

Table 4.2: Comparison of the CFT with and without the ISAF in wave period and peak direction estimation.

	$\overline{\lvert\boldsymbol{\varepsilon_{T_p}}\rvert}$(s)	$\boldsymbol{\sigma_{\varepsilon_{T_p}}}$ (s)	$\overline{\lvert\boldsymbol{\varepsilon_{T_{01}}}\rvert}$(s)	$\boldsymbol{\sigma_{\varepsilon_{T_{01}}}}$ (s)	$\overline{\lvert\boldsymbol{\varepsilon_{T_z}}\rvert}$(s)	$\boldsymbol{\sigma_{\varepsilon_{T_z}}}$ (s)	$\overline{\lvert\boldsymbol{\varepsilon_{\theta_p}}\rvert}$(°)	$\boldsymbol{\sigma_{\varepsilon_{\theta_p}}}$ (°)
CFT-without-ISAF	2.5	0.9	2.4	0.8	2.3	0.8	15.1	16.1
CFT-with-ISAF	2.2	0.5	1.9	0.5	1.9	0.5	9.9	6

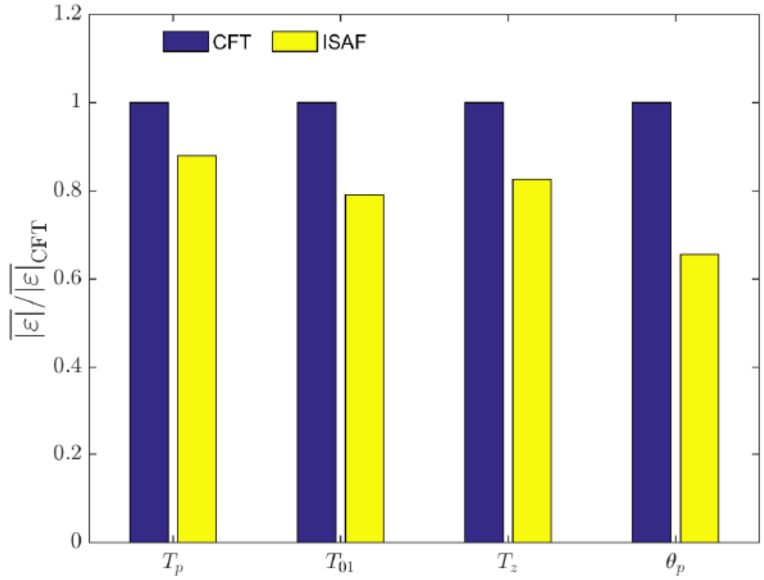

Figure 4.16: The average absolute error of the ISAF normalized with respect to the CFT method.

4.4 Conclusions

In the literature, the process of ocean surface sampling using X-band marine radar has been considered as a standard sampling. Thus, the influence of ocean surface sampling on the ocean wave spectra estimation using the CFT has not been previously addressed. In this chapter, the ocean wave surface sampling process has been modelled and a novel understanding of it being an averaging process has been presented. A 2-D low pass filter model has been presented to describe the effect of the sampling process on the CFT method estimates of the ocean wave spectra. Furthermore, a filter referred to as the Inverse Sampling Moving Average Filter (ISAF) has been proposed to mitigate that effect. The performance of the ISAF was validated against ground truth data that were obtained from a TRIAXYS wave rider buoy. Results show that implementing the ISAF in the CFT method of ocean wave spectral estimation significantly improves the accuracy of the method. The improvement measures that were considered in this paper include the accuracy of estimating the non-directional wave spectrum, the peak wave period, the mean wave period, the zero-crossing wave period, and the peak wave direction. Future work on the ISAF will include further validation involving other ocean state parameters such as the significant wave height and surface current estimation.

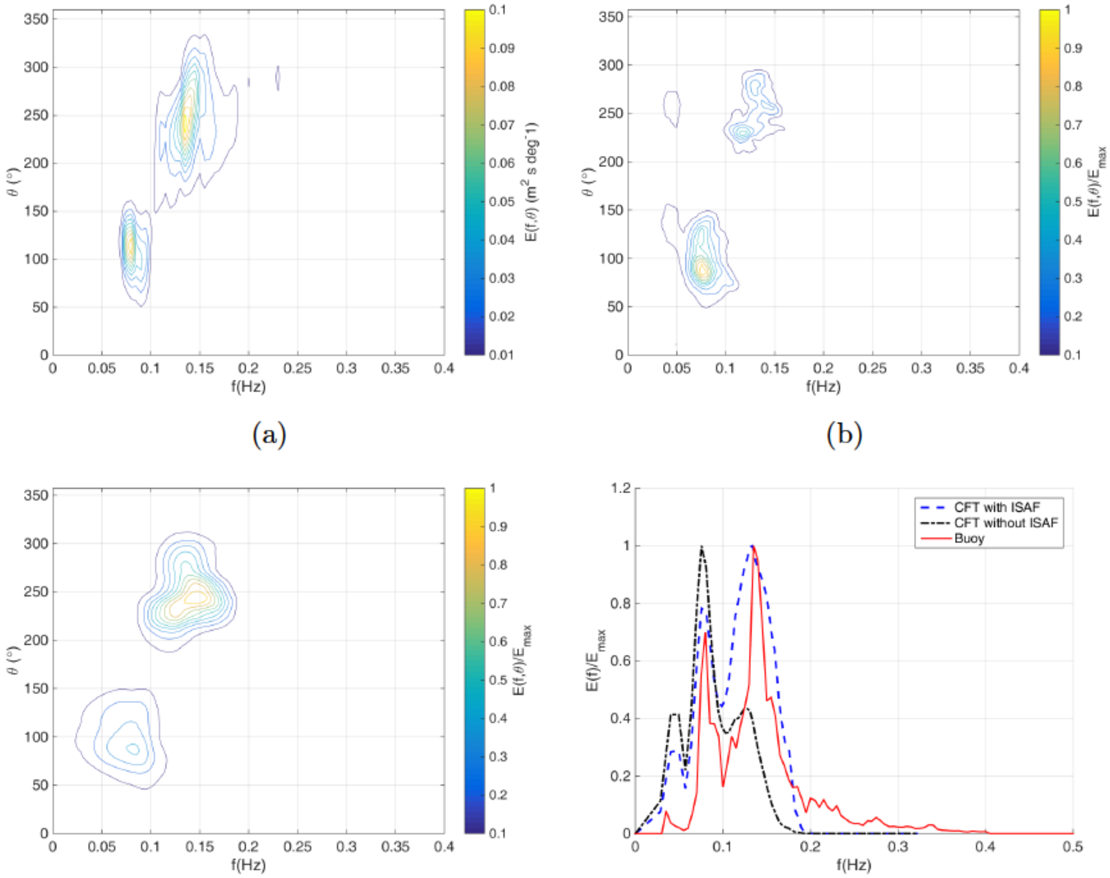

(a) (b)

(c) (d)

Figure 4.10: A field data example to demonstrate the improvement introduced by the ISAF to the CFT-method in ocean wave spectral estimation. Data were recorded on Nov 29, 2008 between 8:08 PM and 8:38 PM: (a) The ground truth directional wave spectrum estimated using the TRIAXYS Wave Rider buoy data. (b and c) The directional wave spectrum estimated using the CFT-without-ISAF and the CFT-with-ISAF method, respectively. (c) The non-directional wave spectra estimated using the CFT-without-ISAF, the CFT-with-ISAF method, and the TRIAXYS Wave Rider buoy data.

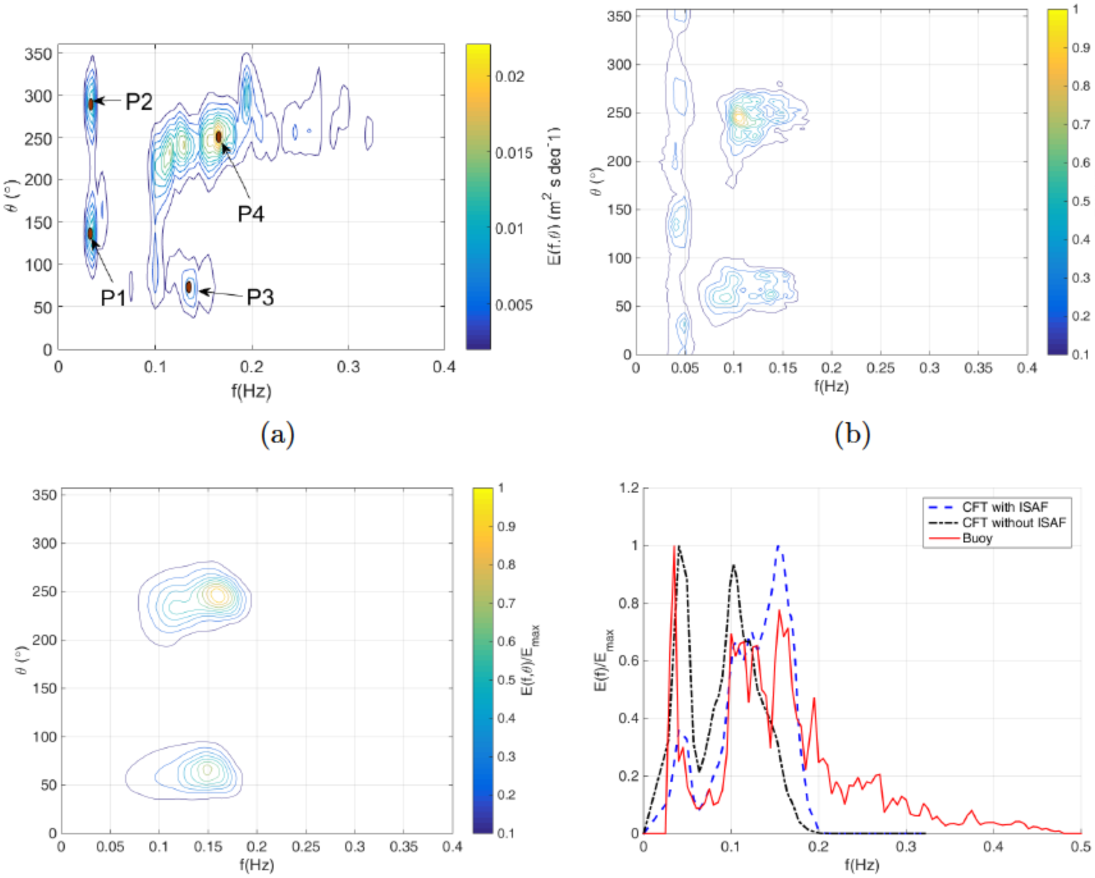

(a) (b)

(c) (d)

Figure 4.11: A field data example to demonstrate the improvement introduced by the ISAF to the CFT-method in ocean wave spectral estimation. Data were recorded on Dec 4, 2008 between 11:26 AM and 11:56 AM: (a) The ground truth directional wave spectrum estimated using the TRIAXYS Wave Rider buoy data. (b and c) The directional wave spectrum estimated using the CFT-without-ISAF and the CFT-with-ISAF method, respectively. (c) The non-directional wave spectra estimated using the CFT-without-ISAF, the CFT-with-ISAF method, and the TRIAXYS Wave Rider buoy data.

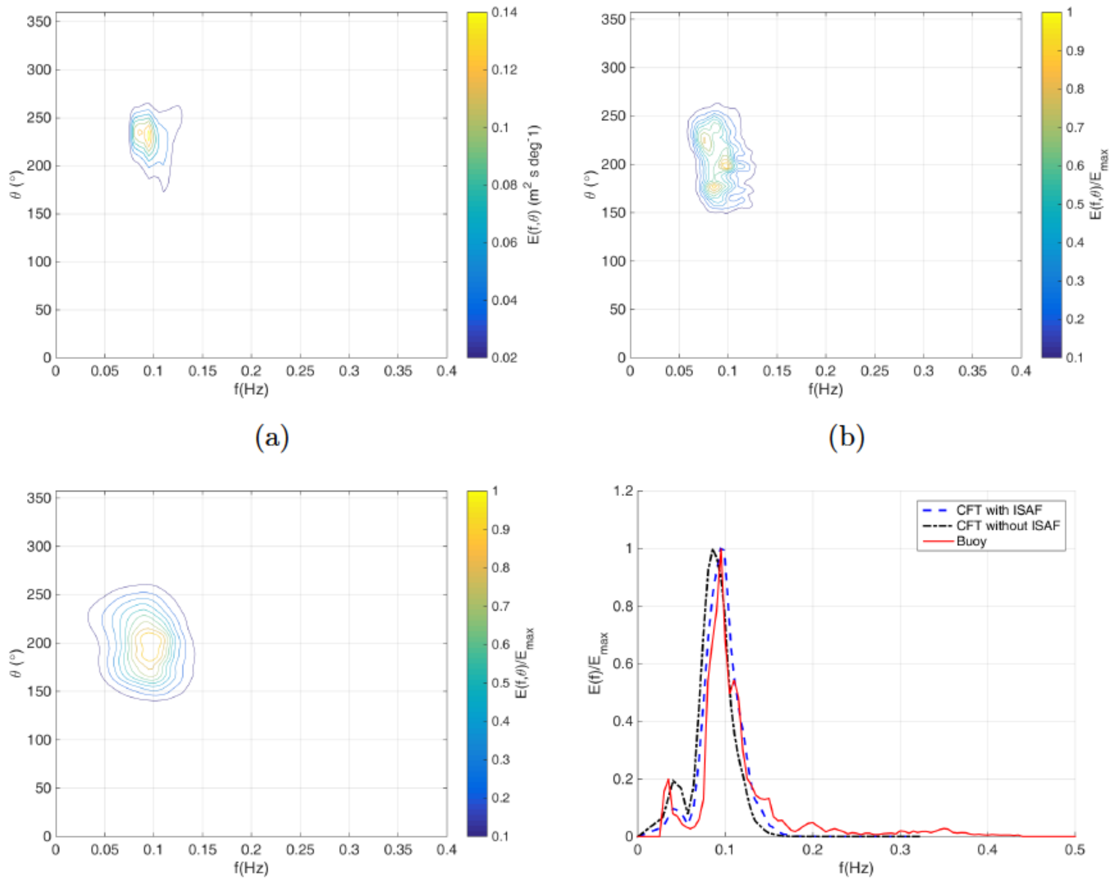

(a) (b) (c) (d)

Figure 4.12: A field data example to demonstrate the improvement introduced by the ISAF to the CFT-method in ocean wave spectral estimation. Data were recorded on Dec 03, 2008 between 10:29 AM and 10:59 AM: (a) The ground truth directional wave spectrum estimated using the TRIAXYS Wave Rider buoy data. (b and c) The directional wave spectrum estimated using the CFT-without-ISAF and the CFT-with-ISAF method, respectively. (c) The non-directional wave spectra estimated using the CFT-without-ISAF, the CFT-with-ISAF method, and the TRIAXYS Wave Rider buoy data.

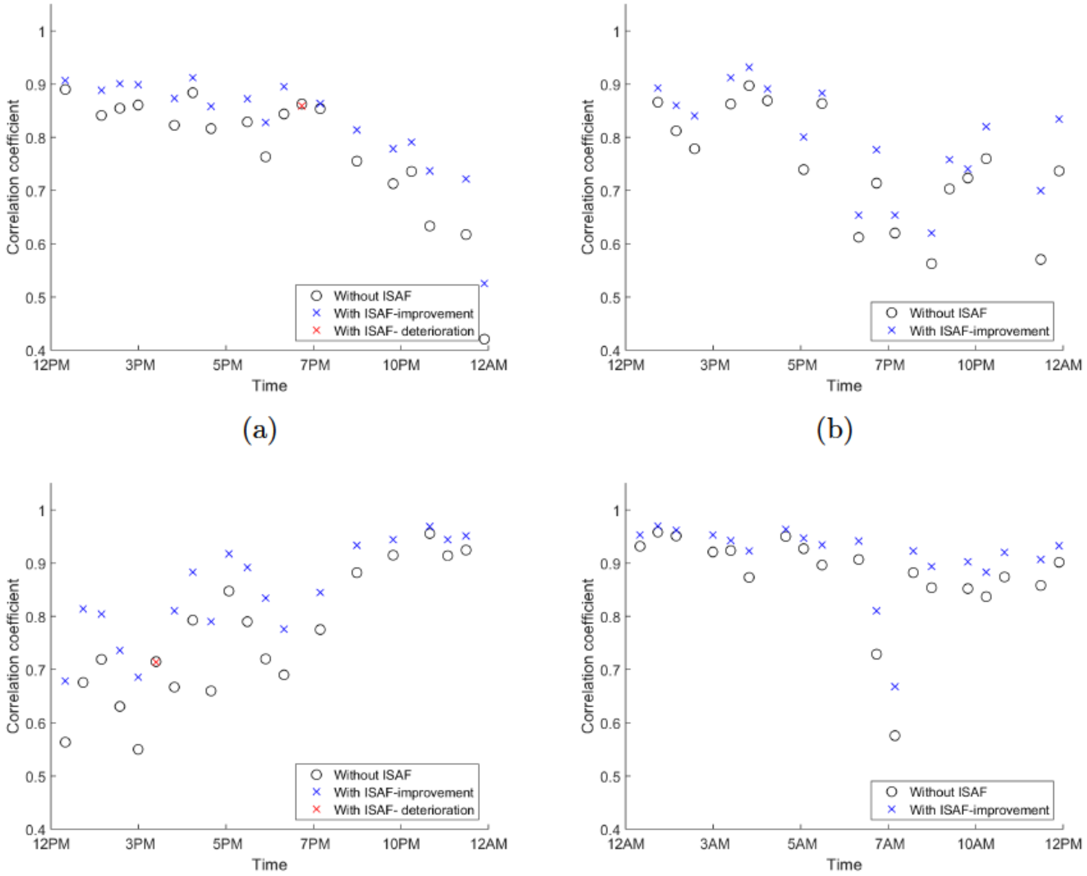

(a) (b)

(c) (d)

Figure 4.13: A comparison of the CFT with and without the ISAF in terms of the wave frequency spectrum similarity with respect to the buoy ground truth spectra. Each point represents the correlation coefficient between ground truth and the radar data 30 minute averaged frequency wave spectra. (a) Dec 1 afternoon and evening, (b) Dec 2 afternoon and evening, (c) Dec 3 afternoon and evening, (d) Dec 4 morning.

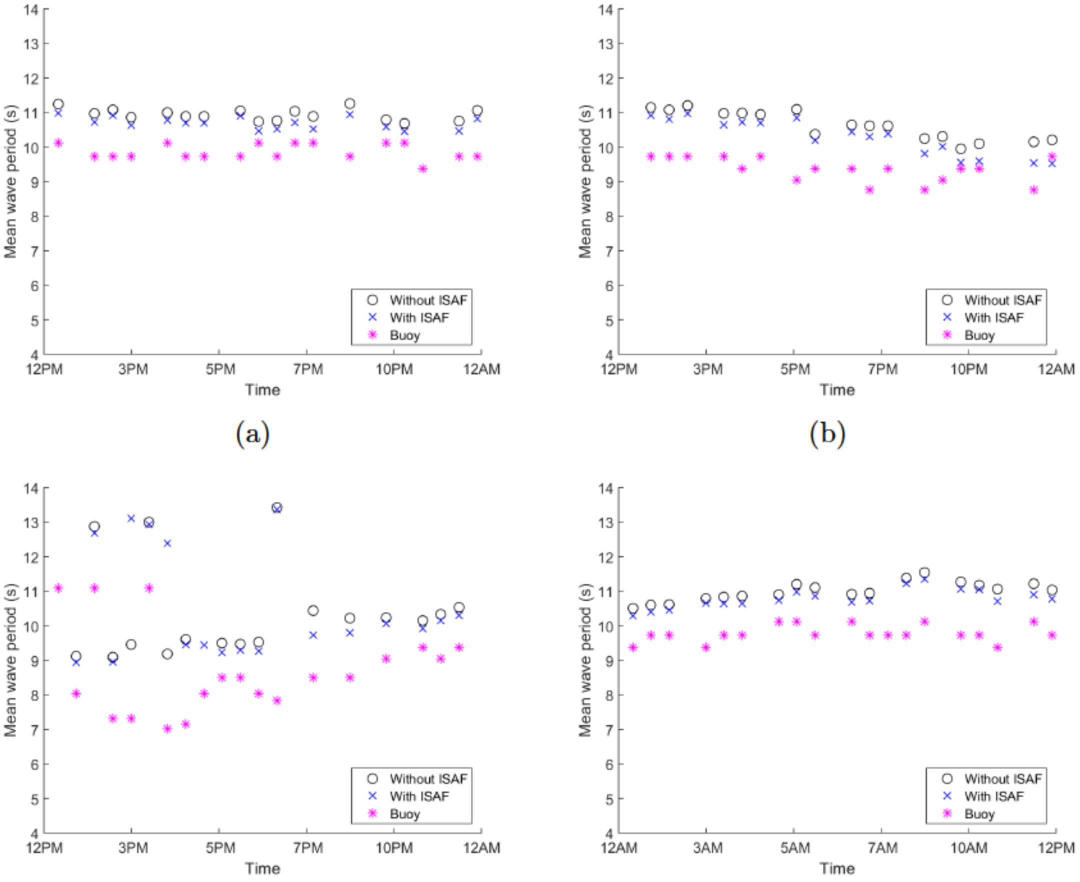

(a) (b)

(c) (d)

Figure 4.14: A comparison of the CFT with and without the ISAF in terms of the wave peak period. (a) Dec 1 afternoon and evening, (b) Dec 2 afternoon and evening, (c) Dec 3 afternoon and evening, (d) Dec 4 morning.

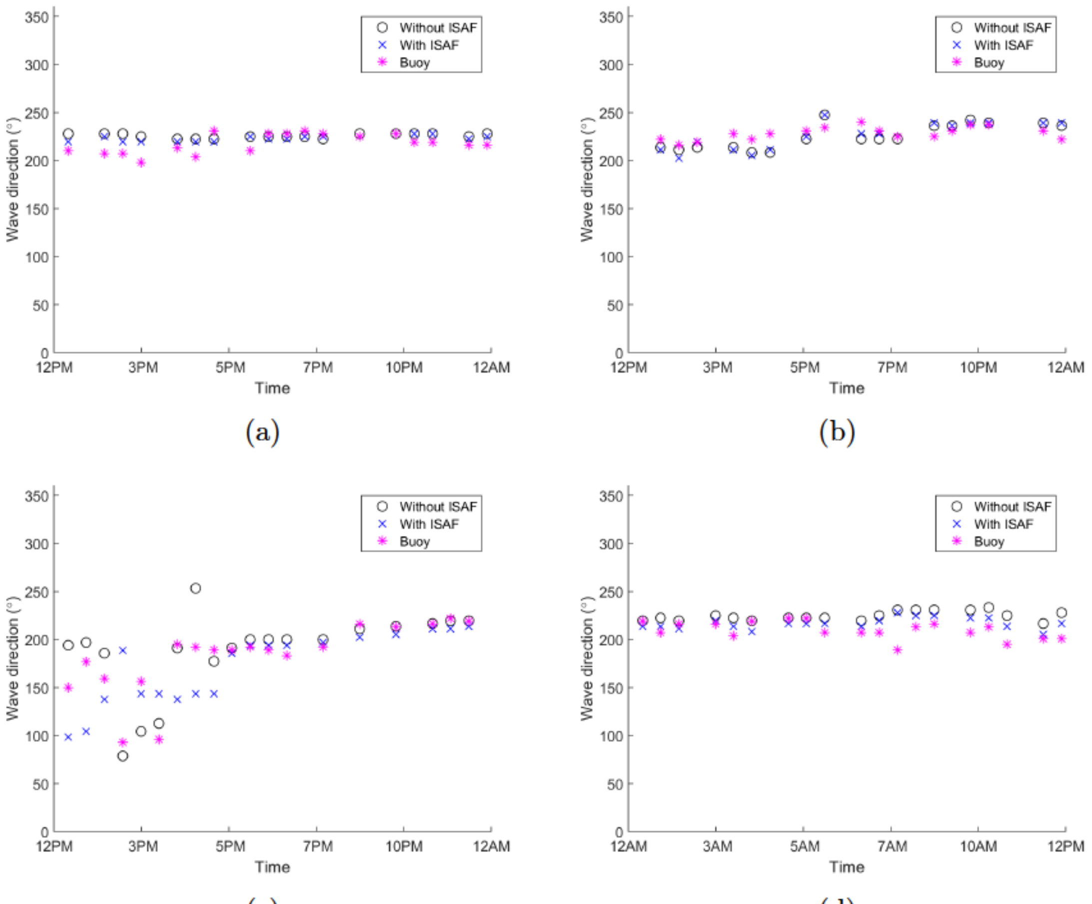

(a) (b)

(c) (d)

Figure 4.15: A comparison of the CFT with and without the ISAF in terms of the wave peak direction.(a) Dec 1 afternoon and evening, (b) Dec 2 afternoon and evening, (c) Dec 3 afternoon and evening, (d) Dec 4 morning.

Chapter 5

Using the Polar Fourier Transform (PFT) in wave spectra estimation using X-band marine radar

5.1 Introduction

Another source of error that is addressed in this thesis is the process of scan conversion. This process is used to convert radar images from polar coordinates to the Cartesian coordinates before applying the CFT. Different reasons contributed to the adoption of the scan conversion process in X-band radar-based ocean wave spectra estimation methods. First, conducting the ocean wave spectral analysis in the Cartesian domain is mainly inherited from the target detection and navigation application of X-band marine radars. Second, the popularity of the Cartesian Fourier transformation and its computational efficiency in the Fast Fourier Transform (FFT) further motivated using the Cartesian analysis in wave spectra estimation using X-band radars. Understanding the effect of scan conversion on wave spectra estimation can be challenging due to its changing behavior with range. In this chapter, an estimation algorithm is proposed to eliminate the error introduced by the scan conversion process by adopting Fourier analysis in polar coordinates. Doing so implies dropping the step of scan conversion.

5.2 The effect of scan conversion on the estimated wave spectra

Scan conversion, as explained in Section 2.3.1, is used to convert B-scan images to Cartesian images in preparation for applying CFT. To the best of our knowledge, the effect of the scan conversion process on the wave spectral estimation using the CFT method has not been addressed in the literature. Revisiting the process of scan conversion, it can be observed that the mapping algorithm in the process is not one-to-one. In fact, it is common in the areas that are far from the image centre that multiple Cartesian samples are assigned to a single B-scan sample as shown in the lower right diagram of Figure 5.1. This is due to the larger B-scan samples' areas compared to the Cartesian samples' area at high ranges. Therefore, a B-scan sample can cover multiple Cartesian samples. In this case, an up-sampling or interpolation process takes place. Also, it is possible to have one Cartesian sample being assigned to multiple B-scan samples. In this case, the Cartesian sample is filled by the value of one of the corresponding B-scan samples or by the average of the corresponding B-scan samples. The latter scenario is common near the centre where the B-scan samples' areas are usually smaller than the Cartesian samples' area. This case can be seen in the lower left diagram if Figure 5.1.

Mathematically, scan conversion is a process of re-sampling in which the original continuous signal (ocean surface image) is reconstructed. Subsequently, the reconstructed continuous image is sampled on a new Cartesian grid. According to the sampling theorem, in order to perfectly and uniquely reconstruct a continuous signal from its sampled representation, an ideal low pass filter is needed and the original signal is required to be strictly band-limited. These requirements are not applicable here and only approximations of low pass filters are used.

Practically, several methods of interpolation and/or decimation may be used to perform the scan conversion process. These include ray tracing, space-variant interpolation, and space semi-invariant interpolation [13]. In the LUT method, for instance, these methods are used to determine the weight of each contributing B-scan sample from the LUT in calculating Cartesian samples. The trade-off between these methods is complexity versus the amount of distortion added to the wave spectrum.

In this chapter, we take the approach of eliminating the scan conversion process entirely by applying a form of Fourier transformation on the radar output directly in its B-scan native format. This requires the implementation of a Polar Fourier Transform (PFT) that suits the polar sampling nature of the digitized B-scan samples. The Polar Fourier Transform (PFT) that is adopted in this thesis was introduced by Wang *et al* in 2009 [17].

5.3 The Polar Fourier Transform (PFT)

Figure 5.2 shows the flow chart of the PFT method in estimating the wave spectra compared to the traditional CFT method. It can be seen that both methods produce a 3D image spectrum. The subsequent analysis for estimating ocean wave spectra and sea state parameters, as outlined in Section 2.3.2, are the same for both methods. It is important to point out that the analysis windows in the PFT take the shape of ring sectors as compared to rectangular windows for the CFT method (See Figure 5.3). Another advantage of the PFT method lies in the compatibility of the shape of the

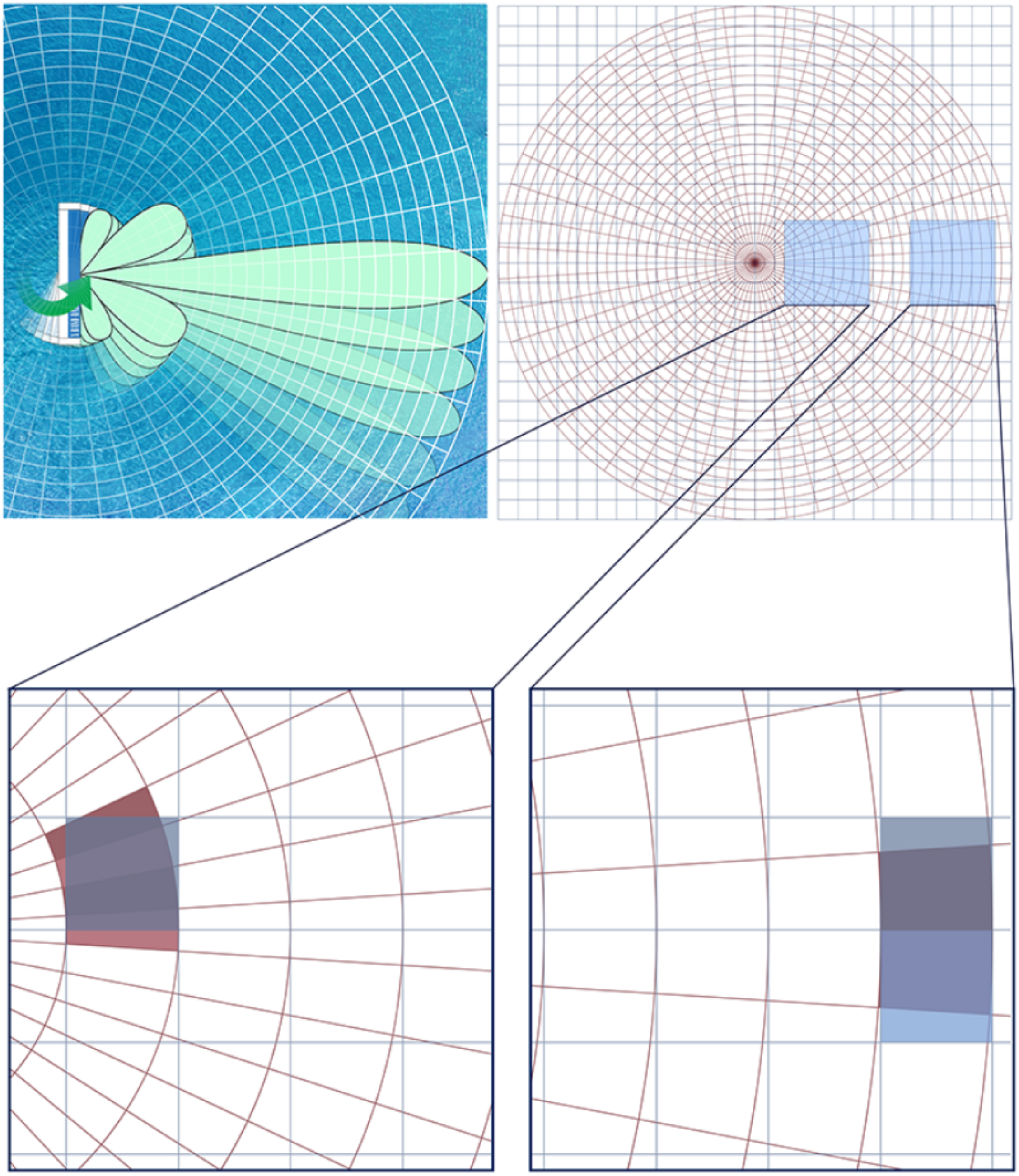

Figure 5.1: An illustration of the scan conversion process: (Upper left) a diagram shows the radar sampling process on a polar grid. (Upper right) a polar grid over which the ocean surface is sampled by the radar overlaid by the Cartesian grid used in scan conversion. (Lower left) an enlargement of a near range sampling area. (Lower right) an enlargement of a far range sampling area. Figure dimensions are not to scale.

analysis windows and the native layout of B-scan images. Such compatibility allows the availability of all B-scan samples to be used in the analysis. Using rectangular windows on the other hand, as in the CFT method, limits the availability of samples that are located at near or far ranges. For instance, the blue ring sector analysis window shown in Figure 5.3b include more samples at the maximum range compared to the blue rectangular analysis window shown in Figure 5.3a, which can only include the maximum range samples that are located at the far corners of the window. Furthermore, since the intensity of returned scatter and shadowing are affected by the range, their effect is expected to be more uniform when using ring sector analysis windows compared to rectangular analysis windows. It should be noted that a ring sector analysis window is acquired by applying a rectangular analysis window on the B-scan data directly as depicted in Figure 5.4.

5.3.1 Derivation of the PFT

Since scan conversion deals with spatial coordinates only where it maps from one set of spatial coordinates (r, φ) to another (x, y), the problem is time independent and can be addressed in spatial coordinates only. This reduces the problem to 2D instead of 3D. The CFT basis functions, $e^{jk_x x} e^{jk_y y}$, can be found by solving for the eigenfunctions of the Laplacian, which in the Cartesian coordinates takes the form

$$\nabla^2 = \nabla_x^2 + \nabla_y^2 = \frac{\partial^2}{\partial x^2} + \frac{\partial^2}{\partial y^2}.$$

Similarly, the basis functions of a polar Fourier transform can be found by solving for the eigenfunctions of the Laplacian in polar coordinates, which is given by

$$\nabla^2 = \nabla_r^2 + \frac{1}{r^2} \nabla_\varphi$$

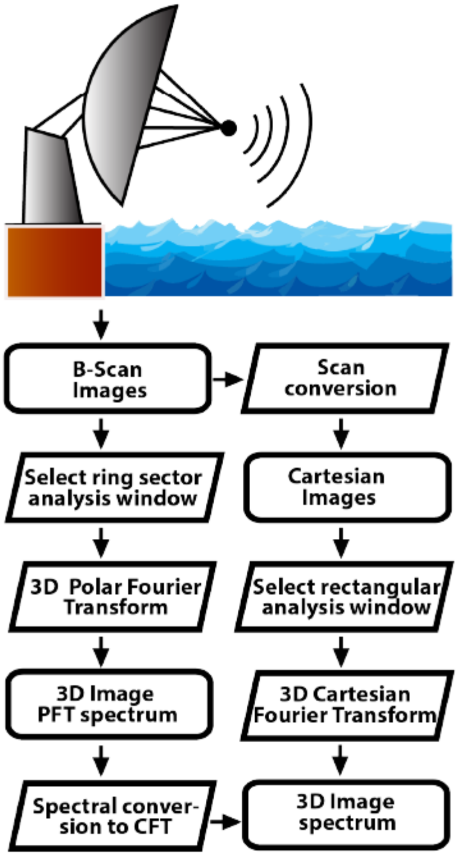

Figure 5.2: Polar Fourier transform method.

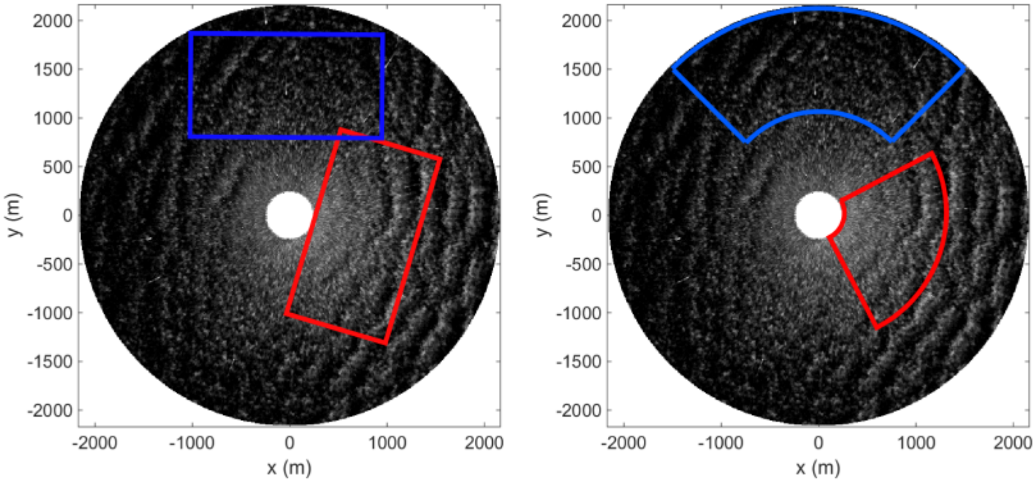

(a) (b)

Figure 5.3: (a) CFT analysis windows. (b) PFT analysis windows.

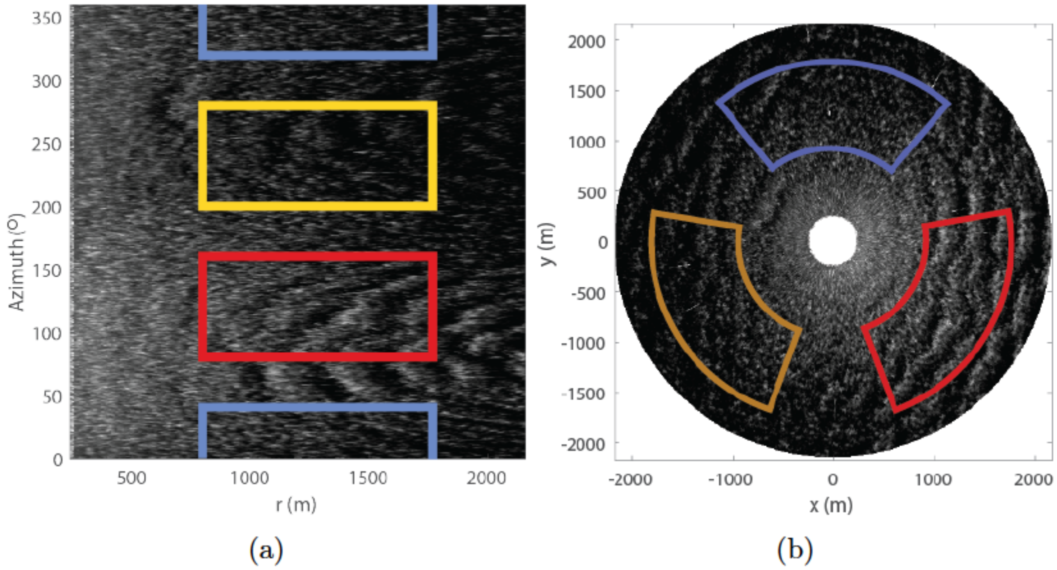

Figure 5.4: (a) Ring sector analysis windows in B-scan domain. (b) Ring sector analysis windows in Cartesian domain.

where

$$\nabla_r^2 = \frac{1}{r}\frac{\partial}{\partial r}\left(r\frac{\partial}{\partial r}\right)$$

and

$$\nabla_\varphi^2 = \frac{\partial^2}{\partial \varphi^2}.$$

The Eigenvalue problem can be written as

$$\nabla_r^2\Psi(r,\varphi) + \frac{1}{r^2}\nabla_\varphi^2\Psi(r,\varphi) + k^2\Psi(r,\varphi) = 0. \tag{5.1}$$

which is the Helmholtz equation in polar coordinates. Substituting a separation of variables, $\Psi(r,\varphi) = R(r)\Phi(\varphi)$, Equation 5.1 may be written as

$$\frac{\partial^2}{\partial \varphi^2}\Phi + m\Phi = 0, \tag{5.2}$$

and

$$\frac{1}{r}\frac{\partial}{\partial r}\left(r\frac{\partial}{\partial r}\right)R + \left(k^2 - \frac{m^2}{r^2}\right)R = 0. \tag{5.3}$$

The solution of Equation 5.2 is

$$\Phi_m(\varphi) = \frac{1}{\sqrt{2\pi}} e^{(jm\varphi)},$$

where m is an integer, and the general non-singular solution of Equation 5.3 is

$$R_{k,m}(r) = \sqrt{k} J_m(kr), \tag{5.4}$$

where J_m is the Bessel function of the first kind of order m. This solution satisfies orthogonality over the radial direction as

$$\Upsilon(k) = \int_0^\infty J_m(k_0 r) J_m(kr) r dr = \frac{1}{k_0 - k} \delta(k_0 - k), \tag{5.5}$$

where $\delta(.)$ is the Dirac delta function, and k_0 is an arbitrary wave number. The basis functions of the PFT are given in [17] as,

$$\Psi_{k,m}(r,\varphi) = R_{k,m}(r)\Phi_m(\varphi) = \sqrt{\frac{k}{2\pi}} J_m(kr) e^{(jm\varphi)}.$$

and the forward PFT is given by

$$P(k,m) = \int_0^\infty \int_0^{2\pi} f(r,\varphi) \Psi^*_{k,m}(r,\varphi) r d\varphi dr, \tag{5.6}$$

where '*' represents complex conjugation and $P(k,m)$ is the PFT spectrum. The inverse PFT is given by

$$f(r,\varphi) = \sum_{m=-\infty}^{\infty} \int_0^\infty P(k,m) \Psi_{k,m}(r,\varphi) k dk.$$

5.3.2 Application to radar images

In ocean wave spectral remote sensing applications, as in other real world applications, the range dimension r is limited. Hence, the orthogonality described by Equation 5.5

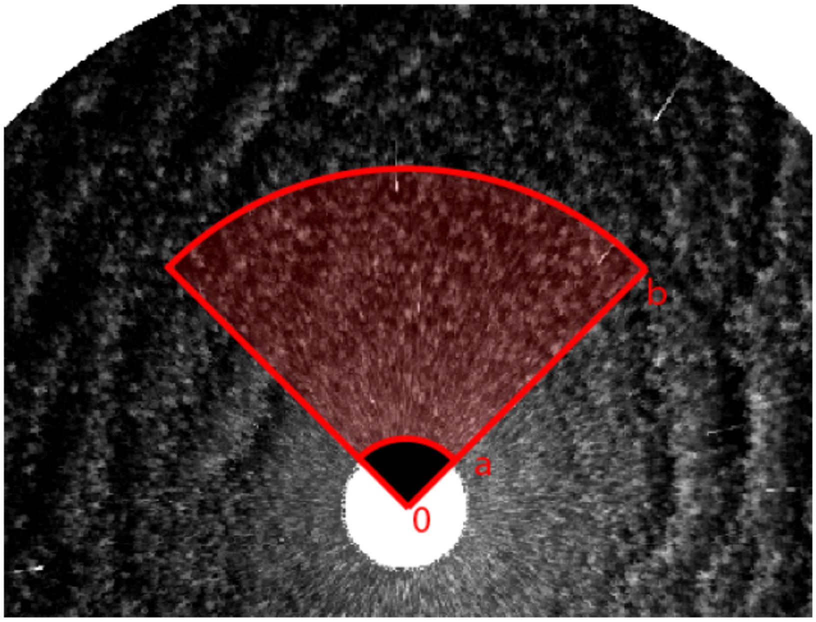

Figure 5.5: Zero-padding in the PFT analysis window.

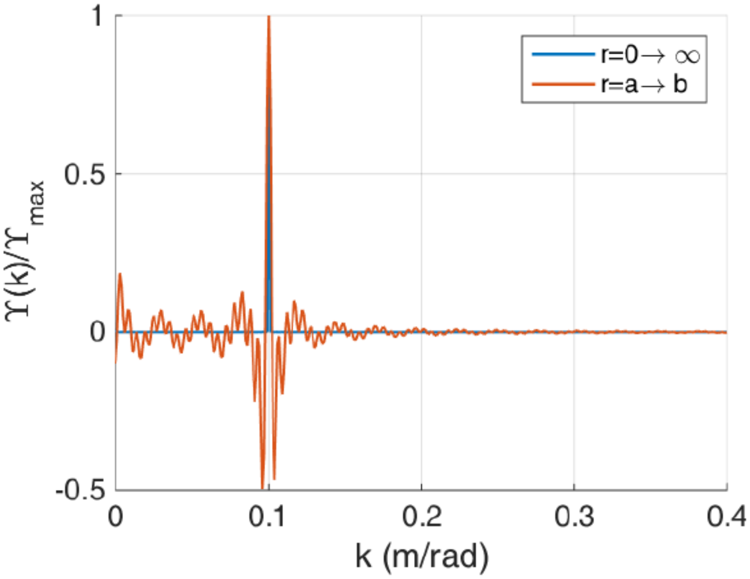

Figure 5.6: Orthogonality of Bessel functions for infinite and finite ranges presented in Equation 5.7. The values $m = 0, k_0 = .1$ rad/m are used, without losing the generality.

does not strictly hold, at least not for all values of k. Instead, for limited $r \in [a, b]$, as shown in Figure 5.5,

$$
\begin{aligned}
\Upsilon(k) = \int_a^b J_m(k_0 r) J_m(kr) r dr = \\
\frac{b}{k_0^2 - k^2} \left[k J_m(k_0 b) J_m'(kb) - k_0 J_m(kb) J'(k_0 b)) \right] \\
-\frac{a}{k_0^2 - k^2} \left[k J_m(k_0 a) J_m'(ka) - k_0 J_m(ka) J'(k_0 a)) \right]
\end{aligned}
\tag{5.7}
$$

Figure 5.6 shows the the orthogonality function Υ for infinite range $r \in [0, \infty]$ and a finite range $r \in [a, b]$, where the values of a and b that are used to generate the figure are 250 and 1210 m, respectively. These values are used to reflect a practical scenario from radar field data. The figure shows that an infinite range satisfies orthogonality while a finite range does not. Furthermore, there is no set of k values for Equation 5.7 that satisfies the orthogonality. In order to simplify the problem, zero-padding is used to extend the analysis window range to be $r \in [0, b]$. This can be seen in Figure 5.5 where the samples that belong to $r \in [0, a]$ are filled with zeros. The analysis window now takes the shape of a sector instead of a ring sector as shown in Figure 5.5. With the zero-padding, Equation 5.7 reduces to

$$
\Upsilon(k) = \int_0^b J_m(k_0 r) J_m(kr) r dr = \frac{b}{k_0^2 - k^2} \left[k J_m(k_0 b) J_m'(kb) - k_1 J_m(kb) J'(k_0 b)) \right] \tag{5.8}
$$

With the help of Sturm-Liouville(S-L) theory [17] and imposing the zero boundary condition, $J_m(kb) = 0$, the orthogonality in Equation 5.8 is satisfied for a certain set of values, $k = k_{nm}$, with $k_{nm} b$ being the set of zeros of the mth order Bessel function and $n = 1 \ldots N$ is an integer. Using Equation 5.8 and $k_0 = 0.1$ rad/m, Figure 5.7 shows the orthogonality for $r \in [0, b]$. The side lobes that appear in the figure are due to zero padding, which can be visualized as multiplying the radar image by a unit

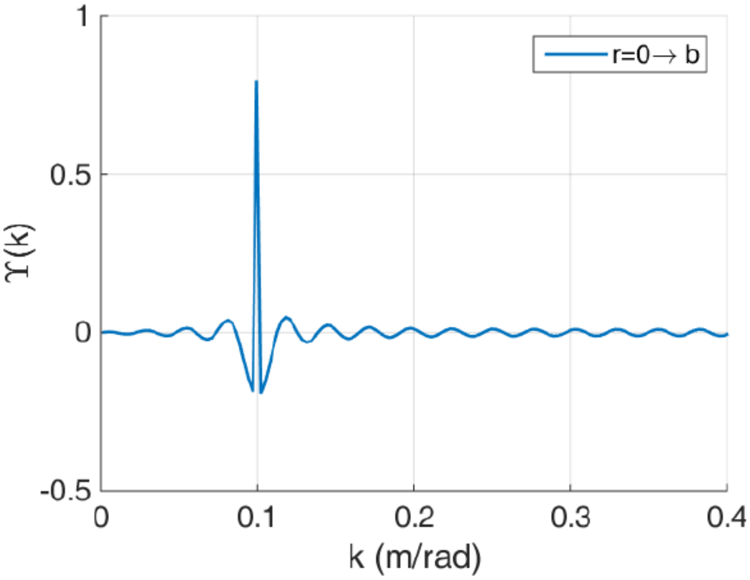

Figure 5.7: Orthogonality of Bessel functions for infinite case presented in Equation 5.8. The values $m = 0, k_0 = .1$ rad/m are used, without loss of generality.

step function in the range dimension. $R(r)$, given in Equation 5.4, is updated such that

$$R_{nm}(r) = \frac{1}{\sqrt{\mathcal{N}_n^{(m)}}} J_m(k_{nm}r),$$

where

$$\mathcal{N}_n^{(m)} = \frac{b^2}{2} J_{m+1}^2(k_{nm}).$$

Hence, the Polar Fourier Transform over a finite region can be given as

$$P(n, m) = \int_0^b \int_0^{2\pi} f(r, \varphi) \Psi_{nm}^*(r, \varphi) r dr d\varphi,$$

where $P(n, m)$ are the PFT coefficients of the B-scan image $f(r, \varphi)$. The B-scan $f(r, \varphi)$ can be reconstructed from $P(n, m)$ as

$$f(r,\varphi) = \sum_{n=1}^{N} \sum_{m=-\Theta/2-1}^{\Theta/2} P(n,m)\Psi_{nm}(r,\varphi),$$

where Θ is the number of directions sampled in one full radar sweep and

$$\Psi_{nm}(r,\varphi) = R_{nm}(r)\Phi_m(\varphi). \tag{5.9}$$

In the CFT method, as explained in Chapter 2, the Fourier transformation is applied in the time domain using the FFT in order to remove the 180° ambiguity in direction that results from the 2-D special Fourier analysis. Similarly, the FFT can be applied to the 2-D PFT output in order to removed the ambiguity in direction. Keep in mind that the scan conversion process is time independent.

5.3.3 Relation to the Cartesian Fourier transform

The 2-D Fourier transform in its vector form is given by

$$F(\mathbf{k}) = \int_{-\infty}^{\infty} f(\mathbf{r})e^{-j\mathbf{k}.\mathbf{r}}d\mathbf{r},$$

In polar coordinates, the transform takes the form

$$F(k,\theta) = \int_0^{\infty}\int_0^{2\pi} f(r,\varphi)e^{-jkr\cos(\theta-\varphi)}rdrd\varphi.$$

Using the identity

$$e^{-jkr\cos(\theta-\varphi)} = \sum_{m=-\infty}^{\infty} j^{-m}J_m(kr)e^{jm\theta}e^{-jm\varphi},$$

$F(k,\theta)$ can be written as

$$F(k,\theta) = \int_0^{\infty}\int_0^{2\pi} f(r,\theta)\sum_{m=-\infty}^{\infty} j^{-m}J_m(kr)e^{jm\theta}e^{-jm\varphi}rdrd\varphi. \tag{5.10}$$

Comparing Equations 5.10 and

$$P(k,m) = \int\limits_0^{\infty}\int\limits_0^{2\pi} f(r,\varphi)\Psi^*_{k,m}(r,\varphi)rdrd\varphi,$$

it can be seen that

$$F(k,\theta) = \sum_{m=-\infty}^{\infty} j^{-m} \frac{1}{\sqrt{2\pi k}} P_{k,m} e^{jm\theta}.$$

Conversely, the polar Fourier transform spectrum is given in terms of the Cartesian Fourier transform spectrum as

$$P(k,m) = \frac{j^m}{\sqrt{2\pi k}} \int_0^{2\pi} F(k,\theta) e^{-jm\theta} d\theta.$$

Clearly $P(k,m)$ are the Fourier coefficients of the Cartesian Fourier spectrum over the azimuth dimension multiplied by the factor $j^m/\sqrt{k}$. For a limited range $r \in [0,b]$, $P(n,m)$ is given in [17] as

$$P(n,m) = (-1)^n j^m \frac{2\sqrt{\pi}}{\sqrt{A}} k_{nm} \sum_{k_0,\theta_0} \frac{J_m(k_0 b)}{k_0^2 - k_{nm}^2} e^{-jm\theta_0} F(k_0,\theta_0),$$

where (k_0,θ_0) are the polar wave number vector components and A is the smallest rectangular area that encloses the ring sector analysis window. Conversely,

$$F(k_0,\theta_0) = \frac{2\sqrt{\pi}}{\sqrt{A}} \sum_{n,m} (-1)^n (-j)^m k_{nm} \frac{J_m(k_0 b)}{k_0^2 - k_{nm}^2} e^{jm\theta_0} P(n,m). \qquad (5.11)$$

Equation 5.11 presents a very important link between output of the PFT and the CFT. Once the the PFT image spectrum is produced, Equation 5.11 is used to convert it to the familiar CFT image spectrum. In Figure 5.2, the conversion using this equation is presented by the 'spectral conversion to CFT' block.

Finally, it should be noted from our discussion in this section that since the PFT is different from the CFT in terms of its basis functions, the way an image is decomposed is also different. The CFT represents an image in terms of its basic plane wave components, while the PFT, with its basis functions given in Equation 5.9, represents the image in terms of cylindrical waves.

5.4 Results and Analysis

In our experiments to validate the performance of the PFT compared to the CFT in wave spectrum estimation, both transforms were applied to field data described in Section 2.4. The CFT method used rectangular analysis windows of size 256×128 samples, which covers an area of 1 843 200 m^2 (1920 × 960 m). On the other hand, the PFT method used ring sector analysis windows of size 320 × 128 samples, which covers an area of 1 849 800 m^2 taking the centre of the ring sector analysis window at $r = 960$ m and an azimuth resolution of 0.36°. The size of the ring sector analysis windows covers roughly the same area as the rectangular analysis windows used in the CFT method.

5.4.1 Field data examples

Examples of estimated wave spectra using the PFT are shown in Figure 5.8. Figure 5.8a illustrates the normalized directional ground truth wave spectrum, which is estimated from TRIAXYS wave buoy data. The spectrum has a main peak at 0.07 Hz and 110° and a secondary peak at 0.14 Hz and 140°, with a 63% relative energy of the main peak energy. The normalized estimated directional wave spectra using the CFT and the PFT are shown in Figures 5.8c and 5.8d, respectively. Normalized non-directional wave spectra using the TRIAXYS wave buoy, the CFT and the PFT are shown in Figure 5.8b. In comparison with the TRIAXYS-estimated wave spectra, the PFT shows a better performance in wave spectra estimation. The PFT spectra show a main peak at 0.07 Hz and 111° compared to 0.075 Hz and 100° for the CFT spectra. Also, the PFT spectra show a secondary peak at 0.13 Hz and 155°, with 35% relative energy, compared to 0.12 Hz and 170°, with 18% relative energy for the CFT spectra.

Another example is shown in Figure 5.9. Figure 5.9a shows the normalized ground truth wave spectrum which is estimated using TRIAXYS wave buoy data. The spectrum has two peaks, a main peak at 0.11 Hz and 190° and a secondary peak at 0.75 Hz and 95°, with a 92% relative energy level. In comparison with the TRIAXYS-estimated wave spectra, again the PFT shows a better wave spectral estimation than the CFT. As shown in Figures 5.9b and 5.9d, the PFT detects both peaks; the main peak at 0.11 Hz and 180° and the secondary peak at 0.08 Hz and 90°, with 97% relative energy level. On the other hand, the CFT detects only the secondary peak at 0.75 Hz and 95° as a false main peak, while the true main peak is not detected (see Figures 5.9b and 5.9c).

5.4.2 Performance validation

In order to validate the performance of the PFT in comparison with the CFT, both methods are used to estimate wave spectra using the X-band marine radar data described in Section 7.3. Furthermore, the ocean wave spectral estimates from both methods are compared to the ground truth estimates there were generated using a TRIAXYS wave rider buoy. The correlation coefficient ρ between the radar-estimated non-directional wave spectra and the non directional buoy spectrum was used as an agreement measure between the two spectra. The value of the correlation coefficient ranges from 0 (no similarity) to 1 (identical) and is given by Equation 3.1. ρ was calculated for different radar estimates using the PFT and CFT. Figure 5.10 shows the correlation coefficient in pairs: the CFT coefficients are marked using "o" while the PFT is marked using "×"; the results are shown for four 12-hour periods during Dec 1 - Dec 4, 2008. To enhance the readability of the results, the PFT output is plotted in blue to indicate improvement in performance (and in red to indicate deterioration) compared to the CFT output. The results show that the PFT outperforms the CFT method with higher correlation coefficients for the majority of time samples. The

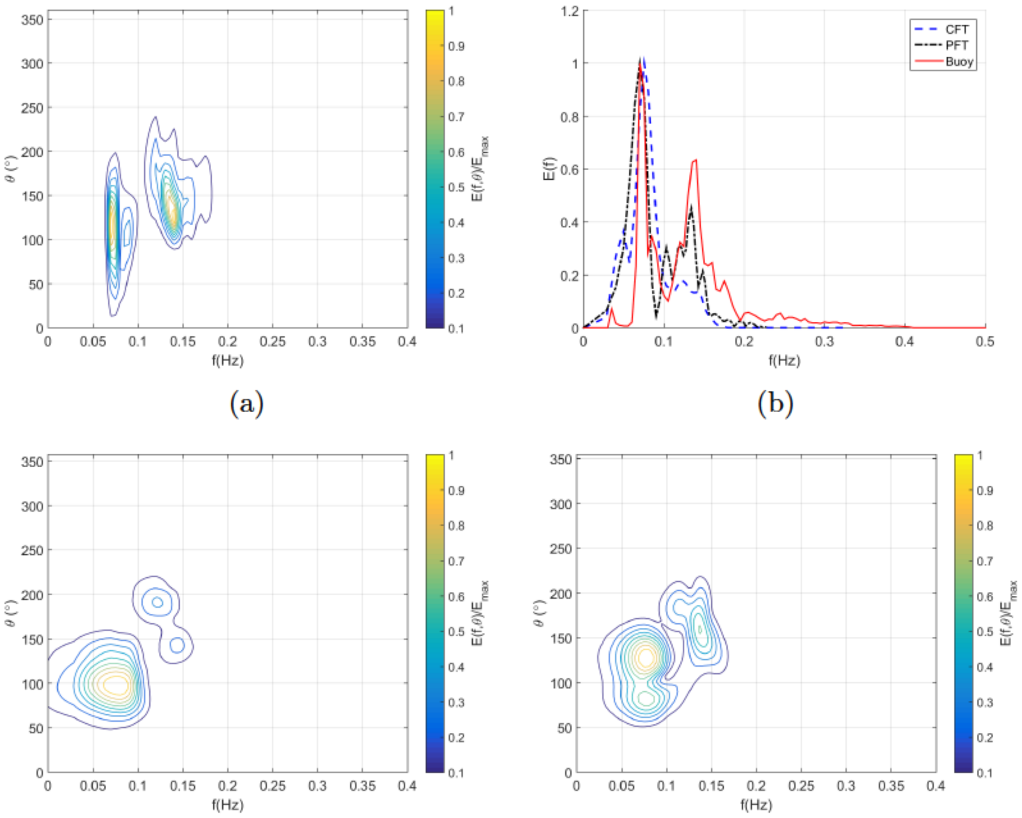

(a) (b)

(c) (d)

Figure 5.8: A field data example for wave spectrum estimation using the PFT. Data were recorded on Dec 1, 2008, between 12:08 PM and 12:38 PM: (a) Directional wave spectrum estimated using a directional TRIAXYS wave rider buoy. (b) Frequency wave spectrum estimated from the radar data using the CFT and PFT overlaid on the ground truth frequency wave spectrum. (c and d) The directional wave spectrum estimated using the CFT and PFT, respectively.

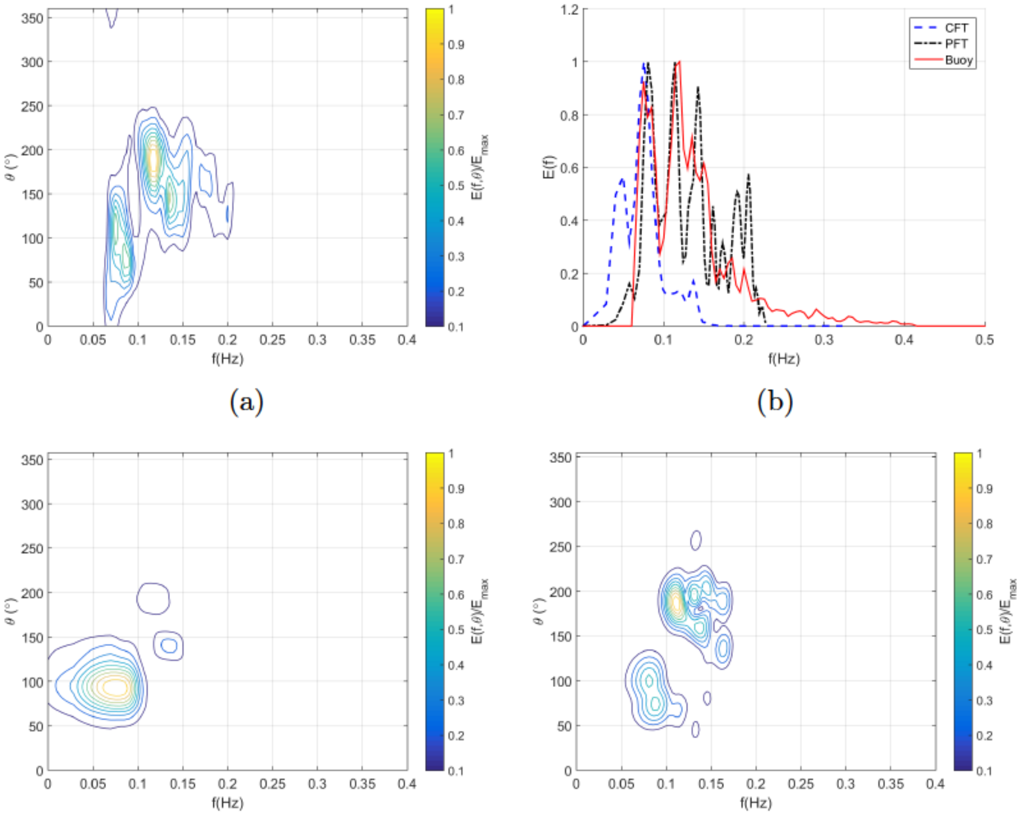

(a) (b)

(c) (d)

Figure 5.9: A field data example for wave spectrum estimation using the PFT. Data were recorded on Dec 1, 2008, between 11:42 AM and 12:12 PM: (a) Directional wave spectrum estimated using a directional TRIAXYS wave rider buoy. (b) Frequency wave spectrum estimated from the radar data using the CFT and PFT overlaid on the ground truth frequency wave spectrum. (c and d) The directional wave spectrum estimated using the CFT and PFT, respectively.

average improvement is found to be 12%.

For further validation, the peak wave period T_p, mean period T_{01}, the zero-crossing period T_z and the peak wave direction θ_p are calculated from the PFT and CFT-estimated spectra (see Section 2.3.2) for wind waves and swell. Figures 5.11 and 5.12 show the peak wave period and direction, respectively. The mean absolute error ($\overline{|\varepsilon_{T_p}|}$,$\overline{|\varepsilon_{T_{01}}|}$, $\overline{|\varepsilon_{T_z}|}$ and $\overline{|\varepsilon_{\theta_p}|}$) and error standard deviation ($\sigma_{\varepsilon_{T_p}}$, $\sigma_{\varepsilon_{T_{01}}}$, $\sigma_{\varepsilon_{T_z}}$ and $\sigma_{\varepsilon_{\theta_p}}$) of these estimates are calculated with respect to the ground truth and are listed in Table 5.1. Figure 5.13 shows the normalized (with respect to the CFT) average absolute error in estimating T_p, T_{01}, T_z, and θ_p using the PFT. The mean absolute error and the error standard deviation of T_p are given by Equations 3.2 and 3.3, respectively. The other metrics are calculated in a similar manner. As derived from Table 5.1, the PFT-wave period and direction estimates are 54% and 49%, respectively, more accurate than the CFT-estimates. The standard deviation values are calculated and listed in Table 5.1 in order to provide better understanding of the distribution of estimates.

While it appears that the PFT method may offer some advantage over the traditional CFT method, the CFT has the advantage of shorter computational time over the PFT. This is due to the Fast Fourier Transform algorithm which is used to evaluate the CFT. As yet, there is no such fast algorithm for the PFT. In our analysis and implementation, the CFT needed 2.7 s to process one radar set (32 radar images) while the PFT required 4.3 min to process the same set, with both implementations running on the same processor and with similar software and data structure efficiency. However, the PFT method computational time might be improved by using a faster processor and utilizing parallel computation. If the goal of using the PFT for real-time analysis is to be realized, it will be important to reduce the computational time to below 48 s, which is the time needed for the radars used in this experiment to

Table 5.1: Comparison of the PFT and the CFT in wave period and peak direction estimation.

	$\overline{\lvert\varepsilon_{T_p}\rvert}$(s)	$\sigma_{\varepsilon_{T_p}}$ (s)	$\overline{\lvert\varepsilon_{T_{01}}\rvert}$(s)	$\sigma_{\varepsilon_{T_{01}}}$ (s)	$\overline{\lvert\varepsilon_{T_z}\rvert}$(s)	$\sigma_{\varepsilon_{T_z}}$ (s)	$\overline{\lvert\varepsilon_{\theta_p}\rvert}$(°)	$\sigma_{\varepsilon_{\theta_p}}$ (°)
CFT	2.5	0.9	2.4	0.8	2.3	0.8	15.1	16.1
PFT	1.4	0.6	1.1	0.7	1.1	0.7	7.7	6.8

generate one radar image set.

In the next chapter, further validation analysis of the PFT performance is conducted in comparison with the ARPM and the ISAF methods that are individually proposed in Chapter 3 and 4, respectively. Also the performance of the proposed methods is analyzed when they are combined.

5.5 Conclusions

Scan conversion is a process of non-uniform re-sampling which leads to some distortion in the wave spectra estimated using marine radar. In this chapter, it is proposed to eliminate the scan conversion process and to apply Fourier transformation directly on the radar data in their native polar B-scan format. The Polar Fourier Transform (PFT) that satisfies orthogonality in the polar coordinates was adopted in this chapter and integrated into an overall wave spectral estimation method. The PFT decomposes an image into its basic components of cylindrical waves, rather than plane waves as in the CFT. Using the PFT requires the analysis windows to have the shape of ring sectors instead of rectangular windows. There is an inherent advantage to this shape of window, namely the compatibility with the original B-scan image layout. This allows for more availability of samples for use in the analysis. Results show that using the PFT instead of the CFT improves the performance of the radar-based method in estimating the ocean wave spectra. This was shown by comparing the wave spectra estimates from CFT and PFT with ground truth spectra that were acquired from TRIAXYS wave buoy data. It also was shown that the PFT produces more accurate estimates of sea state parameters such as wave period and direction. The PFT algorithm significantly serves the purpose of this thesis of reducing the error in wave spectra estimation.

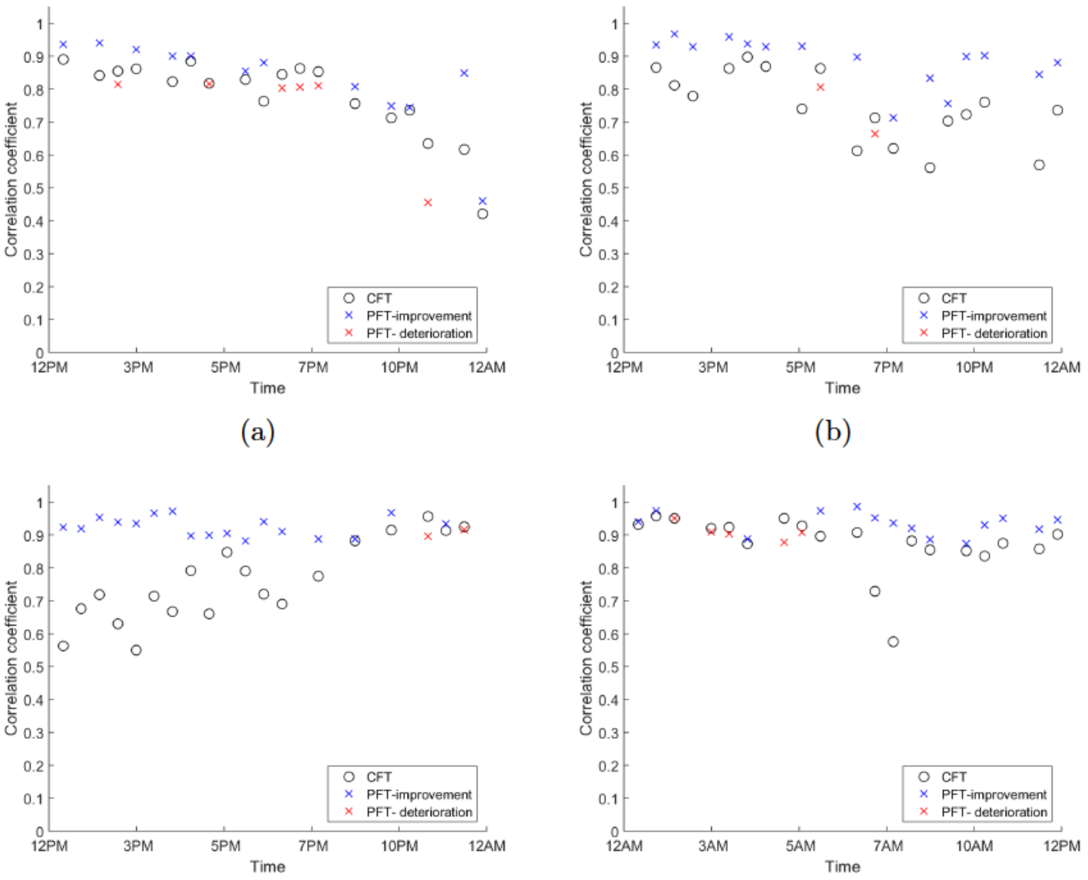

(a) (b)

(c) (d)

Figure 5.10: A comparison between the PFT and the CFT in terms of the frequency wave spectrum similarity, with respect to the buoy ground truth spectra. Each point represents the correlation coefficient between ground truth and the radar data 30 minute averaged frequency wave spectra. (a) Dec 1 afternoon and evening, (b) Dec 2 afternoon and evening, (c) Dec 3 afternoon and evening, (d) Dec 4 morning.

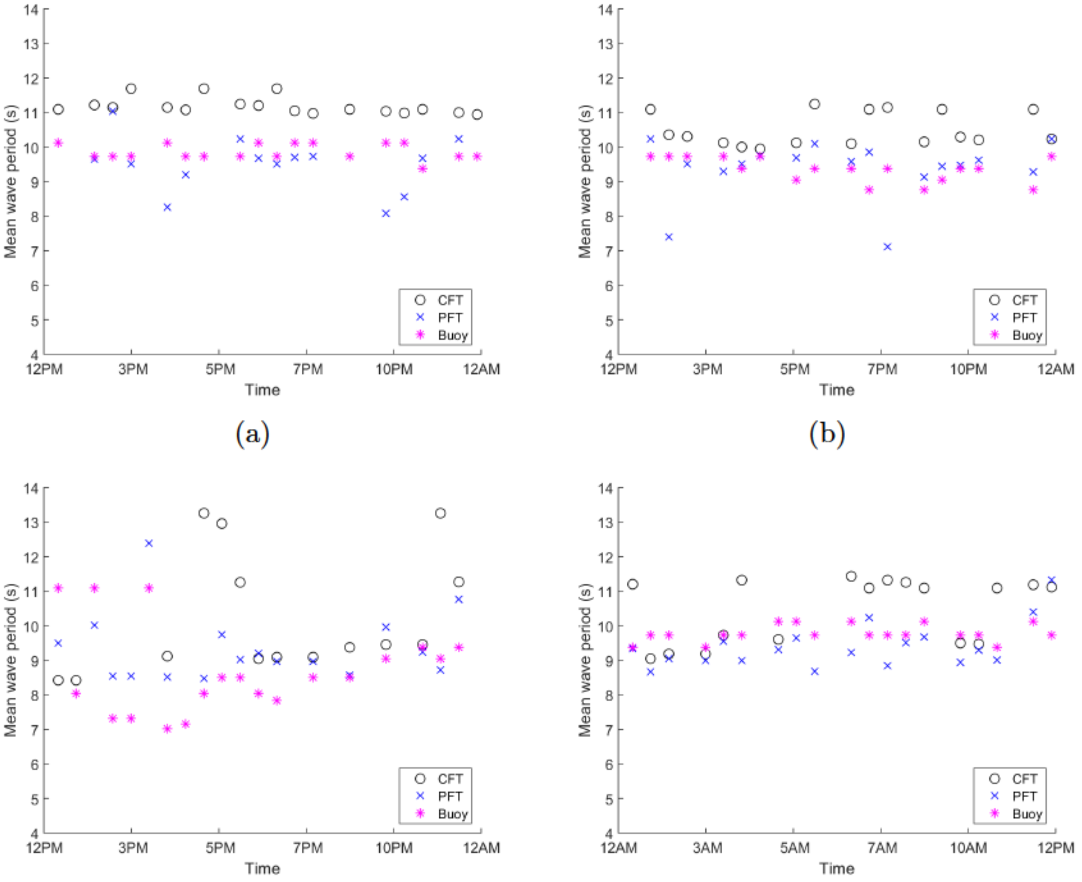

(a) (b)

(c) (d)

Figure 5.11: A comparison between the PFT and the CFT in terms of the peak wave period. (a) Dec 1 afternoon and evening, (b) Dec 2 afternoon and evening, (c) Dec 3 afternoon and evening, (d) Dec 4 morning.

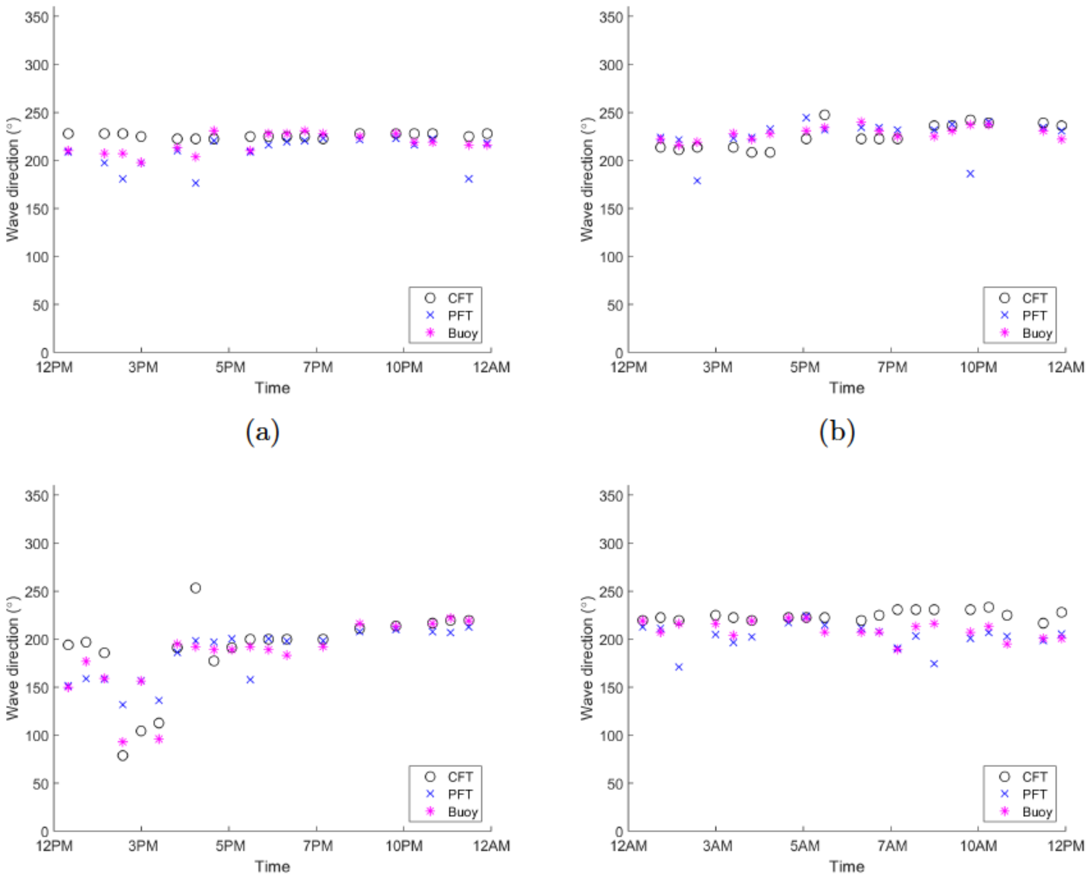

(a)

(b)

(c)

(d)

Figure 5.12: A comparison between the CFT and the PFT in terms of the peak wave direction. (a) Dec 1 afternoon and evening, (b) Dec 2 afternoon and evening, (c) Dec 3 afternoon and evening, (d) Dec 4 morning.

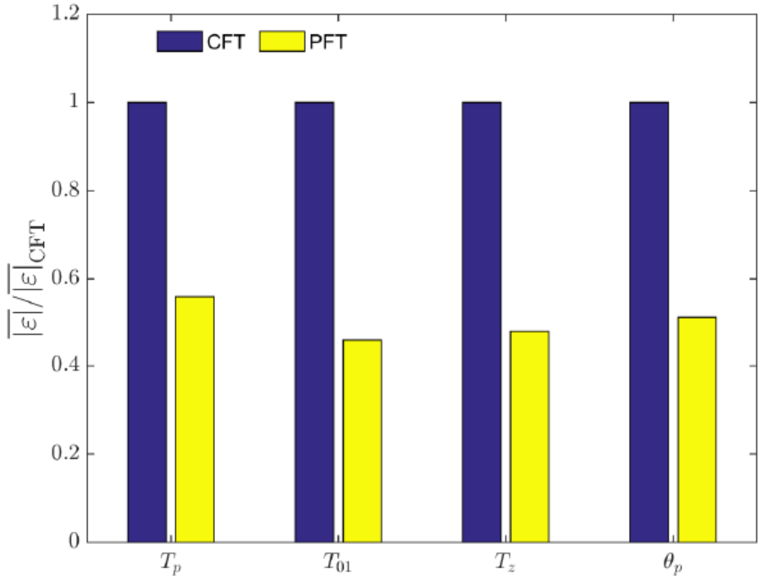

Figure 5.13: The average absolute error of the PFT normalized with respect to the CFT method.

Chapter 6

Performance comparison of the ARPM, ISAF, and PFT

6.1 Introduction

In Chapters 3, 4, and 5 respectively, the ARPM, ISAF, and the PFT have been proposed for enhancing ocean wave spectral estimation using X-band marine radar. It has been shown that the methods, individually, produce more accurate estimates of ocean wave spectra and of wave period and direction compared to the standard CFT method, which has been reviewed in Chapter 2. However, the improvement levels varied among the methods. In this chapter, a performance comparison analysis of the three methods is presented. Furthermore, this chapter also explores and validates the performance of the methods when implemented together. For example, the performance of the PFT in estimating the ocean wave spectra is explored when implemented with the ARPM or with the ISAF.

6.2 Design of combined methods

The CFT or the PFT can be implemented with the ARPM, ISAF, or both. Figure 6.1 shows the flow chart of the combining procedure of the CFT, PFT, ARPM, and the ISAF. Eight possible combinations include:

1. **The CFT alone**

   This method represents the standard CFT method reviewed in Chapter 2 and highlighted by the blue box in Figure 6.1. The scan conversion process is used to convert the B-scan images to produce Cartesian images. Subsequently, three uniformly distributed rectangular analysis windows are selected. The CFT method is applied on the selected analysis windows to produce the final estimate of the directional wave spectrum.

2. **The CFT with ARPM**

   This combination is proposed in Chapter 3 and highlighted by the blue and red boxes in Figure 6.1. Once the directional wave spectrum is estimated using the CFT method, new rectangular analysis windows are chosen. The number and direction of the new analysis windows are determined based on the number and direction of the peaks in the estimated directional wave spectrum. The analysis window re-selection process is repeated until the ARPM termination condition is satisfied. Without loss of generality, the termination condition used here is to reach a maximum number of three iterations.

3. **The CFT with ISAF**

   This method is proposed in Chapter 4 and highlighted by the blue and yellow boxes in Figure 6.1. The final estimate of the directional wave spectrum using this method is generated by applying the ISAF modulation transfer function to the CFT-estimated directional wave spectrum in order to mitigate the effect of the ocean surface sampling process.

4. **The CFT with ARPM and ISAF**

   The blue, yellow and red boxes in Figure 6.1 highlight this combination, in which the CFT-estimated directional wave spectrum is corrected using the ISAF modulation transfer function. Subsequently, new rectangular analysis windows are re-selected by the ARPM iterative process to produce the final directional wave spectrum estimate.

5. **The PFT alone**

   This method is proposed in Chapter 5 and highlighted by the green box in Figure 6.1. Two main differences between the CFT and the PFT methods are shown in Figure 6.1. First, unlike the CFT method, the PFT method does not require the intermediate stage of scan conversion. Second, the PFT uses ring sector analysis windows compared to rectangular windows used by the CFT method. The PFT is applied on three uniformly distributed ring sector analysis windows to produce the final estimate of the directional wave spectrum

6. **The PFT with ARPM**

   The green and red boxes in Figure 6.1 highlight this combination. The number and direction of peaks in the PFT-estimated directional wave spectrum are used to determine the number and direction of the new ring sector analysis windows. The PFT is used again to estimate the directional wave spectrum from the new analysis windows. This process is repeated recursively until the termination condition of a maximum of three iterations is satisfied.

7. **The PFT with ISAF**

   As highlighted by the green and yellow boxes in Figure 6.1 for this combination, the PFT-estimated directional wave spectrum is corrected using the ISAF modulation transfer function to produce the final directional wave spectrum.

8. **The PFT with ARPM and ISAF**

   This combination is highlighted in Figure 6.1 by the green, yellow, and red boxes. Once the PFT-estimate of the directional wave spectrum is generated, it is corrected by the ISAF modulation transfer function. Subsequently, new ring sector analysis windows are re-selected using the ARPM iterative algorithm. The final estimate of the directional wave spectrum is produced once the ARPM termination condition of a maximum of three iterations is satisfied.

The performance of estimating the ocean wave spectra and the wave period and directions of the CFT with the ARPM, the CFT with the ISAF, and the PFT alone were presented in Chapters 3, 4, and 5, respectively. The performance analysis of the remaining combinations outlined in Section 6.2 in estimating the ocean wave spectra and the wave period and direction is presented in Section 6.3. Using a performance validation approach that is similar to that used in the previous chapters, estimates of the ocean wave spectra and wave period and direction produced by the different combinations are compared to ground truth estimates generated using a TRIAXYS wave rider buoy (as discussed in Section 2.4).

6.3 Results and Analysis

The various combinations of the CFT, ARPM, ISAF, and PFT presented in Section 6.2 are used to estimate ocean wave spectra from the field data described in Section 2.4. Subsequently, the peak wave period T_p, mean period T_{01}, the zero-crossing period T_z and the peak wave direction θ_p are calculated from the estimated wave spectra as described in Section 2.3.2. For comparison, the mean absolute error ($\overline{|\varepsilon_{T_p}|}$,$\overline{|\varepsilon_{T_{01}}|}$, $\overline{|\varepsilon_{T_z}|}$ and $\overline{|\varepsilon_{\theta_p}|}$) and error standard deviation ($\sigma_{\varepsilon_{T_p}}$, $\sigma_{\varepsilon_{T_{01}}}$, $\sigma_{\varepsilon_{T_z}}$ and $\sigma_{\varepsilon_{\theta_p}}$) of these estimates

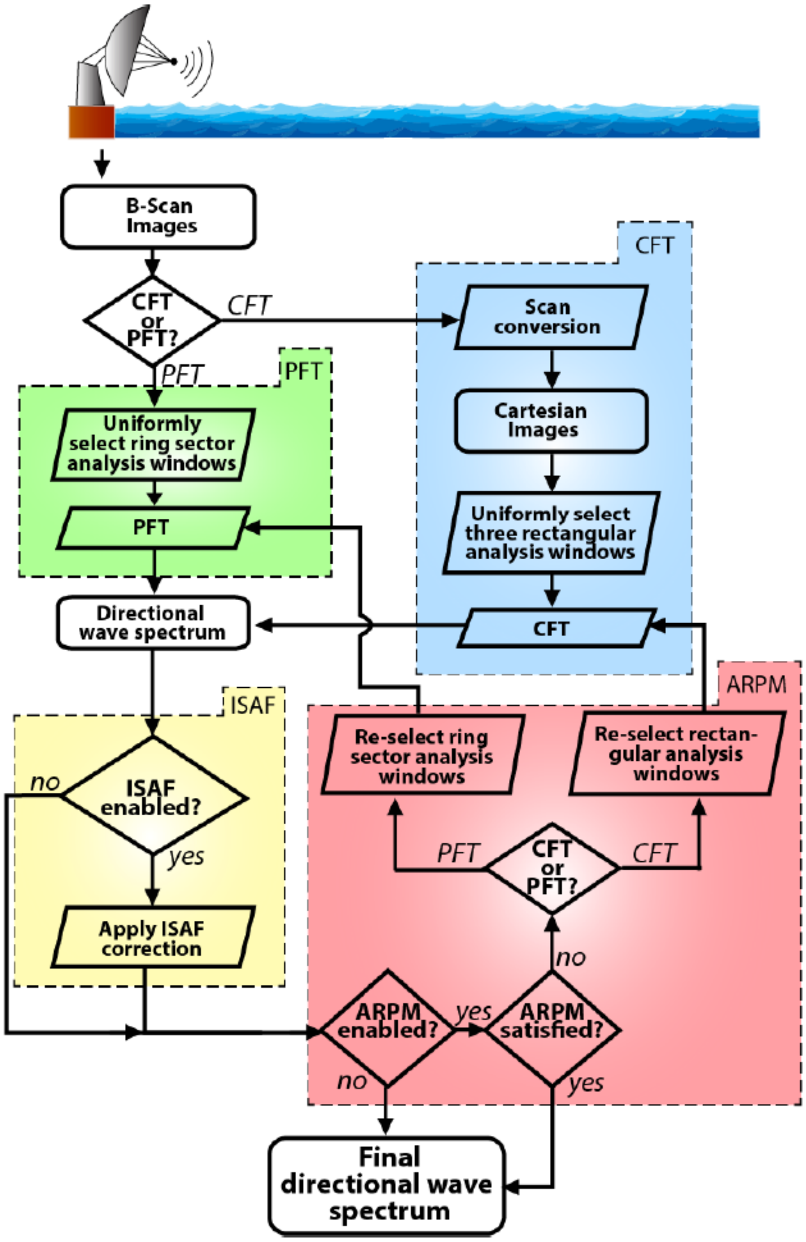

Figure 6.1: Flow chart of the directional wave spectrum estimation using the PFT, ARPM and ISAF. The blue, green, yellow, and red boxes highlight the standard CFT, the PFT, the ISAF and the ARPM methods, respectively.

are calculated with respect to the ground truth. Experimental results are listed in Table 6.1. Figure 6.2 shows the normalized (with respect to the CFT) average absolute error in estimating T_p, T_{01}, T_z, and θ_p using the proposed methods. The mean absolute error and the error standard deviation of T_p are given by Equations 3.2 and 3.3, respectively. The other metrics are calculated in a similar manner. Also, Table 6.2 lists the relative improvements presented by the proposed methods and their combinations in comparison with the standard CFT method. The following remarks can be noted from Tables 6.1 and 6.2:

- All the proposed methods (the ARPM, ISAF, and PFT) individually and their combinations have improved the estimation accuracy of the wave period and wave direction compared to the standard CFT method.

- Between the APRM and the ISAF when implemented with the CFT, the ARPM showed a better performance in estimating T_p with 20% improvement compared to 12% using the ISAF. However, the ISAF improved the wave direction estimation by 33% compared to 22% using the ARPM. In terms of T_{01} and T_z, both methods showed a similar performance with an improvement of 20%.

- When implementing the CFT with ARPM and ISAF, the combination outperforms the performance of the CFT with ARPM and the CFT with ISAF in terms of wave period estimation with improvements of 32%, 38%, and 38% in estimating T_p, T_{01}, and T_z, respectively. On the other hand, the combination outperforms the CFT with ARPM but not the CFT with ISAF in terms of estimating θ_p with an improvement of 23%.

- The PFT outperforms the standard CFT, the CFT with ARPM, the CFT with ISAF, and the CFT with ARPM and ISAF. The PFT produced 44% , 54%, 52%, and 49% improvement in the estimation of T_p, T_1, T_z, and θ_p, respectively.

However, as mentioned in Section 5.4.2, the PFT is computationally expensive which might limit its implementation to non-real time applications.

- Using the PFT with ARPM produces improvements of 60%, 46%, 46%, and 33% in the estimation of T_p, T_1, T_z, and θ_p, respectively. Interestingly, the PFT method produces more accurate wave direction estimates than the PFT when combined with the ARPM. Further investigation on the reason behind this behavior is to be addressed in future work.
- When using the PFT with ISAF, improvements of 52%, 66%, 66%, and 55% in the estimation of T_p, T_1, T_z, and θ_p, respectively, are achieved. It must be noted that this combination has produced the most accurate estimates of T_{01}, T_z, and θ_p among all the methods and their combinations.
- When implementing the PFT with ARPM and ISAF, the estimation of T_p, T_1, T_z, and θ_p have improved by 72%, 63%, 63%, and 33%, respectively. Also, the most accurate estimates of T_p were produced using this combination.

In order to further demonstrate the performance of the proposed methods and their combinations, two field data examples of ocean wave spectral estimation are presented. Figure 6.3 shows (a) a ground-truth directional wave spectrum estimated from TRIAXYS Wave Rider buoy data, (b-e) the estimated non-directional wave spectrum using the proposed methods and their combinations, and (f-m) the estimated directional wave spectrum using the proposed methods and their combinations. With a similar terminology to that used in Chapters 3, 4, and 5, the peak with highest energy is referred to as the main peak, while the other peaks are referred to as the secondary peaks. Also, since we are dealing with normalized wave spectra, the energy level of the secondary peaks is measured relatively with respect to the energy level of the main peak in the same spectrum.

Figures 6.3a and 6.3b show that the ground truth wave spectra have a main peak at 0.115 Hz and 200° and a secondary peak at 0.075 Hz and 95° with a relative energy level of 73%. Looking at the estimates of the non-directional and directional wave spectrum that were generated using the standard CFT method shown in Figures 6.3b and 6.3f, respectively, the secondary peak was detected as a main peak at 0.08 Hz and 115° while the main peak was not detected. Using the CFT with ARPM, as depicted in Figures 6.3c and 6.3g, the main peak is now more visible but still detected as a secondary peak with a relative energy level of 25%. It is expected that the CFT with ARPM would have performed even better if both peaks were detected in the CFT-estimated directional wave spectrum of Figure 6.3f which is used as the initial guess for the ARPM recursive algorithm. Implementing the CFT with ISAF improves the estimates of the non-directional and directional wave spectra as displayed in Figures 6.3d and 6.3h. The main peak was still detected as a secondary peak with a relative energy of 35%. Using the CFT with ARPM and ISAF introduces further enhancement in detecting the main peak. However, the main peak is still detected as secondary a peak with a relative energy level of 40%.

Figures 6.3b and 6.3j show the PFT-estimates of the non-directional and directional wave spectra, respectively. The main peak was detected as a secondary peak with a relative energy level of 65% , the PFT outperformed the CFT, the CFT with ARPM, the CFT with ISAF, and the CFT with ARPM and ISAF. Further significant enhancement was observed when the PFT with ARPM was used as shown in Figures 6.3c and 6.3k. Even though the main peak was still detected as a secondary peak, the estimation of its relative energy was significantly improved as it was estimated to be 95%. The peaks were finally properly detected in this example when the PFT with ISAF was implemented. Figures 6.3d and 6.3l show that the main peak was detected as a main peak and the secondary peak, which has a relative energy of 73%

was detected as a secondary peak with a relative energy of 85%. The estimates of the last combination used here, which is the PFT with ARPM and ISAF, are presented in Figures 6.3e and 6.3m. Again, both peaks were properly detected and the second peak was detected with a relative energy of 65%.

As a conclusion, this example shows that the PFT with ISAF and the PFT with ARPM and ISAF produce the most accurate ocean wave spectral estimation.

In the field example shown in Figure 6.4, the directional ground truth spectrum depicted in Figure 6.4a contains a main peak at 0.12 Hz and 225° and a secondary peak at 0.115 Hz and 100°. Throughout the Figures 6.4(b-e) and (f-m), the estimates of the non-directional and directional wave spectrum, respectively, using the various proposed methods and their combinations are displayed. Due to the close frequencies of the two peaks, the two peaks are hardly distinguishable from each other in the non-directional spectrum shown in Figure 6.4b. Therefore, the comparison between the spectral estimates based on peaks energy is not possible. However, it is clear from Figures 6.4e and 6.4m of the non-directional and directional wave spectra, respectively, generated using the PFT with ARPM and ISAF method that among the various spectrum estimates, the estimates generated using the PFT with ARPM and ISAF method agree the most with the ground truth spectra.

The ARPM, ISAF, and PFT are concerned with improving sea state parameters that are derived from ocean wave spectra including wave period and direction. Hence, the approach followed in designing the previous methods was to improve ocean wave spectral estimation in order to produce accurate sea state parameters. However, the next chapter of this thesis which is concerned with the velocity of encounter information, has a slightly different approach. The velocity of encounter information is estimated from the image spectrum rather than the directional or non-directional wave spectra. Therefore, directional and non-directional wave spectral analysis may not be relevant for estimating the velocity of encounter. However, it must be remembered from Section 2.3.2 that improving velocity of encounter estimation will indirectly improve the estimation of wave spectra since the velocity of encounter information plays a key role in excluding the non-wave components from the image spectrum in the CTF method.

6.4 Conclusions

From the previous discussion in Section 6.3 we conclude that combining the proposed methods can significantly improve the wave period and direction estimation. The most accurate estimates of T_p were achieved when the PFT with ARPM and ISAF method was used. However, using the PFT with ISAF produced the most accurate estimates of T_1, T_z, and θ_p.

Table 6.1: Comparison of the ARPM, ISAF, PFT and their combinations and the standard CFT method in wave period and direction estimation.

	$\overline{\lvert\varepsilon_{T_p}\rvert}$(s)	$\sigma_{\varepsilon_{T_p}}$ (s)	$\overline{\lvert\varepsilon_{T_{01}}\rvert}$(s)	$\sigma_{\varepsilon_{T_{01}}}$ (s)	$\overline{\lvert\varepsilon_{T_z}\rvert}$(s)	$\sigma_{\varepsilon_{T_z}}$(s)	$\overline{\lvert\varepsilon_{\theta_p}\rvert}$(°)	$\sigma_{\varepsilon_{\theta_p}}$(°)
CFT alone	2.5	0.9	2.4	0.8	2.3	0.8	15.1	16.1
CFT with ARPM	2	0.9	1.9	1.5	1.9	1.5	11.7	13
CFT with ISAF	2.2	0.5	1.9	0.5	1.9	0.5	9.9	6
CFT with ARPM and ISAF	1.7	1	1.5	1.1	1.4	1	11.6	13
PFT alone	1.4	0.6	1.1	0.7	1.1	0.7	7.7	6.8
PFT with ARPM	1	0.7	1.3	1	1.2	0.9	9.9	12
PFT with ISAF	1.2	1.2	0.8	1	0.8	1	6.8	8.1
PFT with ARPM and ISAF	0.7	1	0.9	1.2	0.9	1.1	10	12.4

Table 6.2: Relative estimation improvements of T_p, T_{01}, T_z, and θ_p using the ARPM, ISAF, PFT and their combinations compared to the standard CFT method.

	T_p	T_{01}	T_z	θ_p
CFT with ARPM	20%	21%	17%	23%
CFT with ISAF	12%	21%	17%	34%
CFT with ARPM and ISAF	32%	38%	39%	23%
PFT alone	44%	54%	52%	49%
PFT with ARPM	60%	46%	48%	34%
PFT with ISAF	52%	**67%**	**65%**	**56%**
PFT with ARPM and ISAF	**72%**	63%	61%	37%

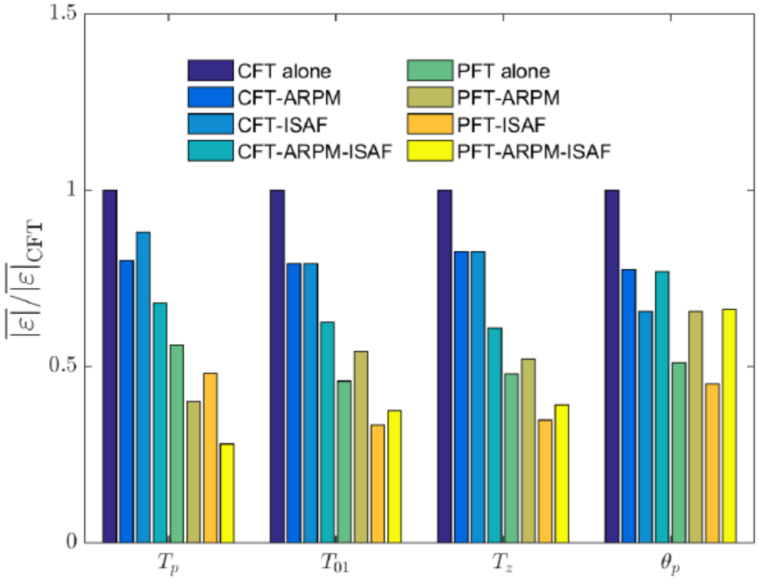

Figure 6.2: The average absolute error of the proposed methods normalized with respect to the CFT method.

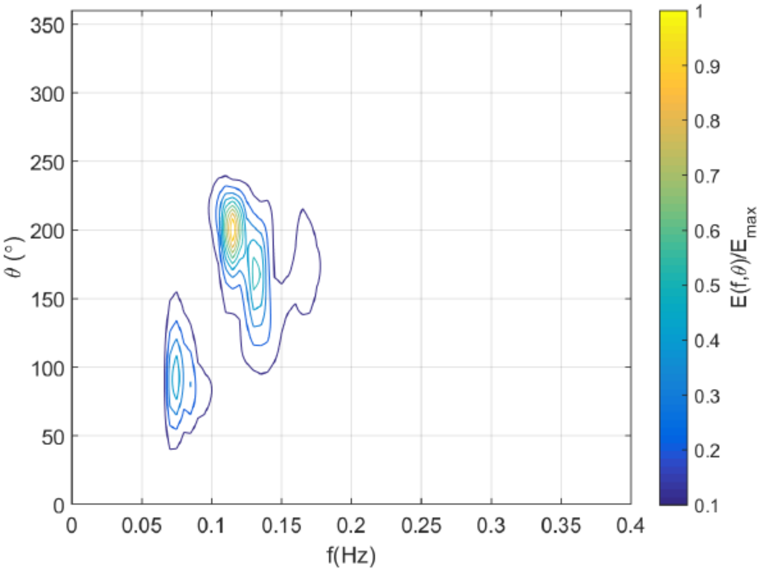

(a)

Figure 6.3: A field data example for wave spectrum estimation using the CFT, PFT, ARPM, and ISAF. Data were recorded on Dec 1, 2008 between 4:40PM and 5:10 PM: (a) Directional wave spectrum estimated using a directional TRIAXYS wave rider buoy. *Cont.*

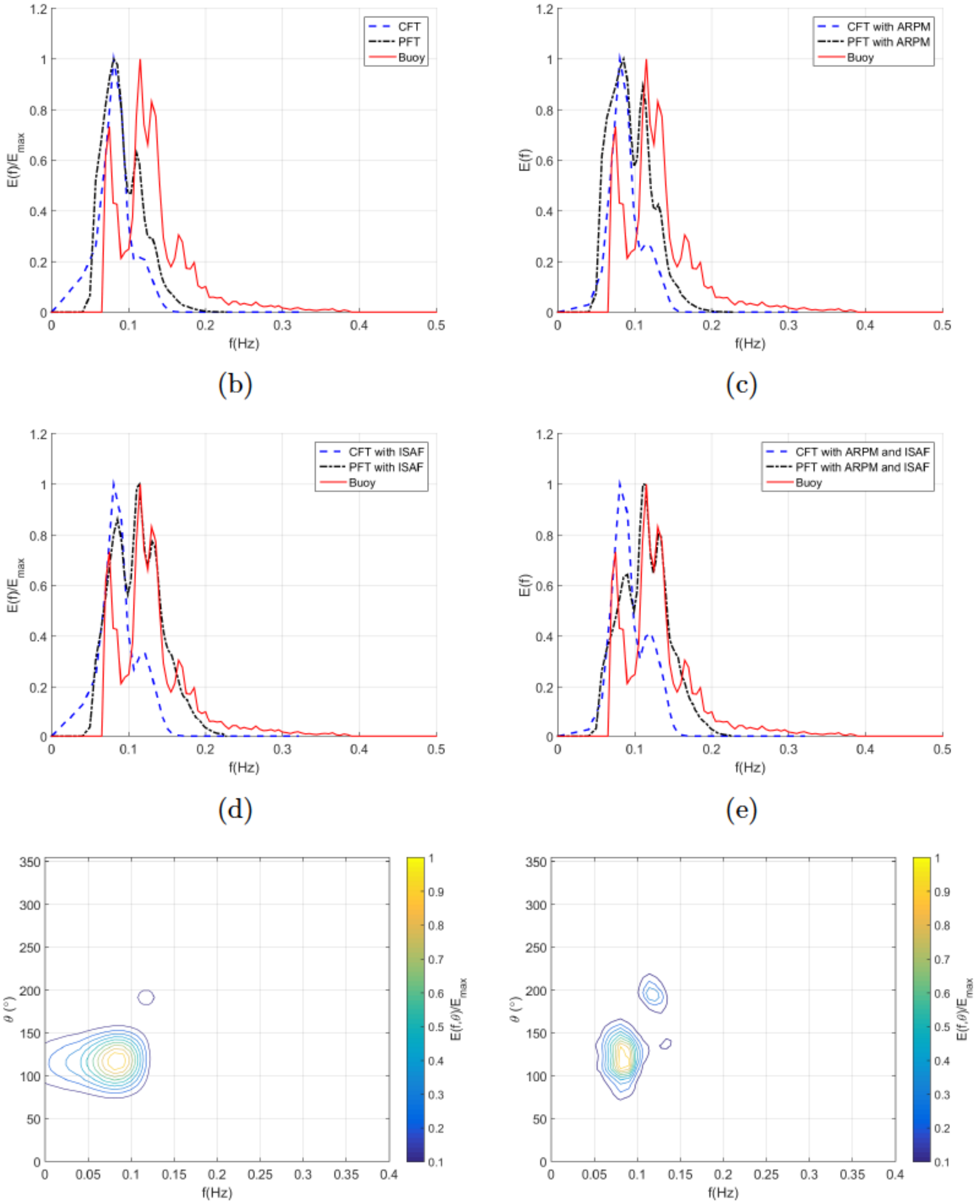

(b) (c)

(d) (e)

(f) CFT (g) CFT with ARPM

Figure 6.3: (b-e) Frequency wave spectrum estimated from the radar data using the CFT, PFT, ARPM, ISAF, and their combinations overlaid on the ground truth frequency wave spectrum.(f and g) The directional wave spectrum estimated using the CFT and the CFT with ARPM, respectively. *Cont.*

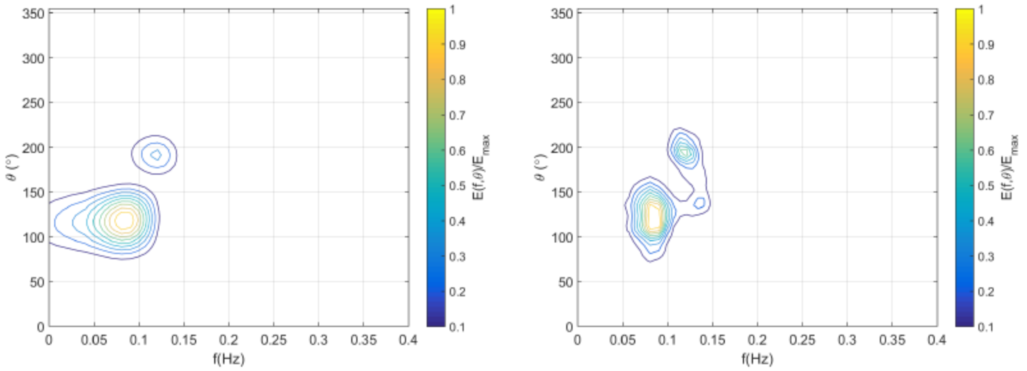

(h) CFT with ISAF (i) CFT with ARPM and ISAF

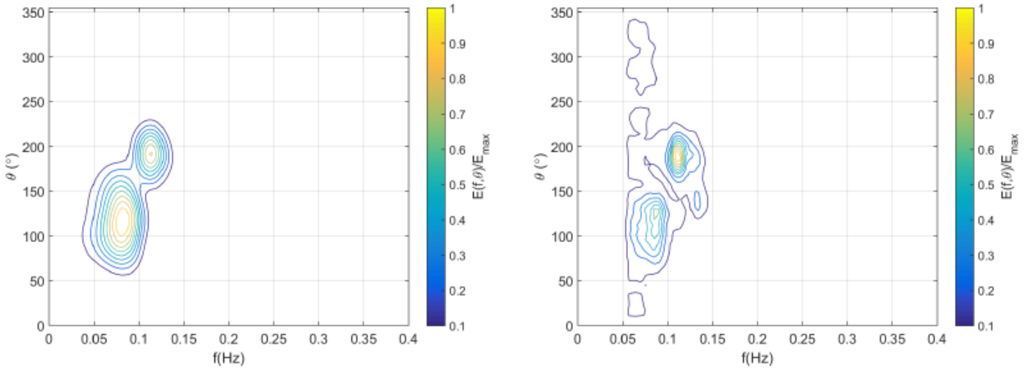

(j) PFT (k) PFT with ARPM

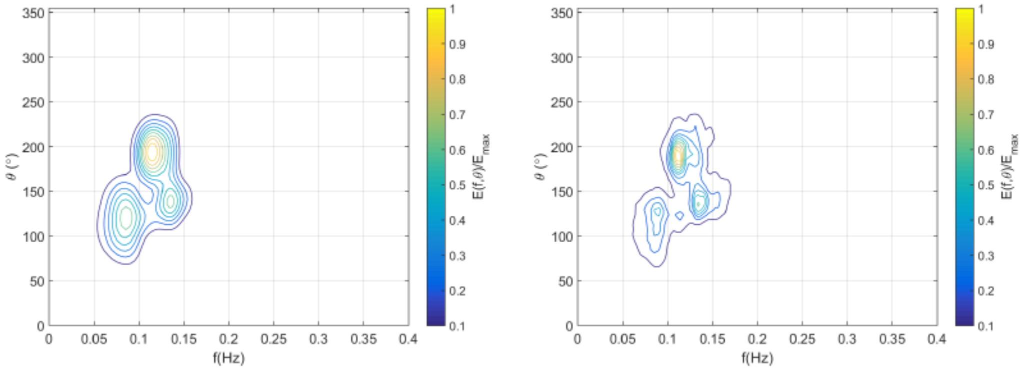

(l) PFT with ISAF (m) PFT with ARPM and ISAF

Figure 6.3: (h,i,j,k,l, and m) The directional wave spectrum estimated using the CFT with ISAF, the CFT with ARPM and ISAF, the PFT, the PFT with ARPM, the PFT with ISAF, and the PFT with ARPM and ISAF, respectively.

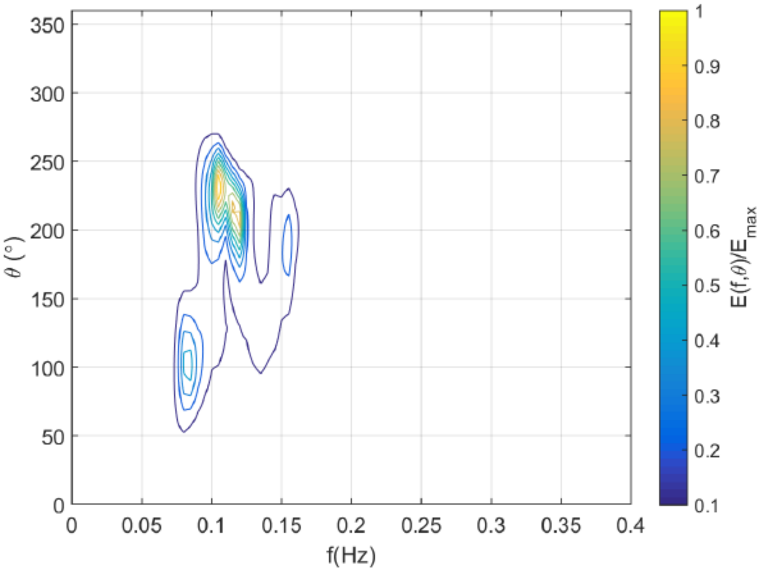

(a)

Figure 6.4: A field data example for wave spectrum estimation using the CFT, PFT, ARPM, and ISAF. Data were recorded on Dec 1, 2008 between 8:40 PM and 9:10 PM: (a) Directional wave spectrum estimated using a directional TRIAXYS wave rider buoy. *Cont.*

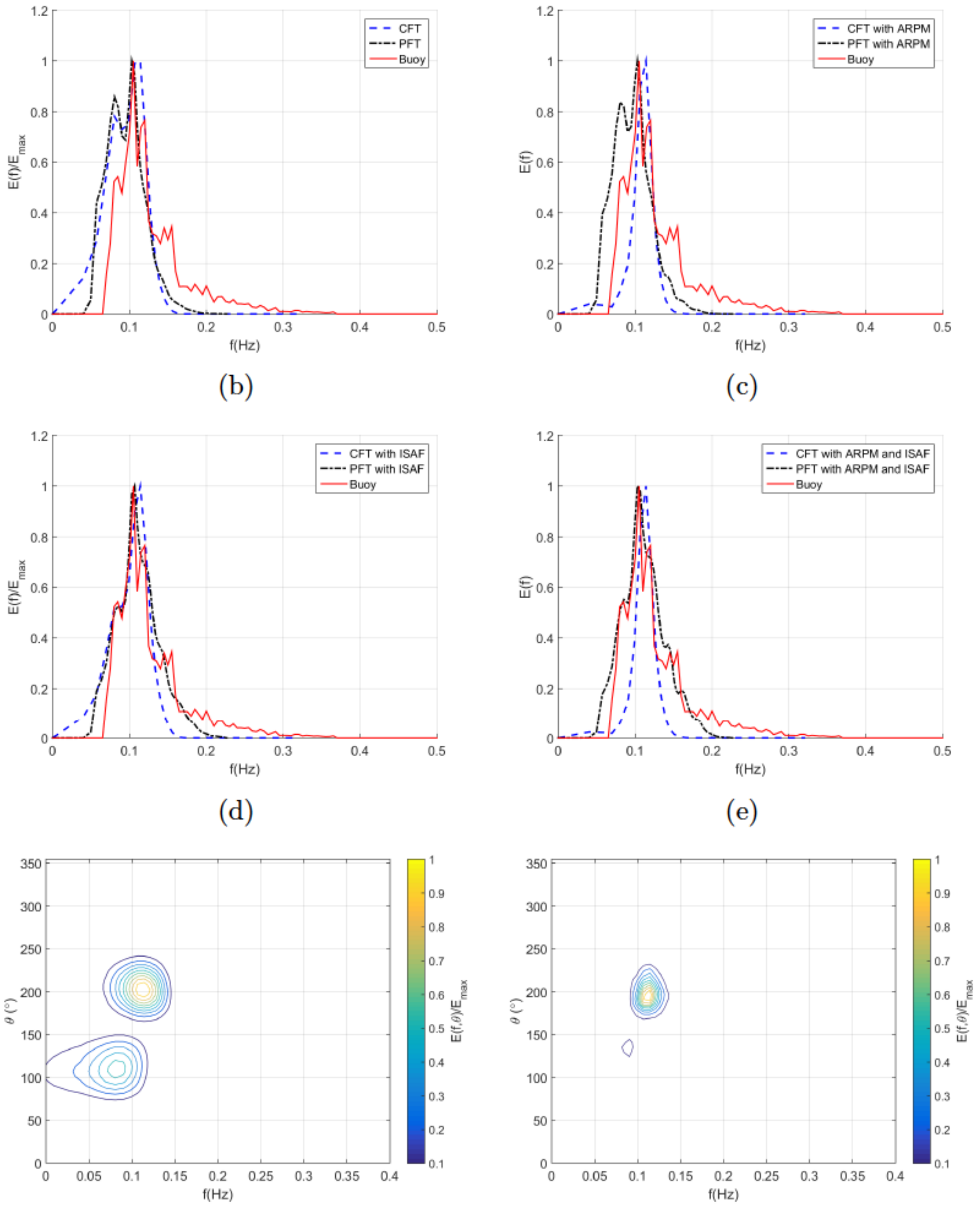

(b) (c)

(d) (e)

(f) CFT (g) CFT with ARPM

Figure 6.4: (b-e) Frequency wave spectrum estimated from the radar data using the CFT, PFT, ARPM, ISAF, and their combinations overlaid on the ground truth frequency wave spectrum.(f and g) The directional wave spectrum estimated using the CFT and the CFT with ARPM, respectively. *Cont.*

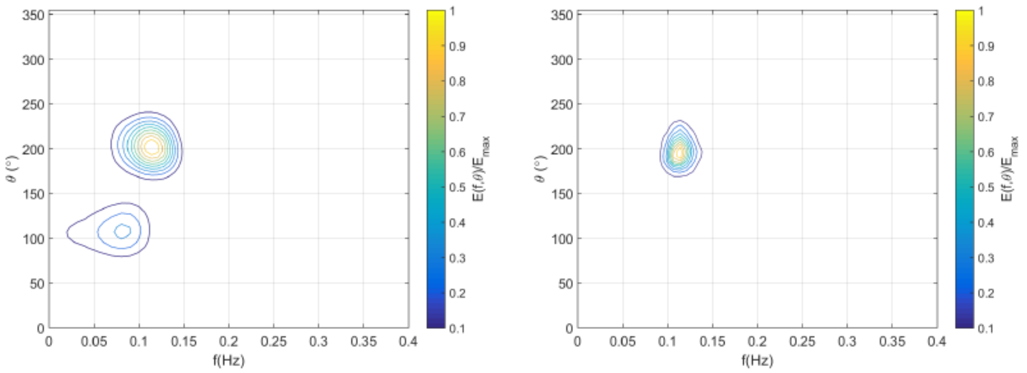

(h) CFT with ISAF (i) CFT with ARPM and ISAF

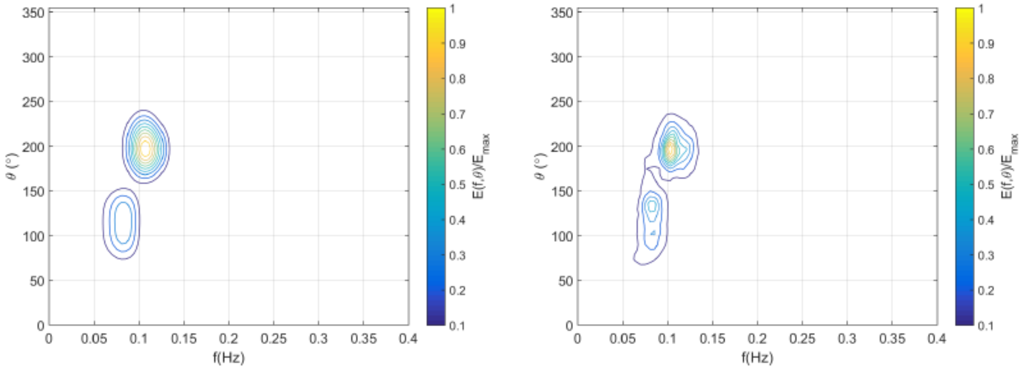

(j) PFT (k) PFT with ARPM

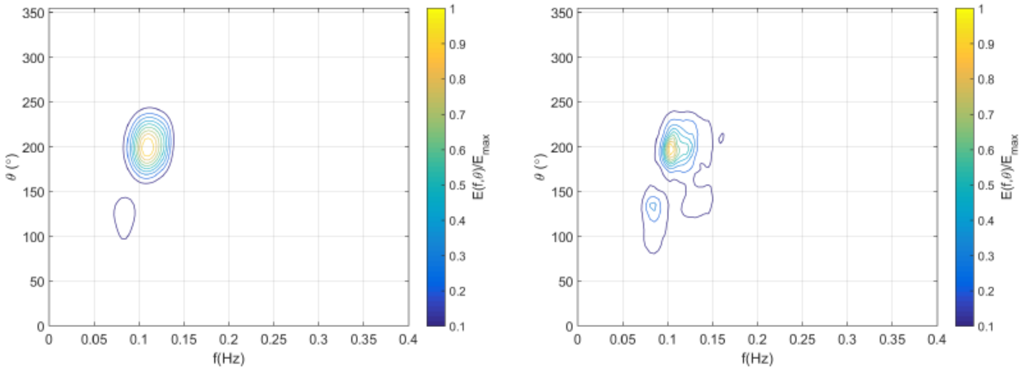

(l) PFT with ISAF (m) CFT with ARPM and ISAF

Figure 6.4: (h,i,j,k,l, and m) The directional wave spectrum estimated using the CFT with ISAF, the CFT with ARPM and ISAF, the PFT, the PFT with ARPM, the PFT with ISAF, and the PFT with ARPM and ISAF, respectively.

Chapter 7

A hybrid method for velocity of encounter estimation using X-band nautical radar

7.1 Introduction

The final enhancement on the wave spectra estimation using X-band marine radar that is considered in this thesis is to develop an accurate (produces low estimation error) and reliable (converges to the true value) method of estimating the velocity of encounter. The velocity of encounter is defined as the vector summation of surface current velocity and ship velocity, which are both measured with respect to the same reference. In the CFT method of estimating ocean wave spectra, as discussed in Section 2.3.2, the velocity of encounter value is used to exclude the non-wave components of the image spectrum from contributing to the wave spectrum. This is done by classifying the 3-D image spectrum components to wave and non-wave components based on their agreement with the dispersion relationship given by

$$\omega(\mathbf{k}, \mathbf{U}) = \sqrt{gk \tanh(kd)} + \mathbf{k} \cdot \mathbf{U} \tag{7.1}$$

where $\mathbf{k}$ is the wave number vector, $\mathbf{U}$ is the velocity of encounter, d the water depth, g the acceleration due to gravity. Figure 7.1 shows an example of image spectrum in the k, ω domain. It can be seen how most of the spectrum energy is concentrated near the dispersion curve (the red dotted line). A velocity of encounter value of $\mathbf{U} = (U_x, U_y) = (0.54, -0.35)$ m/s, which is estimated using the Hybrid Least squares (HLS) method explained later in this chapter, is used here to plot the dispersion curve.

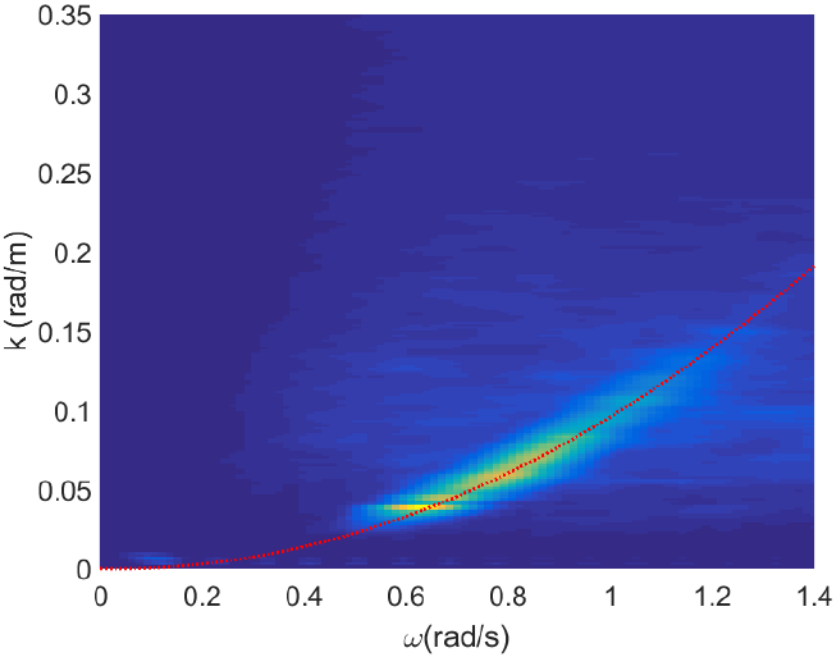

Figure 7.1: An example of the image spectrum in the (k, ω) domain. The dotted red line represents the dispersion relationship given by Equation 7.1.

It can be seen from Equation 7.1 that the velocity of encounter, which is not known *a priori*, is required in order to exclude the non-wave components from the image spectrum. Furthermore, a high velocity of encounter might significantly increase aliasing in the frequency domain which results from under-sampling in the time domain [45]. This effect takes place due to the increase in observed wave frequency according to Equation 7.1. Therefore, velocity of encounter information might also be used to mitigate the effect of the aliasing phenomenon [68–70]. Several methods have been proposed to estimate **U** [10, 45, 46, 55, 56]. These follow one of two approaches: the Least Squares (LS) [10] method and the Normalized Scalar Product (NSP) [45].

7.1.1 The Least Squares (LS) method

The basic LS [10] estimates the optimum **U** that minimizes the error quantity

$$Q^2 = \sum_{i=1}^{N_{c1}} \left(\frac{\omega_i - \omega(\mathbf{k_i}, \mathbf{U})}{\sigma_\omega} \right)^2 \tag{7.2}$$

where $(\mathbf{k_i}, \omega_i)$ are the wavenumber-frequency components of the ith regression coordinate. The image spectrum components that are chosen to be included in the regression process are referred to as the regression coordinates. N_{c1} is the number of regression coordinates, which is the number of image spectrum components that exceed an initial threshold value of $T_{c1} = 0.2$. This is a common empirical value that is chosen based on the assumption that this will separate the fundamental wave components in the image spectrum from higher harmonics and noise [29, 44, 55, 56]. σ_ω is the expected standard deviation of error difference of the theoretical angular frequency given by Equation 7.1 and the angular frequency component of regression coordinates ω_i.

Studies have shown that the LS method produces only a rough estimate of the true **U** and several enhancements had been made to improve its accuracy and reliability [46, 55, 56, 71]. Senet *et al.* [46] proposed several enhancements to this method. The improved LS is referred to as the Iterative Least Squares (ILS) method. The ILS utilizes a larger number of regression coordinates by using a lower threshold value. A common value of this threshold is $T_{c2} = 0.02$ [46]. It is expected with such a low threshold value that not all the regression coordinates follow the fundamental dispersion relationship given in Equation 7.1. This is due to aliasing and the nonlinear imaging process [29]. Instead, the regression process uses the general dispersion relationship with higher order harmonics, which is given by

$$\omega_p(\mathbf{k}, \mathbf{U}) = \pm(p+1)\sqrt{\frac{gk\tanh(kd)}{p+1}} + \mathbf{k}\cdot\mathbf{U}, \qquad p = 0, 1, 2, \ldots, \tag{7.3}$$

where p is the harmonic order. Clearly, substituting $p = 0$ in Equation 7.3 leads to the familiar fundamental dispersion relationship as in Equation 7.1.

Furthermore, the ILS estimates $\mathbf{U}$ iteratively starting from an initial guess that is estimated using the basic LS. The process involves iterative frequency mode classification for regression coordinates as fundamental or first harmonic frequencies and solving for Equation 7.2. Huang *et al.* [56] proposed a further improvement to the ILS by using an adaptive initial guess. It was also proposed in [56] to use the frequency mode classification information to exclude the non-wave components from the wave spectrum instead of using a band-pass filter. This improves the overall performance of the CFT method in terms of accuracy and computational time.

The Polar Current Shell (PCS) , which utilizes a sinusoidal curve-fitting algorithm in polar coordinates and uses LS fitting in the range and azimuth dimensions separately, is another method that was recently proposed for estimating the velocity of encounter [71, 72]. In [73], a comparison of the ILS, NSP and PCS was presented using vertically polarized field data from a stationary X-band marine radar. The study concluded that the three methods perform equally in terms of the estimation accuracy of the velocity of encounter. However, since the radar platform used in the study was stationary, only low values of the velocity of encounter (or simply the surface current velocity) are included in the comparison.

7.1.2 The Normalized Scalar Product (NSP)

The NSP method was first proposed by Serafino *et al.* [45]. In this method, the optimum $\mathbf{U}$ is estimated by maximizing the normalized scalar product

$$V(\mathbf{U}) = \frac{\langle |F_I(\mathbf{k},\omega)|, G(\mathbf{k},\omega,\mathbf{U})\rangle}{\sqrt{P_F P_G}}$$

where $F_I(\mathbf{k},\omega)$ is the image spectrum, P_F and P_G the power of F_I and G, respectively, and $\langle\cdot\rangle$ indicates the scalar product. The characteristic function $G(\cdot,\cdot)$ is given by

$$G(\mathbf{k},\omega,\mathbf{U}) = \begin{cases} 1, & \text{if } |\omega_i - \omega(\mathbf{k_i},\mathbf{U})| \le \Delta\omega. \\ 0, & \text{otherwise.} \end{cases}$$

where $\Delta\omega$ is the angular frequency resolution. This method outperforms the LS based methods in terms of accuracy and reliability at higher ranges of $\mathbf{U}$ ($|\mathbf{U}| >8$ m/s). However, this method is computationally expensive and may thus be restricted to off-line analysis.

In this chapter, a hybrid method is proposed for estimating the velocity of encounter. This method includes both ILS and NSP, and is designed to support high reliability and short computational time, especially at higher ranges of $|\mathbf{U}|$.

7.2 A Hybrid Least Squares Method

Despite its low reliability at higher $|\mathbf{U}|$ as compared to the NPS, the ILS is commonly used due to its short computational time. This makes it more suitable for real time analysis and for stationary platforms and slow moving vessels (such that $|\mathbf{U}| < 6$

m/s). However, at higher speeds, this method may be less robust due to the higher error in the initial guess, which is estimated using the LS method. In order to examine the dependency of the ILS method reliability on the initial guess estimation error, X-band radar images were simulated using different input values of **U** as described in Section 7.3. Subsequently, the ILS method was used to estimate **U** from the simulated X-band radar images. However, the initial guess value of the ILS was not estimated using the LS method. Instead, it was provided to the ILS method. Different initial guess values with a range of absolute error between the initial guess and the true value of 0 to 5 m/s were used. The robustness of the ILS method was measured by the ILS method's failure probability. The ILS method is considered to fail in estimating **U** when the iterative process does not converge to the true value of **U**. The failure probability is measured by the percentage of time the method fails in estimating **U**. Our results, as shown in Figure 7.2, indicate that the initial guess has to be roughly within 2 m/s of the true value in order for the ILS to successfully estimate **U**.

In order to enhance the reliability of the ILS method, a new technique referred to as the Hybrid Least Squares (HLS) method is proposed. The HLS combines the two methods in Section 7.1. The initial guess is estimated using the NSP with a resolution of 1 m/s. Such a low resolution requires a very short computational time (50 ms). At the same time, it guarantees an initial guess within 1 m/s from the true value. Subsequently, the ILS is performed using this initial guess. Another advantage of using this method is that it retains the regression coordinate mode classification for later processing as suggested in [56].

7.3 Numerical Tests

In order to examine the performance of the HLS compared to the NSP and ILS, the three methods are used to estimate $|\mathbf{U}|$ from sets of simulated radar images. The

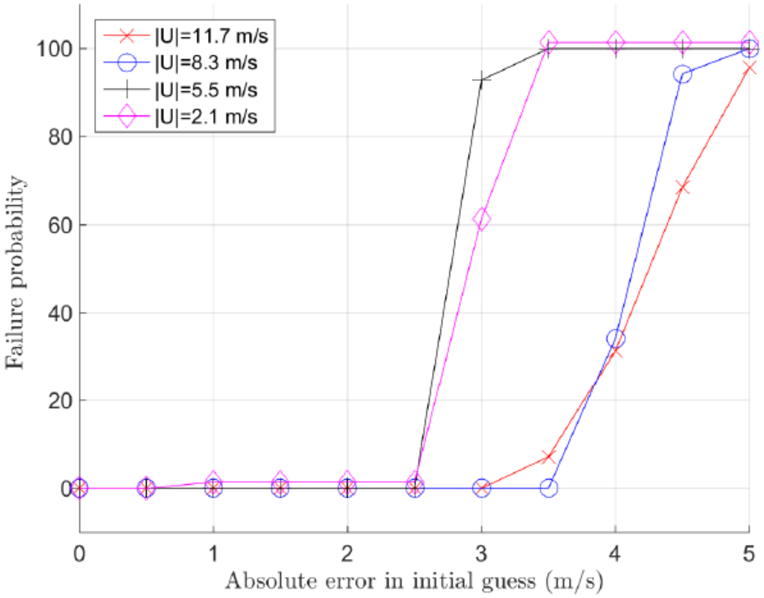

Figure 7.2: Failure probability of ILS dependency on the initial guess value.

simulation was conducted at 4 different values of **U** (2.1, 5.5, 8.3 and 11.7 m/s) with a direction of 180° from the main wave direction. The Pierson-Moskowitz-based power distribution model presented in [66] and a squared cosine distribution (accounting for angular spreading) [11], with random phases that are generated using a uniform distribution, were used to simulate ocean surface elevation. The values of **U** were chosen to cover low to high speeds, while the particular direction was chosen because we have noticed that the reliability of the ILS is most sensitive to the case in which the velocity of encounter direction is opposite to that of the waves. For each of the test values of $|\mathbf{U}|$, 70 sets of radar images were simulated using the parameters listed in Table 7.1. After applying the three methods (NSP, ILS and HLS) to the simulated sets, several comparison metrics were calculated for each method and data set. These metrics include the average absolute error ($\overline{\varepsilon}_{|\mathbf{U}|}$) in the magnitude of the velocity of encounter ($|\mathbf{U}|$) and its standard deviation ($\sigma_{\overline{\varepsilon}_{|\mathbf{U}|}}$), the average absolute error ($\overline{\varepsilon}_{|\mathbf{U}|}$)

Table 7.1: Numerical tests: simulation parameters.

Image set size	128 × 128 × 32 samples
Antenna repetition time	1.44 s
Antenna height	10 m
Sampling frequency	20 MHz
Patch distance from the antenna	1km
Water depth	200 m
Main wave direction	270° from true north

in the direction of the velocity of encounter ($\angle\mathbf{U}$) and its standard deviation ($\sigma_{\overline{\varepsilon}_{\angle\mathbf{U}}}$), and the average computational time ($\overline{\tau}$) and its standard deviation ($\sigma_{\overline{\tau}}$).

7.4 Results and Analysis

Table 7.2 lists the comparison metrics for the three methods with $|\mathbf{U}| = 2.1$ m/s. At this relatively low speed, the results show that the three methods produce accurate estimates for $\mathbf{U}$ with $\overline{\varepsilon}_{|\mathbf{U}|}$ less than 7 cm/s and high reliability with $\sigma_{\overline{\varepsilon}_{|\mathbf{U}|}}$ less than 10 cm/s as well. This indicates that most of the results from the test image sets are located within 10 cm/s of the average estimate. This can be also seen from Figure 7.3 which shows the error vector ($\varepsilon_{\mathbf{U}}$) at $|\mathbf{U}| = 2.1$ m/s. Table 7.2 also shows that the NSP requires a relatively large computational time $\overline{\tau}(s)$ (71 s) compared to the other two methods which require less than 0.5 s. Therefore, at such low speeds the ILS and the HLS are preferable over the NPS.

Similar conclusions can be drawn from the results of $|\mathbf{U}| = 5.5$ m/s as shown in Table 7.3 and Figure 7.4. Moving to a higher range ($|\mathbf{U}| = 8.3$ m/s), it can be seen from

Table 7.4 that both the accuracy and reliability of the ILS are reduced as compared to those of the other two methods with $\overline{\varepsilon}_{|\mathbf{U}|} = 0.21$ m/s and $\sigma_{\overline{\varepsilon}_{|\mathbf{U}|}} = 0.25$ m/s. This is due to incorrect results for some image sets when the iterative method started with poor initial guesses. These incorrect estimates do not appear in Figure 7.5 as they are located further than 2 m/s from the true value and are truncated from the plot as shown. The probability of the ILS to break down dramatically increases at speeds of 8 m/s and higher. The main reason for this failure is a poor initial guess. This should not be surprising as for higher speeds the regression coordinates are expected to be scattered far from the fundamental dispersion shell. Meanwhile, the HLS is still able to maintain accurate and reliable estimates while maintaining a very short computational time. At $|\mathbf{U}| = 11.7$ m/s, the highest speed considered in this paper, Table 7.2 shows that the ILS has completely failed to estimate $\mathbf{U}$ as seen from the fact that $\overline{\varepsilon}_{|\mathbf{U}|}$ and $\sigma_{\overline{\varepsilon}_{|\mathbf{U}|}}$ equal 4.4 and 4.7, respectively. This shows that more of the ILS estimates did not converge acceptably close to the true value. This can be seen in Figure 7.6 where fewer values of the ILS are shown. On the other hand the other two methods maintain satisfactory accuracy and reliability.

Among the three, the HLS shows very short computational times and high accuracy and reliability for all velocities of encounter ranges. In our study, this indicates that the proposed method (HLS) significantly outperforms the two other methods (ILS and NSP).

Table 7.2: Velocity of encounter magnitude $|\mathbf{U}| = 2.1$ m/s.

	$\overline{\varepsilon}_{|\mathbf{U}|}$ (m/s)	$\sigma_{\overline{\varepsilon}_{|\mathbf{U}|}}$	$\overline{\varepsilon}_{\angle \mathbf{U}}$ (°)	$\sigma_{\overline{\varepsilon}_{\angle \mathbf{U}}}$	$\overline{\tau}(s)$	$\sigma_{\overline{\tau}}$
NSP	0.07	0.09	3.9	4.7	71.7	11.0
ILS	0.07	0.09	3.9	5.0	0.1	0.02
HLS	0.06	0.08	4.1	4.5	0.28	0.05

Table 7.3: Velocity of encounter magnitude $|\mathbf{U}| = 5.5$ m/s.

	$\overline{\varepsilon}_{|\mathbf{U}|}$ (m/s)	$\sigma_{\overline{\varepsilon}_{|\mathbf{U}|}}$	$\overline{\varepsilon}_{\angle \mathbf{U}}$ (°)	$\sigma_{\overline{\varepsilon}_{\angle \mathbf{U}}}$	$\overline{\tau}(s)$	$\sigma_{\overline{\tau}}$
NSP	0.06	0.06	0.5	0.7	127.6	27
ILS	0.08	0.05	0.5	0.6	0.23	0.05
HLS	0.09	0.05	0.5	0.6	0.5	0.1

Table 7.4: Velocity of encounter magnitude $|\mathbf{U}| = 8.3$ m/s.

	$\overline{\varepsilon}_{|\mathbf{U}|}$ (m/s)	$\sigma_{\overline{\varepsilon}_{|\mathbf{U}|}}$	$\overline{\varepsilon}_{\angle \mathbf{U}}$ (°)	$\sigma_{\overline{\varepsilon}_{\angle \mathbf{U}}}$	$\overline{\tau}(s)$	$\sigma_{\overline{\tau}}$
NSP	0.15	0.11	0.4	0.6	122.3	28
ILS	0.21	0.25	0.2	0.3	0.2	0.05
HLS	0.17	0.1	0.2	0.3	0.5	0.1

Table 7.5: Velocity of encounter magnitude $|\mathbf{U}| = 11.7$ m/s.

	$\overline{\varepsilon}_{|\mathbf{U}|}$ (m/s)	$\sigma_{\overline{\varepsilon}_{|\mathbf{U}|}}$	$\overline{\varepsilon}_{\angle \mathbf{U}}$ (°)	$\sigma_{\overline{\varepsilon}_{\angle \mathbf{U}}}$	$\overline{\tau}(s)$	$\sigma_{\overline{\tau}}$
NSP	0.3	0.18	0.3	0.4	124	28
ILS	4.4	4.7	27	58	0.23	0.05
HLS	0.16	0.15	0.2	0.25	0.5	0.11

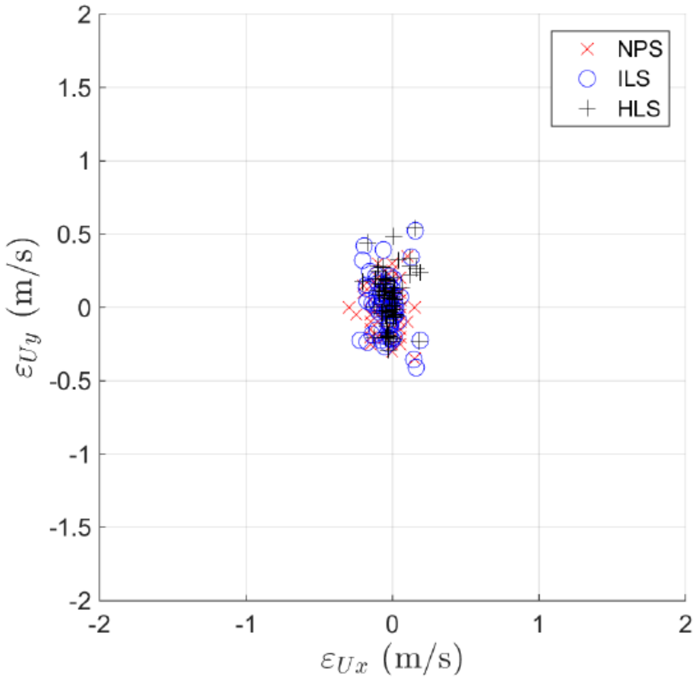

Figure 7.3: Error vector ($\varepsilon_{\mathbf{U}}$) at$|\mathbf{U}| = 2.1$ m/s.

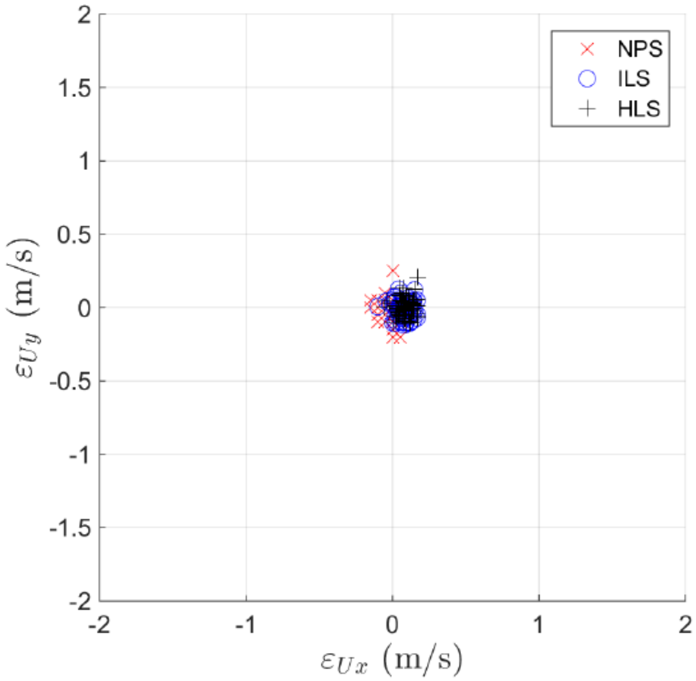

Figure 7.4: Error vector ($\varepsilon_{\mathbf{U}}$) at$|\mathbf{U}| = 5.5$ m/s.

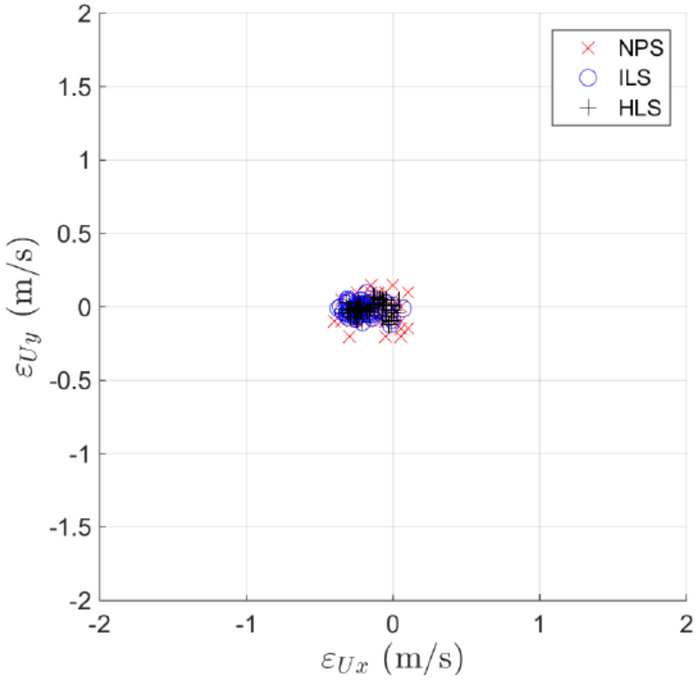

Figure 7.5: Error vector ($\varepsilon_{\mathbf{U}}$) at$|\mathbf{U}| = 8.3$ m/s.

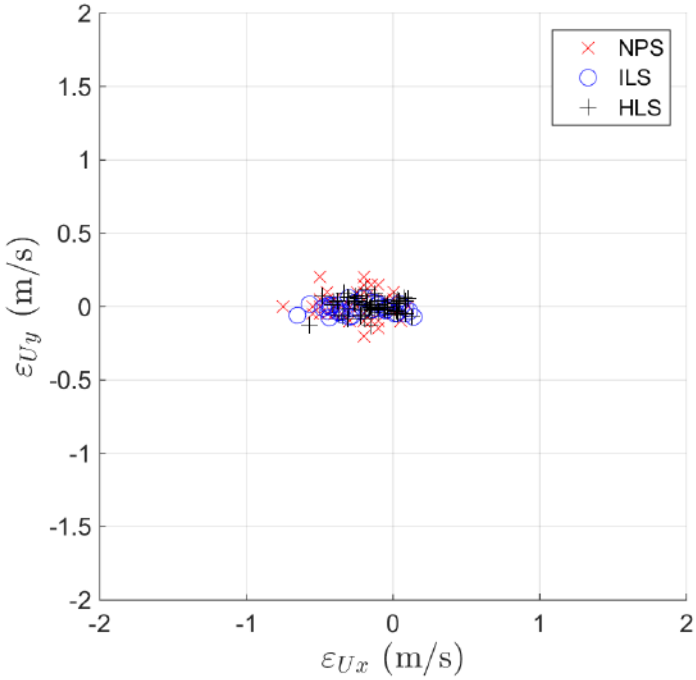

Figure 7.6: Error vector ($\varepsilon_{\mathbf{U}}$) at$|\mathbf{U}| = 11.7$ m/s.

7.5 Conclusions

The value of the velocity of encounter is important in wave spectrum estimation using the 3D Fourier transformation on nautical radar images. It is used to exclude non-wave components from the image spectrum to produce the wave spectrum. Two main approaches are currently used to estimate velocity of encounter: the Iterative Least Squares (ILS) and Normalized Scalar Product (NSP). The ILS provides short computational time and good accuracy at lower values of the velocity of encounter. However, the reliability of this method dramatically drops at speeds of 8 m/s and higher. The main reason for such poor performance at high speeds has been identified in this chapter to be due to a poor initial guess. On the other hand, the NSP provides high reliability at all speed ranges but at the price of long computational times. In this chapter, a new algorithm that combines the ILS and NSP to support short computational time and high reliability is proposed. The method is referred to as Hybrid Least Squares (HLS). The new method estimates the initial guess using the NSP and then uses the ILS method to refine the estimate. Our results show that HLS achieves its purpose by supporting a short computational time while maintaining high reliability at all speed ranges.

Chapter 8

Summary and future work

8.1 Summary of the thesis

The ocean is one of the earth's most important natural resources. Fisheries provide humans with one of the most nutritious food resources. The ocean also plays a key role in transportation around the globe with most goods being shipped via sea routes. Furthermore, the ocean has a significant impact on our climate with regulating the amount of CO_2 in the atmosphere. Also, a huge amount of crude oil and natural gas has been discovered trapped under the ocean seabed. This has motivated great attention among drilling companies and engineers to exploit these energy resources. It is quite clear how important the ocean is in our lives. This has motivated researchers since ancient times to study the ocean in order to better use its resources.

Ocean wave spectra are widely accepted as a descriptive model of the ocean system. Wave spectra represent the ocean surface system in terms of the energy content of contributing plane ocean waves. Several technologies have been developed to estimate ocean wave spectra, such as wave buoys and remote sensing using HF and X-band radars. The purpose of this thesis is to develop accurate and reliable methods for wave spectra and sea state parameters estimation using X-band marine radar. Three wave spectral estimation algorithms in addition to a surface current estimation algorithm have been proposed to address different sources of error in the current Cartesian Fourier Transform (CFT) method of ocean wave spectra and sea state parameter estimation.

The first algorithm, which was proposed in Chapter 3 of this thesis, addresses the dependency of the X-band marine radar-estimated ocean wave spectra on the azimuth location of the analysis window. One of the advantages of using X-band marine radars to estimate ocean wave spectra is that they can provide field data from a wide area, usually within a radius of 5 km and azimuth of 360° when deployed at sea. In practice, not all the radar field data are analyzed to estimate the ocean wave spectra. Typically, rectangular analysis windows with a size of 256×128 samples [18, 29], covering an area of 1920×960 m^2, are chosen from the radar data to be used for analysis. It has been reported in the literature and verified in this thesis that the azimuth location of the analysis window influences the estimated ocean wave spectra. This is due to the effect of the radar imaging process represented by shadowing and tilt modulation.

Traditionally, several analysis windows that are uniformly distributed in the azimuth direction have been used to eliminate the dependency of the estimated wave spectra on the azimuth direction. In this thesis, it was verified using simulated X-band radar data that the effect of shadowing and tilt modulation is minimum in the up-wave azimuth direction. Therefore, better ocean wave estimates are expected when choosing the analysis window in the up-wave directions. However, two challenges are present here: the up-wave direction is not known *a priori* and the ocean system might have not only wind waves but swell as well, and hence multiple up-wave directions. Therefore, the Adaptive Recursive Positioning Method (ARPM) was proposed to address this problem. The ARPM uses three analysis windows to estimate initial spectra. The up-wave direction and the number of analysis windows are determined from the initial spectra. Subsequently, new wave spectra are acquired using new analysis windows that are located in the up-wave directions. The process is repeated recursively to achieve more accurate results.

The ARPM results from field data showed an improvement of 9.8% on the agreement between the CFT-estimated and the ground truth frequency wave spectrum. Also, 20%, 20%, and 22% improvements in the peak wave period, mean wave period and peak wave direction estimates, respectively, were achieved by implementing the ARPM method. These improvements come at the expense of extra computational time. Implementing the ARPM requires computational time that is double or triple the time needed by the conventional CFT method. Fortunately, the ARPM can be implemented in near real-time because its computational time still does not exceed the radar data generating time. The ARPM's applicability is limited to cases where the radar data is available for a full 360° azimuth range. A possible enhancement on the method is to expand its applicability to the cases where the field of view is partially blocked. This can be addressed by using the available field of view to determine an initial estimate. If the up-wave direction lies in the available part of the field of view, the ARPM can proceed normally. Otherwise, the algorithm would terminate and the initial estimate would be used.

In Chapter 4 the sampling process of the ocean surface by X-band radar and its effect on the ocean wave spectra estimation were revisited. Traditionally, the radar sampling process is considered to be a standard sampling, in which the ocean surface elevation is sampled at the centre of the polar sample areas. It was demonstrated in Chapter 4 that this assumption is not accurate. A B-scan sample is generated by accumulating the returned scatter from the whole sample area, which is determined by the radar beam width and range resolution. This motivates the assumption that the radar sampling of the ocean surface involves an averaging process, which is equivalent to using a low-pass filter in the frequency domain. The radar sampling process was simulated in order to understand its effect on the estimated ocean wave spectra. The results support the assumption of using an averaging filter in the sampling process. An analytical model was presented to describe the frequency response of the sampling low pass filter. Furthermore, an approximation of the inverse low pass filter is presented, which is referred to as the Inverse Sampling Averaging Filter (ISAF). It was also proposed to implement the ISAF in the CFT method in order to mitigate the effect of the radar sampling process. For validation, the CFT method with and without the ISAF were used to estimate ocean wave spectra and wave period and direction. The estimates from the standard CFT method and the CFT with ISAF are compared to ground truth estimates, which are acquired using a TRIAXYS wave rider buoy data. The results show that using the ISAF provides an improvement of 11% in the agreement between the CFT-estimated and the ground truth frequency wave spectrum. Furthermore, the ISAF improves the estimates of peak wave period, mean wave period, and peak wave direction by 12%, 20%, and 26%, respectively.

Another source of error in wave spectra estimation with the CFT that was addressed in this thesis is the effect of the scan conversion process. The scan conversion process is used to convert the radar output samples, which are digitized on a polar grid and referred to as B-scan images, to Cartesian images. This step is necessary to allow the application of the CFT on the Cartesian images. This scan conversion process adds some distortion to the estimated wave spectra. From a signal processing point of view, scan conversion is a process of re-sampling in which the original continuous image of the ocean surface is retrieved and subsequently sampled on a new Cartesian grid. In the wave number frequency domain, retrieving the original continuous image is equivalent to applying a low-pass filter. To achieve a distortionless retrieval, an ideal low pass filter is required. Of course, an ideal low-pass filter can not be achieved in practice and approximations necessarily introduce distortion to the estimated wave spectra.

In Chapter 5 of this thesis, discarding the scan-conversion process is proposed. In order to do so, a method of applying the 3D Fourier transformation in polar coordinates instead of Cartesian coordinates is required. A transform that is referred to as the Polar Fourier Transformation (PFT) [17] is adopted for that purpose. The PFT is modified to allow its applicability on radar data. For performance validation of the PFT compared to the CFT, both transforms are applied on field data described in Section 2.4. The ocean wave spectra estimates from both transforms were compared to ground truth estimates that were acquired using TRIAXYS wave rider buoy data. In the comparison analysis, the agreement between the radar-estimated ocean frequency wave spectrum (using either the CFT or the PFT) and the ground truth spectrum is represented using the correlation coefficient between the two spectra. Other comparison metrics that are used include the mean absolute error and error standard deviation in the estimation of the wave period and direction. The results showed that the estimates of the frequency wave spectrum that were acquired using the PFT represent a 12% improvement in the agreement with the ground truth frequency wave spectrum compared to the CFT-estimates. The results presented in this thesis also showed that using the PFT produces 44%, 54% and 49% improvements in the peak wave period, mean wave period, and peak wave direction estimates, respectively. The main drawback of the PFT method is the relatively long computational time. In our analysis, in which the implementations of the PFT and the CFT run on the same processor and with similar data structure efficiency, the CFT required only 20% of the time needed by the PFT to analyze the same data. The time that the PFT needed to analyze a 32 radar image set was 4.3 min compared to 2.7 s using the standard CFT method. The CFT fast data analysis capability is due to the

Fast Fourier Transform (FFT) algorithm. On the other hand, there exists no similar fast algorithm to perform the PFT. An enhancement on the PFT method that could greatly increase its applicability, which can be addressed in the future, would be to develop a fast algorithm to compute the transformation.

The performance of implementing the CFT, PFT, ARPM, PFT, and their combinations in estimating ocean wave spectra and ocean wave period and direction is validated in Chapter 6. It was found that the most accurate estimates of the peak wave direction were achieved when the PFT was implemented with the ARPM and the ISAF with an improvement of 72% when compared to the CFT method. On the other hand, the most accurate estimates of the mean wave period and peak wave direction with improvements of 65% and 55%, respectively, over the CFT method were achieved using the ARPM with ISAF method.

Finally, the problem of estimating the velocity of encounter **U** was addressed in Chapter 7. The velocity of encounter represents the vector summation of the ocean surface current velocity and the ship velocity. The velocity of encounter information has a key role in reducing the noise and removing the non-wave components from the 3D image spectrum in order to produce the 3D ocean wave spectrum. Higher magnitudes of **U** increases the possibility of aliasing in the image spectrum. Estimating **U** is crucial for the CFT method of wave spectra estimation. Two main methods are currently used to estimate **U**: the Iterative Least Squares (ILS) method and the Normalized Scalar Product (NSP). Both methods provide accurate estimates at low speeds of **U**. The ILS method provides lower computational time compared to the NSP. However, the accuracy and reliability of the ILS drop dramatically at higher values of **U** while the NSP maintains performance at higher values of **U**. In this thesis, it was found that main reason that the ILS drops performance at higher values of **U** is the poor initial guess of the recursive process. Thus, a hybrid method for estimating

U was proposed. This method is referred to as the Hybrid iterative Least Squares (HLS) The initial guess is estimated using the NSP with wide intervals. This allows a good rough initial estimate of **U** with a short computational time. Subsequently, the initial guess is provided to the ILS to start the recursive process. Simulated X-band radar images were used to validate the performance of the proposed method. The results show that the HLS maintains its accuracy and reliability at higher values of **U** and has low computational time.

8.2 Future work

While the thesis presented a significant improvement on the estimation of ocean wave spectra and sea state parameters, extension opportunities on the presented algorithms remain.

In Chapter 3, the shadowing effect was found to be minimum in the up-wave and down-wave directions. These behaviors are not clear and need further investigation.

Another interesting conclusion can be found in Chapter 6 where implementing the ARPM provided a slight deterioration in the performance of the PFT with ISAF in estimating T_{01}, T_z, and θ_p. Further investigation is required in order to explain this behavior.

Despite the improvement introduced by the PFT method, proposed in Chapter 5 in estimating the ocean wave spectra and sea state parameters, the method may still not be applied for real-time applications using the current form of the PFT due to its long computational time. In our analysis, one ring sector analysis window with a size of $320 \times 128 \times 32$ required 4.3 minutes to be analyzed using the PFT method. In order for the PFT to be implemented in real time applications, the processing time should be brought down to less than 44.3 s, which is the time required to generate a 32-image radar set. This condition is considered under the assumption that only one analysis window is used to estimate wave spectra and sea state parameters. Since, in practice, multiple analysis windows are used, the processing time should not exceed $44.3/n$ s, where n is the number of analysis windows. A future enhancement on the current PFT method is to design a more efficient PFT such that the method can be implemented in real time applications.

Another future work direction of this thesis concerns the applicability expansion of the proposed methods to other sea state parameters. Even though the performance enhancement using the proposed methods of ARPM, ISAF and PFT was validated for estimating ocean wave spectra and wave period and direction, the applicability of the proposed methods is not limited to those parameters. After a proper validation, the proposed methods may also be applied to estimate other sea state parameters, such as significant wave heights, or related information, such as wind speed and direction.

Bibliography

[1] M. Skolnik, *Radar Handbook*, 3rd ed. Mc Graw Hill, 2008.

[2] The USGS Water Science School, "U.S. geological survey," https://water.usgs.gov/edu/earthwherewater.html, 2016.

[3] Food and Agricultural Organization of the United Nations, "The state of world fisheries and aquaculture 2014," http://www.fao.org/3/a-i3720e.pdf, 2017.

[4] Government of Canada. (2016) Canada's fisheries fast facts of 2015. [Online]. Available: http://www.dfo-mpo.gc.ca/stats/facts-Info-15-eng.htm

[5] Canada's Oil Natural Gas Producers. (2016) Atlantic canada's offshore oil and gas industry. [Online]. Available: http://atlanticcanadaoffshore.ca/projects-exploration-newfoundland-labrador/

[6] M. Tucker, *Waves in Ocean Engineering: Measurement, Analysis, Interpretation.* Ellis Horwood, 1991.

[7] B. Kinsman, *Wind Waves, their Generation and Propagation on the Ocean Surface.* New Jersey, United States: Englewood Cliffs, N.J., Prentice-Hall, 1965.

[8] O. M. Phillips, *The Dynamics of the Upper Ocean.* New York , United States: Cambridge University Press, 1977.

[9] COST Action 714, *Measuring and Analysing the Directional Spectra of Ocean Waves.* Office for Official Publications of the European Communities, 2005.

[10] I. Young, W. Rosenthal, and F. Ziemer, “A three-dimensional analysis of marine radar images for the determination of ocean wave directionality and surface currents,” *J. Geophys. Res.*, pp. 1049–1059, 1985.

[11] J. C. Nieto-Borge, “Inversion of marine radar images for surface wave analysis,” *Journal of Atmospheric and Oceanic Technology*, vol. 31, pp. 1291–1059, Aug. 2004.

[12] B. Lund, C. Collins, H. Graber, E. Terrill, and T. Herbers, “Marine radar ocean wave retrieval’s dependency on range and azimuth,” *Ocean Dynamics*, vol. 64, no. 7, pp. 999–1018, 2014.

[13] K. Nickerson and S. Haykin, “Scan conversion of radar images,” *IEEE Transactions on Aerospace and Electronic Systems*, vol. 25 (2), pp. 166–175, Mar. 1989.

[14] A. Al-Habashneh, C. Moloney, and E. Gill, “Towards ocean wave spectrum estimation from marine radar data by the Polar Fourier Transform,” in *Proceedings of MTS/IEEE Oceans Conference, Bergen, Norway*, June 2013.

[15] ——, “Ocean wave spectrum estimation from marine radar data using the polar fourier transform,” in *Proceedings of MTS/IEEE Oceans Conference, Taipei, Taiwan*, April 2014.

[16] A.-A. Al-Habashneh, C. Moloney, E. W. Gill, and W. Huang, “An adaptive method of wave spectrum estimation using X-band nautical radar,” *Remote Sensing*, vol. 7, no. 12, p. 15851, 2015. [Online]. Available: http://www.mdpi.com/2072-4292/7/12/15851

[17] Q. Wang, O. Ronneberger, and H. Burkhardt, "Rotational invariance based on Fourier analysis in polar and spherical coordinates," *IEEE Transactions on Pattern Analysis and Machine Intelligence*, vol. 31 (9), pp. 1715–1722, Sep. 2009.

[18] A. Al-Habashneh, C. Moloney, E. Gill, and W. Huang, "A hybrid method for surface current estimation using X-band nautical radar," in *Radar Symposium (IRS), 2015 16th International, Dresden,Germany*, June 2015, pp. 840–845.

[19] C. Therrien and M. Tummala, *Probability and Random Processes for Electrical and Computer Engineers, Second Edition.* CRC Press, 2011.

[20] W. C. O'Reilly, T. H. C. Herbers, R. J. Seymour, and R. T. Guza, "A comparison of directional buoy and fixed platform measurements of Pacific swell," vol. 13, pp. 231–238, 1996.

[21] J. C. Nieto-Borge, K. Hessner, P. Jarabo-Amores, and D. de la Mata-Moya, "Signal-to-noise ratio analysis to estimate ocean wave heights from X-band marine radar image time series," *IET Radar, Sonar Navigation,*, vol. 2, no. 1, pp. 35–41, February 2008.

[22] B. Lund, C. O. Collins, H. Tamura, and H. C. Graber, "Multi-directional wave spectra from marine X-band radar," *Ocean Dynamics*, vol. 66, no. 8, pp. 973–988, 2016. [Online]. Available: http://dx.doi.org/10.1007/s10236-016-0961-z

[23] W. J. Plant and W. C. Keller, "Evidence of Bragg scattering in microwave doppler spectra of sea return," *Journal of Geophysical Research: Oceans*, vol. 95, no. C9, pp. 16 299–16 310, 1990.

[24] M. Long, *Radar Reflectivity of Land and Sea.* Artech House, 2001.

[25] J. C. Nieto-Borge and C. G. Soares, "Analysis of directional wave fields using X-band navigation radar," *Coastal Engineering*, vol. 40, pp. 375–391, 2000.

[26] W. Alpers, D. Ross, and C. Rufenach, “On the detectability of ocean surface waves by real and synthetic aperture radar,” *J. Geophys. Res.*, vol. 86 (C7), pp. 6481–6498, 1981.

[27] W. Plant and G. Farquharson, “Wave shadowing and modulation of microwave backscatter from the ocean,” *Journal of Geophysical Research: Oceans*, vol. 117, no. C8, 2012.

[28] P. H. Y. Lee, J. D. Barter, K. L. Beach, C. L. Hindman, B. M. Lake, H. Rungaldier, J. C. Shelton, A. B. Williams, R. Yee, and H. C. Yuen, “X band microwave backscattering from ocean waves,” *Journal of Geophysical Research: Oceans*, vol. 100, no. C2, pp. 2591–2611, 1995.

[29] J. C. Nieto-Borge, G. Rodriguez, K. Hessner, and P. Gonzalez, “Inversion of marine radar images for surface wave analysis,” *Journal of Atmospheric and Oceanic Technology*, vol. 21 (8), pp. 1291–1300, 2004.

[30] A. Chaudhry and R. Moore, “Tower-based backscatter measurements of the sea,” *IEEE Journal of Oceanic Engineering*, vol. 9, no. 5, pp. 309–316, December 1984.

[31] J. C. Daley, J. T. Ransone, J. A. Burkett, and J. R. Duncan, “Sea-clutter measurements on four frequencies,” Naval Research Lab, Washington DC, US, Tech. Rep., November 1968.

[32] P. Izquierdo and C. G. Soares, “Analysis of sea waves and wind from X-band radar,” *Ocean Engineering*, vol. 32, pp. 1404–1419, 2005.

[33] Y. Liu, W. Huang, E. Gill, D. Peters, and R. Vicen-Bueno, “Comparison of algorithms for wind parameters extraction from shipborne X-band marine radar images,” *IEEE Journal of Selected Topics in Applied Earth Observations and Remote Sensing,*, vol. 8, no. 2, pp. 896–906, Feb 2015.

[34] H. Dankert and J. Horstmann, "A marine-radar wind sensor," in *IEEE International Conference on Geoscience and Remote Sensing Symposium, Denver, CO, USA*, July 2006, pp. 1296–1299.

[35] B. Lund, H. Graber, and R. Romeiser, "Wind retrieval from shipborne nautical X-band radar data," *IEEE Transactions on Geoscience and Remote Sensing,*, vol. 50, no. 10, pp. 3800–3811, Oct 2012.

[36] H. Hatten, F. Ziemer, J. Seemann, and J. C. Nieto-Borge, "Correlation between the spectral background noise of a nautical radar and the wind vector," in *Proceedings of 17th OMAE Conference*, 1998.

[37] W. Huang and Y. Wang, "A spectra-analysis-based algorithm for wind speed estimation from X-band nautical radar images," *IEEE Geoscience and Remote Sensing Letters*, vol. 13, no. 5, pp. 701–705, May 2016.

[38] Y. Wang and W. Huang, "An algorithm for wind direction retrieval from X-band marine radar images," *IEEE Geoscience and Remote Sensing Letters*, vol. 13, no. 2, pp. 252–256, Feb 2016.

[39] P. S. Bell, "Shallow water bathymetry derived from an analysis of X-band marine radar images of waves," *Coastal Engineering*, vol. 37, no. 34, pp. 513 – 527, 1999.

[40] C. Senet, J. Seemann, S. Flampouris, and F. Ziemer, "Determination of bathymetric and current maps by the method disc based on the analysis of nautical X-band radar image sequences of the sea surface (November 2007)," *IEEE Transactions on Geoscience and Remote Sensing,*, vol. 46, no. 8, pp. 2267–2279, Aug 2008.

[41] K. Hessner, K. Reichert, J. C. Nieto-Borge, C. L. Stevens, and M. J. Smith, "High-resolution X-band radar measurements of cur-

rents, bathymetry and sea state in highly inhomogeneous coastal areas," *Ocean Dynamics*, vol. 64, no. 7, pp. 989–998, 2014. [Online]. Available: http://dx.doi.org/10.1007/s10236-014-0724-7

[42] F. Ziemer and J. Dittmer, "A system to monitor ocean wave fields," in *OCEANS '94. 'Oceans Engineering for Today's Technology and Tomorrow's Preservation.' Proceedings, Brest, France*, vol. 2, Sep 1994, pp. II/28–II/31 vol.2.

[43] J. Nieto-Borge, "First experience with the use of marine radar to survey ocean wave fields," in *Proceed. of the WMO/IOC Workshop on Operational Ocean Monitoring using Surface Based Radars*, March 1995.

[44] J. C. Nieto-Borge, K. Reichert, and J. Dittmer, "Use of nautical radar as a wave monitoring instrument," *Coastal Engineering*, vol. 37, pp. 331–341, 1998.

[45] F. Serafino, C. Lugni, and F. Soldovieri, "A novel strategy for the surface current determination from marine X-band radar data," *IEEE Geoscience and Remote Sensing Letters,*, vol. 7, no. 2, pp. 231–235, April 2010.

[46] C. Senet, J. Seemann, and F. Ziemer, "The near-surface current velocity determined from image sequences of the sea surface," *IEEE Transactions on Geoscience and Remote Sensing,*, vol. 39, no. 3, pp. 492–505, Mar 2001.

[47] K. Reichert, K. Hessner, J. Nieto-Borge, and J. Dittmer, "WAMOS II: A radar based wave and current monitoring system," in *Proceedings of the ninth ISOPE*, vol. 3, Brest, France, 1999, pp. 1–5.

[48] Z. Chen, B. Zhang, Y. He, Z. Qiu, and W. Perrie, "A new modulation transfer function for ocean wave spectra retrieval from X-band marine radar imagery," *Chinese Journal of Oceanology and Limnology*, pp. 1–10, 2015.

[49] L. Wua, L. D. Doongc, and C. Kaoa, "Ocean remotely sensed image analysis using two-dimensional continuous wavelet transforms," *International Journal of Remote Sensing*, pp. 1–20, 2011.

[50] Z. Chen, Y. He, B. Zhang, Z. Qiu, and B. Yin, "A new algorithm to retrieve wave parameters from marine X-band radar image sequences," *IEEE Transactions on Geoscience and Remote Sensing,*, vol. 52, no. 7, pp. 4083–4091, July 2014.

[51] B. Edde, *Radar Principles, Technology, Applications.* Prentice Hall, 1995.

[52] M. Farmer and S. Sohn, "Programmed radar coordinate scan conversion," Patent 5 519 401, 05 21, 1996.

[53] H. M. Deitel, *C++ How To Program, Fifth Edition.* Prentice Hall, 2005.

[54] *The Wave and Surface Current Monitoring System (WaMoS) II operating manual*, 4th ed., OceanWaves GmbH, Luneburg, Germany, 5 2012.

[55] W. Huang and E. Gill, "Surface current measurement under low sea state using dual polarized X-band nautical radar," *IEEE Journal of Selected Topics in Applied Earth Observations and Remote Sensing*, vol. 5, no. 6, pp. 1868–1873, Dec 2012.

[56] W. Huang, E. Gill, and J. An, "Iterative least-squares-based wave measurement using X-band nautical radar," *IET Radar, Sonar Navigation*, vol. 8, no. 8, pp. 853–863, October 2014.

[57] M. K. Ochi, *Ocean Waves : the Stochastic Approach.* Cambridge, U.K. ; New York : Cambridge University Press, 1998, includes bibliographical references and index.

[58] J. C. Nieto-Borge, K. Reichert, and K. Hessner, "Detection of spatio-temporal wave grouping properties by using temporal sequences of X-band radar images of the sea surface," *Ocean Modelling*, vol. 61, pp. 21 – 37, 2013. [Online]. Available: http://www.sciencedirect.com/science/article/pii/S1463500312001497

[59] C. Collins, B. Lund, R. Ramos, W. Drennan, and H. Graber, "Wave measurement intercomparison and platform evaluation during the itop (2010) experiment," *Journal of Atmospheric and Oceanic Technology*, vol. 31 (10), pp. 2309–2329, Oct. 2014.

[60] R. Gangeskar, "An algorithm for estimation of wave height from shadowing in X-band radar sea surface images," *IEEE Transactions on Geoscience and Remote Sensing,*, vol. 52, no. 6, pp. 3373–3381, June 2014.

[61] S. Salcedo-Sanz, J. C. Nieto-Borge, L. Carro-Calvo, L. Cuadra, K. Hessner, and E. Alexandre, "Significant wave height estimation using {SVR} algorithms and shadowing information from simulated and real measured X-band radar images of the sea surface," *Ocean Engineering*, vol. 101, pp. 244 – 253, 2015. [Online]. Available: http://www.sciencedirect.com/science/article/pii/S0029801815001225

[62] E. Alexandre, L. Cuadra, J. Nieto-Borge, G. Candil-Garc M. del Pino, and S. Salcedo-Sanz, "A hybrid genetic algorithm-treme learning machine approach for accurate significant wave height reconstruction," *Ocean Modelling*, vol. 92, pp. 115 – 123, 2015. [Online]. Available: http://www.sciencedirect.com/science/article/pii/S1463500315001092

[63] L. Cornejo-Bueno, J. C. Nieto-Borge, E. Alexandre, K. Hessner, and S. Salcedo-Sanz, "Accurate estimation of significant wave height with support vector regression algorithms and marine radar images," *Coastal Engineering*,

vol. 114, pp. 233 – 243, 2016. [Online]. Available: http://www.sciencedirect.com/science/article/pii/S0378383916300412

[64] X. Liu, W. Huang, and E. W. Gill, “Comparison of wave height measurement algorithms for ship-borne X-band nautical radar,” *Canadian Journal of Remote Sensing*, vol. 42, no. 4, pp. 343–353, 2016. [Online]. Available: http://dx.doi.org/10.1080/07038992.2016.1177450

[65] K. Reichert, “Analysis of the azimuth dependence of the navigation radar imaging of the sea surface,” Master’s thesis, University of Hamburg, Germany, 1994.

[66] D. Nomiyama and T.Hirayama, “Evaluation of marine radar as an ocean-wave-field detector through full numerical simulation,” *Marine Science and Technology*, pp. 88–98, 2003.

[67] A. Grove, *An Introduction to the Laplace Transform and the Z-Transform.* Prentice Hall, 1991.

[68] F. Serafino, C. Lugni, J. C. Nieto-Borge, and F. Soldovieri, “A simple strategy to mitigate the aliasing effect in X-band marine radar data: Numerical results for a 2d case,” *Sensors*, vol. 11, no. 1, p. 1009, 2011. [Online]. Available: http://www.mdpi.com/1424-8220/11/1/1009

[69] J. Seemann and F. Ziemer, “Computer simulation of imaging ocean wave fields with a marine radar,” in *OCEANS ’95. MTS/IEEE. Challenges of Our Changing Global Environment. Conference Proceedings.*, vol. 2, Oct 1995, pp. 1128–1133 vol.2.

[70] J. Seemann, F. Ziemer, and C. M. Senet, “A method for computing calibrated ocean wave spectra from measurements with a nautical X-band radar,”

in *OCEANS '97. MTS/IEEE Conference Proceedings*, vol. 2, Oct 1997, pp. 1148–1154 vol.2.

[71] C. Shen, W. Huang, E. W. Gill, R. Carrasco, and J. Horstmann, "An algorithm for surface current retrieval from X-band marine radar images," *Remote Sensing*, vol. 7, no. 6, p. 7753, 2015. [Online]. Available: http://www.mdpi.com/2072-4292/7/6/7753

[72] C. Shen, W. Huang, and E. W. Gill, "An alternative method for surface current extraction from X-band marine radar images," in *2014 IEEE Geoscience and Remote Sensing Symposium*, July 2014, pp. 4370–4373.

[73] W. Huang, R. Carrasco, C. Shen, E. W. Gill, and J. Horstmann, "Surface current measurements using X-band marine radar with vertical polarization," *IEEE Transactions on Geoscience and Remote Sensing*, vol. 54, no. 5, pp. 2988–2997, May 2016.